LUDWIG
MAXIMILIANS
UNIVERSITÄT
MÜNCHEN

WALTHER - MEISSNER -
INSTITUT FÜR TIEF -
TEMPERATURFORSCHUNG

BAYERISCHE
AKADEMIE DER
WISSENSCHAFTEN

Superconducting Hybrid Rings for Homodyne Detections of Microwave Signals

Diploma Thesis

Elisabeth Hoffmann

Advisor: Prof. Dr. Rudolf Gross

Munich, 15 February 2008

LUDWIG MAXIMILIANS UNIVERSITÄT MÜNCHEN

Abstract

During the last years, the topic of superconducting circuit quantum electrodynamics has attracted increasing interest. After, A. Wallraff et al. [1] observed the coherent exchange of a microwave single photon between a superconducting charge qubit strongly coupled to an on-chip microwave cavity, it became clear that the coupling of a quantum mechanical two-level system to a microwave photon on one chip is possible.
In 2005 M. Mariantoni [2] proposed an experimental setup to deterministically generate single microwave photons in a system of a flux qubit strongly coupled to a resonator. Since single microwave photon detectors are not available yet, a technique similar to optical homodyne detection is proposed to detect these extremely weak microwave signals.
A critical component in this setup is a 180° hybrid ring which acts as a microwave beam splitter. This hybrid ring will be connected to the resonator output and the weak microwave signal will be superimposed with a strong local oscillator (LO) signal of the same frequency. The constructive and destructive interference signals will give information about the single microwave photon. This detection scheme puts strong requirements on the hybrid ring. Both input ports need to be isolated at the photon (and LO) frequency, whereas a 3 dB coupling has to be achieved between the input and the output ports.
In this work experimental results of hybrid rings of different designs and materials will be presented and analyzed. A short introduction of qubits and the readout of weak microwave signals is given in the first chapter. The theoretical background of a microwave beam splitter is explained in chapter two, including transmission line theory, theory of the S-parameters and the theoretical behavior of the hybrid ring. After a short description of the fabrication process and the experimental setup scheme, the measurements are presented in chapters four and five. The results of the S-parameters are classified according to the two designs - the microstrip and the coplanar waveguide hybrid ring. At the end of chapter four measurements that were performed in Erlangen with a low temperature laser scanning microscope (LTLSM) are shown and discussed. Chapter five shows time domain measurements of the hybrid ring when applying two signals at the two input ports and detecting the constructive and destructive interference on the output ports. A conclusion is given in chapter six.
The appendix names detailed information about fabrication parameters, technical drawing and a few theoretical additions. A summary of some experiments in circuit quantum electrodynamics can also be found in the appendix.

Contents

1 Introduction **1**

2 Theoretical Background for the Hybrid Ring **5**
2.1 Superconductivity . . . 5
2.1.1 The London Equations and the Coherence Length . . . 6
2.1.2 Skin Depth and Surface Impedance . . . 7
2.2 Transmission Line Theory . . . 8
2.2.1 Introduction . . . 9
2.2.2 Microstrip . . . 11
2.2.3 Coplanar Waveguide . . . 15
2.2.4 Scattering Matrix . . . 18
2.3 Design of a 180° Hybrid Ring . . . 19
2.3.1 S-parameters of the Hybrid Ring . . . 20
2.4 Design of the Microstrip Hybrid Ring . . . 24
2.5 Design of the Coplanar Waveguide Hybrid Ring . . . 25

3 Sample Fabrication and Experimental Setup **27**
3.1 Sample Fabrication . . . 27
3.2 Sample Preparation . . . 29
3.3 Experimental Setup . . . 31

4 Measurements of the Hybrid Rings **35**
4.1 Microstrip Hybrid Ring . . . 41
4.1.1 Niobium on Sapphire and Silicon . . . 41
4.1.2 Gold on Silicon . . . 45
4.1.3 Copper on Teflon/Ceramic . . . 45
4.1.4 Reproducibility . . . 48
4.1.5 Line Thicknesses . . . 49
4.1.6 Ground Planes . . . 49
4.1.7 Contacting . . . 53
4.2 Measurements on CPW Hybrid Rings . . . 58
4.2.1 H 3: With and Without Inner Ground Plane . . . 58
4.2.2 CPW 1 . . . 61
4.2.3 CPW 2 . . . 61
4.3 LTLSM-Measurements . . . 64

5 Time Domain Measurement **71**

5.1 MITEQ Hybrid Ring . . . 71
5.1.1 Measurement . . . 71
5.1.2 Calculation . . . 74
5.2 MSH Cu . . . 77
5.3 Reference Measurement . . . 77

6 Conclusion **79**

A Quantum Bits and Circuit Quantum Electrodynamics **81**
A.1 Quantum Bit . . . 81
A.2 The Flux Qubit . . . 83
A.3 Circuit Quantum Electrodynamics . . . 85
A.4 Single Microwave Photon Source . . . 87

B Fluxoid Quantization in the Hybrid Ring **93**

C Fringe Field Factor **95**

D General Coplanar Waveguide **97**

E Fabrication Parameters **99**

F Technical Drawings **107**

1 Introduction

It has taken years of technological advancements to create modern computers. Charles Babbage (1791-1871) came up with the idea of a programmable engine and in 1941 Konrad Zuse created the first computer. Over time, computers have become more compact and considerably faster. However, the basic operation principle remains the same: to manipulate and interpret classical binary digits, or classical bits, into useful computational results. A classical "bit" is a fundamental unit of information. Classical bits are formed by a macroscopic physical system, e. g. as charge on a conductor or a hole in a punchcard. This means a classical bit must be either 0 or 1 (charge or no charge on the conductor, hole or no hole in the punchcard).
During the last years, it turned out that there are some problems that are to complicated to be solved with classical computers in a reasonable amount of time. In 1982, Feynman [3] introduced the idea of using a quantum system to simulate "physics", as he said, with computers. Here, the phrase "physics" includes quantum mechanical many body problems for which, in the case of classical computers, the calculation time increases exponentially with the size of the problem.
The fundamental unit of quantum information is the quantum bit or "qubit". In general, a qubit is a quantum mechanical two level system with basis states $|0\rangle$ and $|1\rangle$. Thus, any state $|\Psi(t)\rangle$ of the qubit can be interpreted as a superposition of these two basis states:

$$|\Psi(t)\rangle = \alpha(t)|0\rangle + \beta(t)|1\rangle.$$

Here, $\alpha(t)$ and $\beta(t)$ are complex amplitudes that have to satisfy the normalization condition

$$|\alpha(t)|^2 + |\beta(t)|^2 = 1.$$

More details about qubits are located in the appendix A.1.
Qubits can be realized by different physical systems. For example, in quantum optics ions are trapped and confined by electromagnetic fields and then can be manipulated by lasers. This has been achieved with eight qubits by H. Haeffner [4].
In a second ansatz cold atoms (Bose-Einstein-condensate) in optical lattices are used. These atoms can be entangled and manipulated in parallel. The optical lattice consists of micro traps that are created by standing laser fields.
The nuclear magnetic resonance (NMR) quantum computer uses the spins of atomic nuclei. In 1998, Chuang et al. [5] used such a "computer" to factorize the number 15 by applying the Shor algorithm [6]. However, NMR approaches lack scalability.
Besides semiconductor nanostructures like quantum dots, one of the most promising solid-state architectures for the realization of qubits is based on superconducting

quantum circuits [7]. The advantage of superconducting qubits over any other solid-state based quantum mechanical two-level system is the possibility to isolate the qubit from most of the environmental degrees of freedom and thereby reduce decoherence effects. This can be done because the superconducting ground state is separated by an energy gap ($\sim$ meV) from the quasiparticle excitation spectrum.
Physically, superconducting qubits are based on Josephson junctions that are arranged in different designs and different sizes. Depending on the ratio of the characteristic energy scales of the qubits Josephson junctions, the family of superconducting qubits can be divided into charge qubits, phase qubits and flux qubits (also known as persistent current qubits).
These superconducting quantum circuits have been investigated in numerous experiments [8, 9, 10, 11, 12, 13]. An overview of single and two qubit gates is given in reference [14]. In 2003, Yamamoto et al. [15] introduced a conditional gate operation using a pair of superconducting charge qubits.
The interaction between matter and light is of fundamental interest to physics. In quantum optics individual atoms with electrical dipole moment d are coupled to the vacuum state electric field E_0 of a cavity. When the Rabi frequency $\nu_{\mathrm{Rabi}} = 2dE_0/h$ exceeds the rates of relaxation and decoherence of both the atom and the field, the coherent oscillations of a single excitation between the atom and the cavity can be observed at ν_{Rabi}.
In 2004 A. Wallraff et al. [1] observed the coherent exchange of a single microwave photon between a superconducting charge qubit and an on-chip microwave cavity. The strong coupling of a superconducting qubit with an on-chip microwave cavity opened a new and fascinating field referred to as circuit quantum electrodynamics (c-QED). Sillanpää et al. [16] and Majer et al. [17] coupled two qubits via a resonator while Helmer et al. [18] proposed a cavity grid which allows to couple any two qubits on a grid independent of their distance and transfer information between them.
Houck, Schuster et al. [19] demonstrated how to utilize a specially designed qubit and resonator as an on-chip single-photon source. The qubit state can be mapped onto a photon which then acts as a "flying qubit" and transmits the quantum information across the chip. Thus, the information of the qubit is transferred onto a microwave photon. Details about this experiment can be found in the appendix A.4.
The readout of such microwave photons requires additional microwave elements that are working with low loss materials and at low temperatures since temperatures in the range of a few mK are needed. For many experiments the development of microwave technologies suitable for dealing with quantum signals is a crucial prerequisite. In this respect, it is of especial importance to investigate from which materials such microwave components should be made and how the device properties are influenced by this choice.
In 2007 Mariantoni et al. [20] proposed a measurement scheme that is expected to allow the detection of weak quantum signals, even at the level of single microwave photons. A crucial component is a device acting as a microwave beam splitter - the 180° hybrid ring. (see figure 1.1). It allows to create a coherent superposition of the quantum signal (S), entering the hybrid ring through port one, and the local

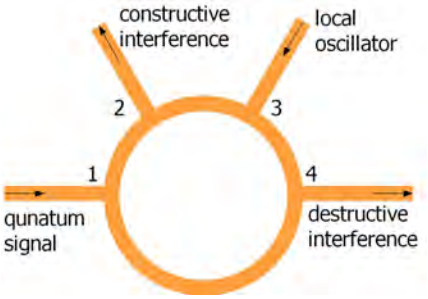

Figure 1.1: Sketch of the 180° hybrid ring. The incident signals at ports one and three are superimposed and the constructive and destructive interference is emitted through port two and four.

oscillator signal (LO), coming through port three with $\omega_S = \omega_{LO}$. The microwaves at the output ports two and four are amplified at low temperatures and downconverted to DC-signals. These DC-signals are proportional to the energy of the input signals and can be measured as voltages with an oscilloscope.
The classical theory of hybrid rings (see section 2.3) is extended to the quantum regime in analogy to an optical beam splitter. With the vacuum incident at ports two and four, the reduced quantum input-output relations of a lossless hybrid ring are

$$\begin{pmatrix} a_2 \\ a_4 \end{pmatrix} = \begin{pmatrix} r & t \\ -t^* & r^* \end{pmatrix} \begin{pmatrix} a_S \\ a_{LO} \end{pmatrix} \tag{1.1}$$

where r and t are the complex, frequency-dependent reflection and transmission coefficients, a_{LO} and a_S are the signal and LO port operators and a_2 and a_4 are the signals at the output ports two and four.
This detection scheme puts strong requirements on the hybrid ring. The signal at the *center frequency*, applied at port one is equally split into two components with a phase shift of 180° at port two and port four while, simultaneously, port three must be isolated. These conditions corresponds to $r = t = 1/\sqrt{2}$. The signal applied at port three is split into two in-phase components at ports two and four. This leads to a constructive interference at port two and a destructive interference at port four of the two applied signals ($a_2 = (a_S + a_{LO})/2$ and $a_4 = (-a_S + a_{LO})/2$). The center frequency f_0 is defined by the circumference U of the hybrid ring as $\lambda = 2U/3$ and $f_0 = v_p/\lambda$ where v_p is the phase velocity.
The behavior of the hybrid ring has been analyzed in detailed for normal conductors like gold and copper [21]. Since the applied signal at port one is a very weak microwave signal, it would be advantageous to work with superconductors. Several materials issues have to be resolved and the fabrication processes have to be optimized in order to get a working superconducting hybrid ring. As the measurements will show, a crucial step is the connection of the beam splitter with the environment.
Unlike commercial power splitters, the superconducting hybrid ring allows a superposition of quantum signals. In references [22, 23], hybrid rings using dielectric-

supported air-gapped microstrip lines are presented. These hybrid rings achieve an isolation magnitude of -40 dB. The measurements within this work will show that the superconducting hybrid rings achieve an isolation magnitude of -50 dB.
Within this work, microstrip hybrid rings of different designs, materials and line thicknesses were fabricated and analyzed. Additionally, three asymmetric coplanar waveguide hybrid rings were designed and their performance was compared to symmetric coplanar waveguide hybrid rings measured within a pervious work [24].
Chapter 2 gives an introduction to superconductivity and transmission line theory. Two of the major transmission line layouts - the microstrip line and the coplanar waveguide - will be described. In section 2.3.1 detailed dimensions of the fabricated hybrid rings are listed. An overview of the fabrication process and the setup scheme is located in chapter 3. Detailed fabrication parameters can be found in the appendix E.
The presented measurements are subdivided into frequency domain measurements (see chapter 4) and time domain measurements (see chapter 5). Chapter 4 presents S-parameter measurements of the different microstrip and coplanar waveguide hybrid rings. The last section of this chapter shows measurements using a low temperature laser scanning microscope. The time domain measurements of chapter 5 show the destructive and constructive interference of two applied signals at the hybrid ring. A conclusion of this diploma theses is located in chapter 6.

2 Theoretical Background for the Hybrid Ring

The design of the superconducting microwave beam splitter is influenced by superconductivity and transmission line theory. This chapter gives a short overview about the basic aspects of these two theories. A 180° hybrid ring acts as the proposed beam splitter and was therefore fabricated in the two major transmission line geometries - the microstrip and the coplanar waveguide which are explained in section 2.2.2 and 2.2.3. The properties of the hybrid ring and the parameters that are to consider, are presented in section 2.3.
Section 2.2.4 states a short introduction of S-parameters.

2.1 Superconductivity

Superconductivity was discovered in 1911 by Kamerlingh-Onnes. For many years, it was thought to be characterized simply of a vanishing electrical resistivity below a material dependent critical temperature. In 1933, Meissner and Ochsenfeld showed that superconductors are perfect diamagnets, meaning an external magnetic field is excluded from all but a thin penetration region close to the surface. Fritz and Heinz London gave the first phenomenological explanation for the electromagnetic properties [25] in 1935. The London theory is a dynamic theory that describes the superconductors locally. In 1950, the phenomenological Ginzburg-Landau theory of superconductivity was devised [26]. This theory, which combined Landau's theory of second-order phase transitions with a Schrödinger-like wave equation, successfully explained the macroscopic properties of superconductors. In particular, Abrikosov showed that the Ginzburg-Landau theory predicts the division of superconductors into the two categories now referred to as type I and type II superconductors.

In 1957, almost 50 years after the discovery of superconductivity, Bardeen, Cooper and Schrieffer published their microscopic theory of superconductivity [27].

During the last decades, superconductors have become more and more important in many different fields such as superconducting magnets and transmission line. Due to the fact that superconducting materials were used in this work, it is useful to give a short overview of the important quantities. Additional details are located in solid state books such as [28] or [29].

2.1.1 The London Equations and the Coherence Length

The behavior of a superconductor in external electromagnetic fields can be understood by using the two-fluid model. The free electrons of the superconductor are separated into two groups: the superconducting electrons with density n_s and the "normal" electrons with density n_n. The total density of the free electrons is $n = n_\mathrm{n} + n_\mathrm{s}$. The equation of motion for the superconducting electrons in an electromagnetic field is

$$\frac{\mathrm{d}\mathbf{v}_\mathrm{s}}{\mathrm{d}t} = \frac{e\mathbf{E}}{m} \tag{2.1}$$

where m is the electron mass, e the electron charge and $\mathbf{v}_\mathrm{s}$ is the superfluid velocity. At finite temperatures, there are thermal excitations in the superconductor whose velocity $\mathbf{v}_\mathrm{n}$ is described by the Drude model

$$\left(\frac{\partial}{\partial t} + \frac{1}{\tau_\mathrm{n}}\right)\mathbf{v}_\mathrm{n} = \frac{e\mathbf{E}}{m} \tag{2.2}$$

with $1/\tau_\mathrm{n}$ being the electron collision rate.
By using the supercurrent density $\mathbf{j}_\mathrm{s} = n_\mathrm{s} e \mathbf{v}_\mathrm{s}$ and the London coefficient $\Lambda = m/(n_\mathrm{s}e^2)$, (2.1) reads

$$\mathbf{E} = \frac{\mathrm{d}}{\mathrm{d}t}\left(\Lambda \mathbf{j}_\mathrm{s}\right). \tag{2.3}$$

This equation is called the *first London equation*. It describes the relation between an external electric field and the supercurrent. The relation between magnetic field and current is described by the *second London equation*. Since the derivation is a bit longer but not essential, only the results will be presented.
As already mentioned, an external applied magnetic field $\mathbf{H}(\mathbf{r})$ is not equal to zero in the whole superconductor. The magnetic flux penetrates the superconductor as described by the *second London equation*

$$\nabla \times (\Lambda \mathbf{j}_s) = -\mu_0 \mathbf{H}. \tag{2.4}$$

By applying Maxwell's equations, the second London equation is equal to

$$\mathbf{H} + \lambda_\mathrm{L}^2 \, \nabla \times (\nabla \times \mathbf{H}) = 0.$$

Consider a superconducting semispace $x > 0$ where the surface of the superconductor is assumed to be the $x = 0$ plane. A static external magnetic field $\mathbf{H}_0$ is orientated along the z axis. By using this symmetries and $\nabla \times (\nabla \times \mathbf{H}) = -\nabla^2 \mathbf{H}$ one gets

$$\frac{\mathrm{d}^2 H}{\mathrm{d}x^2} = \lambda_\mathrm{L}^{-2} H.$$

This leads to the solution

$$H = H_0 \exp\left(-\frac{x}{\lambda_\mathrm{L}}\right).$$

λ_L is called the London penetration depth and is defined as

$$\lambda_\mathrm{L}^2 = \frac{m}{\mu_0 n_\mathrm{s} e^2.} \tag{2.5}$$

Since λ_L depends on n_s, the London penetration depth is also depending on T. According to reference [28], a good approximation for the temperature dependence is given by the empirical formula

$$\lambda_\mathrm{L}(T) = \frac{\lambda_\mathrm{L}(0)}{\sqrt{1-(T/T_\mathrm{c})^4}}. \tag{2.6}$$

The London equations are local equations, they relate the local supercurrent density to the local vector potential.

2.1.2 Skin Depth and Surface Impedance

An oscillating electromagnetic field penetrates a conductor in a region given by the so called skin depth δ. This region influences the propagation of an electromagnetic wave.
The Maxwell's equations direct to

$$-\nabla^2 \mathbf{H} = -\mu_0 \sigma(\omega) \frac{\partial \mathbf{H}}{\partial t}$$

and with $\mathbf{H} \propto \exp(-i(kx - \omega t))$ one obtains

$$k^2 = -i\mu_0 \sigma(\omega)\omega.$$

For analyzing the penetration of the electromagnetic field it is useful to substitute

$$k = (1-i)/\delta(\omega)$$

with

$$\delta(\omega) = \sqrt{\frac{2}{\mu_0 \sigma(\omega)\omega}}.$$

The electromagnetic field then is

$$\mathbf{H} \propto \exp\left[\frac{-x}{\delta(\omega)} + i\left(\frac{x}{\delta(\omega)} + \omega\right)\right].$$

Thus, the oscillating electromagnetic field penetrates the conductor only to the depth $\delta(\omega)$.
Ohm's law is

$$\mathbf{j} = \sigma(\omega)\mathbf{E}$$

with $\sigma(\omega)$ the frequency-dependent conductivity. According to the two fluid model, where the total current density $\mathbf{j}$ consists of two components $\mathbf{j}_\mathrm{n}$ and $\mathbf{j}_\mathrm{s}$, this can be separated into two equations

$$\mathbf{j}_\mathrm{s} = \sigma_\mathrm{s}(\omega)\mathbf{E} \qquad \text{and} \qquad \mathbf{j}_\mathrm{n} = \sigma_\mathrm{n}(\omega)\mathbf{E}.$$

element	T_c [K]	$\lambda_L(4.2\,\mathrm{K})$	$\sigma(4.2\,\mathrm{K})$ [S/m]	$Z_S(4.2\,\mathrm{K})$ [Ω]
Nb	9.25	39.9 nm	$6.08 \cdot 10^7 + i\,6.64 \cdot 10^9$	$1.22 \cdot 10^{-5} - i\,2.67 \cdot 10^{-3}$

Table 2.1: T_c is given in [28]; the other values are calculated with (2.5), (2.7) and (2.8) at $\omega = 6\,\mathrm{GHz}$.

Together with $\mathbf{j}_s = n_s e \mathbf{v}_n$, $\mathbf{j}_n = n_n e \mathbf{v}_n$, $\mathbf{E} \propto \exp\left[\frac{-x}{\delta(\omega)} + i\left(\frac{x}{\delta(\omega)} + \omega\right)\right]$ and the equations (2.1) and (2.2) the superconducting and normal conducting conductivities are

$$\sigma_s(\omega) = \frac{n_s e^2}{-i\omega m} \qquad \text{and} \qquad \sigma_n(\omega) = \frac{n_n \tau_n e^2}{m} \frac{1}{1 - i\omega\tau_n}$$

The total conductivity is then defined as

$$\sigma(\omega) = \underbrace{\frac{n_s e^2}{-i\omega m}}_{\text{superconducting component}} + \underbrace{\frac{n_n \tau_n e^2}{m} \frac{1}{1 - i\omega\tau_n}}_{\text{normal component}} \tag{2.7}$$

Equation (2.7) describes the complex conductivity of a superconductor in a electromagnetic field with frequency ω.
The surface impedance is defined by

$$Z_S = \frac{E}{H}$$

with Maxwell equations and the assumption $\mathbf{H} \propto \exp(-i(kx - \omega t))$ it is possible to write the surface impedance as

$$Z_S(\omega) = \frac{1 - i}{\delta(\omega)\sigma(\omega)} = R_S + i \cdot X_S \tag{2.8}$$

The real part of the impedance R_S reflects the energy dissipation due to heating, while the imaginary part X_S is the inductive resistance. Since $\sigma(\omega)$ depends on n_n and n_s, Z_S is temperature dependent.
Table 2.1 lists the important values for niobium, which is the only superconducting material used within this work. The value for $1/\tau_n$ is 370 GHz and n_s is given as $0.89 \cdot 10^{28}$ for $T = 4.2\,\mathrm{K}$ [24].

2.2 Transmission Line Theory

Transmission line theory describes wave propagation in waveguides such as microwave tubes, which are more preferred for low frequencies, hollow-pipe waveguides for higher frequencies and surface waveguides. Two typical types of surface waveguides are the coplanar waveguide and the microstrip which are used within this work. A summary of different types of waveguides is given in reference [30]. First, an introduction of transmission line theory and wave propagation will be given before the microstrip and the coplanar waveguide design are described.

2.2.1 Introduction

The transmission line is described by a satisfactory analysis which can be carried out by treating the transmission line as a network. Current and voltage waves which may propagate along the line can be found analytically by using the network's parameters. In this section the characteristic impedance and the effective permittivity will be derived by applying Kirchhoff's law.

Lumped Element Circuit Model

In general, a transmission line can be represented by a two-wire line. A piece of infinitesimal length Δz is shown in figure 2.1 and can be modeled as a lumped-element circuit which is shown in figure 2.2 with

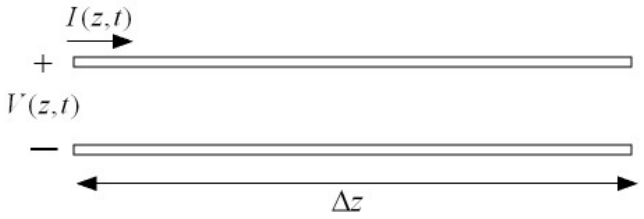

Figure 2.1: An infinitesimal length of transmission line

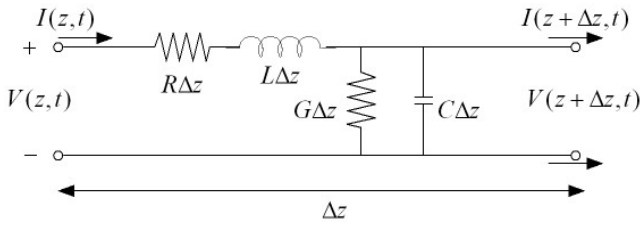

Figure 2.2: An infinitesimal length of transmission line modeled as a lumped-element circuit

R = series resistance per unit length, for both conductors, in Ω/m
L = series inductance per unit length, for both conductors, in H/m
G = shunt conductance per unit length, in S/m
C = shunt capacitance per unit length, in F/m.

Applying Kirchhoff's laws, taking the limit $\Delta z \to 0$ and assuming $V(z,t) = V(z)\exp(i\omega t)$ and $I(z,t) = I(z)\exp(i\omega t)$ leads to two equations

$$\frac{dV(z)}{dz} = -(R + i\omega L)I(z) \tag{2.9}$$

$$\frac{dI(z)}{dz} = -(G + i\omega C)V(z) \tag{2.10}$$

These equations are also known as the *Telegrapher's Equations* and were developed by Oliver Heaviside in 1887.

Wave Propagation

The Telegrapher's equations can be converted to two one-dimensional wave equations. By the definition of a complex propagation constant

$$\gamma = \alpha + i\beta = \sqrt{(R + i\omega L)(G + i\omega C)} \tag{2.11}$$

where α is the damping constant of the propagating wave with the wave number β, the general solutions of the Telegrapher's equations can be written as

$$V(z) = V_0^+ e^{\gamma z} + V_0^- e^{-\gamma z} \tag{2.12}$$

and

$$I(z) = I_0^+ e^{\gamma z} + I_0^- e^{-\gamma z} \tag{2.13}$$

The characteristic impedance is defined as

$$\frac{V_0^+}{I_0^+} = Z_0 = \frac{-V_0^-}{I_0^-} \tag{2.14}$$

By substituting (2.9) into (2.12) and using (2.13) Z_0 is

$$Z_0 = \frac{R + i\omega L}{\gamma} = \sqrt{\frac{R + i\omega L}{G + i\omega C}}\,.$$

With the substitution for I_0^+ and I_0^- in (2.13), the time-dependent solution for $V(z,t)$ can be expressed as

$$V(z,t) = |V_0^+| \cos(\omega t - \beta z + \Phi^+) e^{-\alpha z} + |V_0^-| \cos(\omega t + \beta z + \Phi^-) e^{\alpha z} \tag{2.15}$$

$\Phi^\pm$ is the phase angle of the complex voltage $V_0^\pm$.
Since the wavelength is defined as the distance between two successive maxima at a fixed instant of time and $[\omega t - kz] - [\omega t - k(z + \lambda)] = 2\pi$, one finds an expression for the wavelength

$$\lambda = \frac{2\pi}{\beta} \tag{2.16}$$

and the phase velocity

$$v_\mathrm{p} = \frac{\omega}{\beta} = \lambda f. \tag{2.17}$$

This is the solution for a general lossy transmission line, where the propagation constant and characteristic impedance are complex quantities.

Lossless Line

In the case of low loss effects, which is a good approximation for superconductors at low temperatures, the above results can be simplified by setting the $R = G = 0$. Then the attenuation α is zero and the propagation constant γ can be written as

$$\gamma = i\beta = i\omega\sqrt{LC}\,.$$

Thus, the characteristic impedance can be written as

$$Z_0 = \sqrt{\frac{L}{C}} \tag{2.18}$$

which is a real number. Analogous to the general solution the wavelength is

$$\lambda = \frac{2\pi}{\beta} = \frac{2\pi}{\omega\sqrt{LC}} \tag{2.19}$$

and the phase velocity is

$$v_\mathrm{p} = \frac{\omega}{\beta} = \frac{1}{\sqrt{LC}}. \tag{2.20}$$

It is also possible to give an expression for the characteristic impedance depending on the effective permittivity of the system. With (2.20) and (2.18) the impedance can be written as

$$Z_0 = \frac{1}{Cv_\mathrm{p}} = Lv_\mathrm{P} \tag{2.21}$$

where c is the velocity of light. Since the effective permittivity $\varepsilon_{\mathrm{eff,q}}$ is defined by

$$\varepsilon_{\mathrm{eff,q}} = c^2 v_\mathrm{p}^2 \tag{2.22}$$

Z_0 can be calculated as

$$Z_0 = \frac{\sqrt{\varepsilon_{\mathrm{eff,q}}}}{cC} = \frac{Lc}{\sqrt{\varepsilon_{\mathrm{eff,q}}}} \tag{2.23}$$

The characteristic impedance is a very important property of a waveguide. Most of the industrially fabricated devices are matched with $Z_0 = 50\,\Omega$. This matching requires also a $50\,\Omega$ alignment of the hybrid ring.

2.2.2 Microstrip

The microstrip is one of the most popular types of planar transmission lines because it can be fabricated by a lithography process (see section 3.1). It consists of a single conducting strip of width w and thickness t_s suspended on a dielectric substrate of thickness h. Figure 2.3 shows the cross section of a microstrip transmission line. The ground plane is on the opposite site of the substrate and has a thickness t_g.
If the dielectric was not present, one could think of the line as a two-wire line consisting of two flat strip conductors separated by distance $2h$. In this case, one would achieve a simple TEM wave with $v_\mathrm{p} = c$. The presence of the dielectric

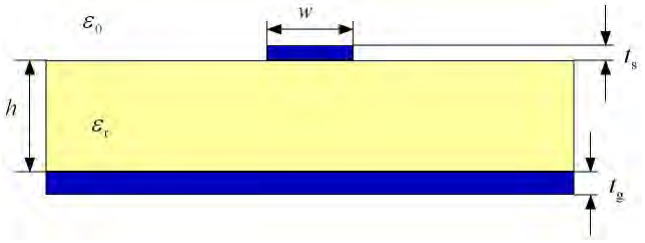

Figure 2.3: The profile of a microstrip line with ground plane on the opposite side of the substrate.

complicates the behavior of microstrip lines. The microstrip line cannot support a pure TEM wave since the phase velocity of a TEM wave in the dielectric region $c/\sqrt{\varepsilon_r}$ differs from the one in air c.
In most practical applications the dielectric region is very thin ($h \ll \lambda$) and the fields can be approximated by the quasistatic solution:

$$v_p = \frac{c}{\sqrt{\varepsilon_{eff,q}}} \tag{2.24}$$

which is equal to (2.22).
The calculation of the effective permittivity requires a differentiation between the superconducting and non superconducting case. The calculated values, that are used within this work can be found in table 2.2.

Non-superconducting Microstrip Transmission Line

According to reference [21] the effective permittivity for a microstrip transmission line is

$$\varepsilon_{eff,q} = \frac{1}{2}\left[(\varepsilon_r + 1) + (\varepsilon_r - 1)\left(\sqrt{1 + 12h/w}\right)^{-1}\right] \tag{2.25}$$

The effective dielectric constant can be interpreted as the dielectric constant of a homogeneous medium that replaces both the air and the dielectric regions of the microstrip. The characteristic impedance can be calculated to be

$$Z_0 = \begin{cases} 60/\sqrt{\varepsilon_{eff,q}} \cdot \ln\left(8h/w + w/(4h)\right) & w/h \leq 1 \\ 120\pi/\sqrt{\varepsilon_{eff,q}} \cdot [w/h + 1.393 + 0.667\ln(w/h + 1.444)]^{-1} & w/h > 1 \end{cases} \tag{2.26}$$

Dispersion Relation

The dispersion properties have been studied theoretically, for example by references [31] and [32]. Kobayashi [33] proposed a dispersion formula that promises an accuracy better than 0.6 percent in the range $0.1 < w/h \leq 10$, $1 < \varepsilon_{eff,q} \leq 128$. This

accuracy was determined by comparing the calculated dispersion values $\varepsilon_{\text{eff}}(f)$ with a numerical model [34]. The expression for the frequency dependent permittivity is

$$\varepsilon_{\text{eff}}(f) = \varepsilon_{\text{r}} - \frac{\varepsilon_{\text{r}} - \varepsilon_{\text{eff,q}}}{1 + (f/f_{50})^m}$$

where

$$f_{50} = \frac{f_{\text{K,TM}_0}}{0.75 + \left(0.75 - \frac{0.332}{\varepsilon_{\text{r}}^{1.73}}\right)\frac{w}{h}}$$

$$f_{\text{K,TM}_0} = \frac{c\tan^{-1}\left[\varepsilon_{\text{r}}\sqrt{\frac{\varepsilon_{\text{eff,q}}-1}{\varepsilon_{\text{r}}-\varepsilon_{\text{eff,q}}}}\right]}{2\pi h\sqrt{\varepsilon_{\text{r}} - \varepsilon_{\text{eff,q}}}}$$

$$m = m_0 m_{\text{c}}$$

$$m_0 = 1 + \frac{1}{1+\sqrt{w/h}} + 0.32\left(\frac{1}{1+\sqrt{w/h}}\right)^3$$

$$m_{\text{c}} = \begin{cases} 1 + 1.4/(1+w/h)\left[0.15 - 0.235\exp\left(-0.45 f/f_{50}\right)\right] & (w/h \leq 0.7) \\ 1 & (w/h \geq 0.7) \end{cases}$$

The frequency dependence of the effective permittivity is illustrated in figure 2.4. These calculations are done with the permittivity of sapphire $\varepsilon_{\text{r}} = 11.6$ and the height $h = 525\,\mu\text{m}$ of the sapphire substrate.

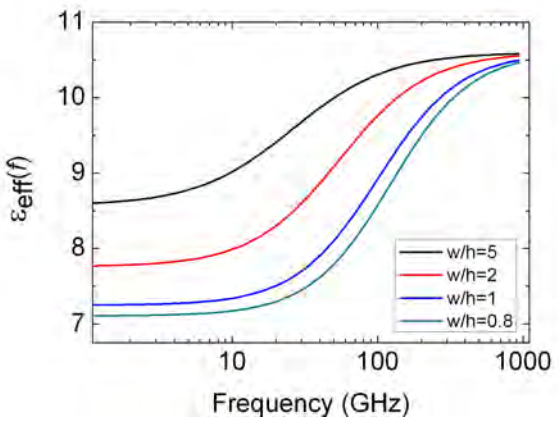

Figure 2.4: The frequency dependence of $\varepsilon_{\text{eff}}(f)$ for the electric permittivity $\varepsilon_{\text{r}} = 11.9$.

Since the effective permittivity does not change up to 10 GHz, according to figure 2.4, and the center frequency of the hybrid ring will be 6 GHz, it can be assumed that the effective permittivity is constant.

Superconducting Microstrip Transmission Line

The London penetration depth λ_L influences the inductance L of the microstrip line . As shown in section 2.2.1, the characteristic impedance can be calculated as $Z_0 = \sqrt{L/C}$. Therefore Z_0 depends on λ. In reference [35] W. H. Chang presents an analytical formula for the inductance L and the capacitance C. The complete solution is applicable for $w/h > 1$ and has been obtained by using a conformal mapping technique.
In general, the inductance per unit length of a superconductor consists of two different parts: the *internal* and *external* inductance. The external inductance represents the contribution due to the external field while the internal inductance contains the parts of the strip conductor and the ground plane.
The inductance L is obtained by evaluating the fluxoid of the strip line using the integration path as shown in figure 2.5. The ansatz

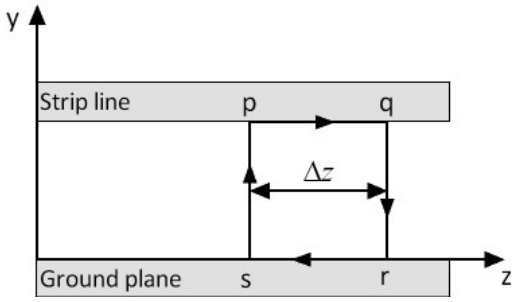

Figure 2.5: Integration path to calculate the inductance L.

$$L = \frac{1}{I}\frac{1}{\Delta z}\int_{pqrsp} (\mathbf{A} + \mu_0 \lambda_\mathrm{L}^2 \mathbf{J})\,\mathrm{dl}$$

leads to

$$L_\mathrm{sc} = \frac{\mu_0}{wK(w,h,t_\mathrm{s})}\left[h + \lambda_\mathrm{L,s}\coth\left(\frac{t_\mathrm{s}}{\lambda_\mathrm{L,s}}\right) + \lambda_\mathrm{L,g}\coth\left(\frac{t_\mathrm{g}}{\lambda_\mathrm{L,g}}\right)\right] \tag{2.27}$$

where $\lambda_\mathrm{L,s}$ and $\lambda_\mathrm{L,g}$ are the respective penetration depths of the strip line and the ground plane. In this diploma thesis, the superconducting ground plane consists of the same material as the line $\lambda_\mathrm{L,s} = \lambda_\mathrm{L,g} = \lambda_\mathrm{L}$. $K(w,h,t_\mathrm{s})$ is the so called fringe field factor and is 3.8 for $w = 420\,\mu$m, $h = 525\,\mu$m and $t = 200\,$nm. The whole calculation of the fringe factor can be found in the appendix.
According to reference [35] the capacitance per unit length of a superconducting strip line is given as

$$C_\mathrm{sc} = \frac{\varepsilon_\mathrm{eff}(f)\varepsilon_0 w}{h} K(w,h,\mathrm{ts})$$

Values for the capacitance and the inductance are required to calculate the characteristic impedance $Z_{0,\mathrm{sc}} = \sqrt{L_\mathrm{sc}/C_\mathrm{sc}}$. Table 2.2 shows the characteristic impedances

material	w [μm]	h [μm]	t_s [nm]	ε_r	$\varepsilon_{eff,q}$	ε_{eff}(6 GHz)	Z_0	$Z_{0,sc}$
Al_2O_3	490	500	200	10.6	7.23	7.27	47.5	42.6
Si	420	525	200	11.9	7.93	7.97	49.5	43.9
PTFE/ceramic	490	605	17500	10.2	6.86	6.89	52.9	50.4

Table 2.2: Calculated values of the characteristic impedance for a microstrip line with niobium as conductor at 4 K.

for some dimensions that were used for the hybrid rings. The dimensions of the fabricated hybrid rings were chosen to achieve $Z_0 \approx 50$.

2.2.3 Coplanar Waveguide

In 1969, C. P. Wen proposed the coplanar waveguide (CPW) [36]. The coplanar waveguide promises lower losses than the microstrip. In contrast to the microstrip, the coplanar waveguide has the center strip and the ground plane on the same side of the substrate. The center strip with width w is separated from the ground lateral planes by a gap g. The aspect ratio is defined as $w/(w+2g)$.
The dimensions of the center strip, the gap of the conductors, the thickness and dielectric constant of the substrate have influence on the characteristic impedance (Z_0) and the effective dielectric constant ($\varepsilon_{eff,q}$).
CPWs have been analyzed theoretically and in experiments in the last years. An overview of the different types of CPWs is given in reference [37]. The impedance is also dependent on the London penetration depth, therefore it is useful to give expressions for both the superconducting and non-superconducting case. Some calculated values for the dimensions that were used within the experiments are given in table 2.3.

Non-superconducting Coplanar Waveguide

A coplanar waveguide, see figure 2.6, consists of a substrate, a conducting line and the ground plane on the same side of the substrate. Similar to the microstrip, one has to compute the effective permittivity and the characteristic impedance. The general case is calculated in reference [37] or [38]. The formulas for the general case are included in the appendix D.

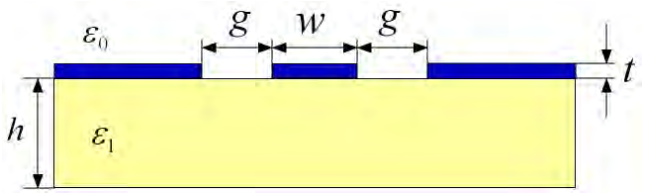

Figure 2.6: Profile of a one-layered unshielded coplanar waveguide transmission line

The effective permittivity is given as

$$\varepsilon_{\mathrm{eff,q}} = 1 + \frac{(\varepsilon_1 - 1)}{2} \frac{K(k_1)}{K(k_1')} \frac{K(k_0)}{K(k_0')}$$

with the complete elliptic integrals of first kind $K(x)$, where k_j and k_j' ($j \in \{0, 1, 2\}$) are defined as

$$k_1 = \frac{\sinh\left(\frac{\pi w}{4h}\right)}{\sinh\left(\frac{\pi}{2h}\left(w/2 + g\right)\right)},$$

$$k_0 = \frac{w}{w + 2g}$$

and

$$k_j' = \sqrt{1 - k_j^2}.$$

The capacitance per unit length and the characteristic impedance are

$$C = 4\varepsilon_0 \varepsilon_{\mathrm{eff,q}} \frac{K(k_0)}{K(k_0')}, \tag{2.28}$$

$$Z_0 = \frac{30\pi}{\sqrt{\varepsilon_{\mathrm{eff,q}}}} \frac{K(k_0')}{K(k_0)}. \tag{2.29}$$

Dispersion Relation

A formula for the effective capacitance versus the frequency has been derived by Hasnain et al. in reference [39] and Yamashita et al. in reference [40]. The computed expression is valid up to the terahertz regime and is given by

$$\sqrt{\varepsilon_{\mathrm{eff}}(f)} = \sqrt{\varepsilon_{\mathrm{eff,q}}} + \frac{\sqrt{\varepsilon_1} - \sqrt{\varepsilon_{\mathrm{eff,q}}}}{1 + a\, F^{-1.8}}. \tag{2.30}$$

F is defined by $F = f/f_{\mathrm{TE}}$ where $f_{\mathrm{TE}} = c/(4h\sqrt{\varepsilon_1 - 1})$ is the cut-off frequency for the lowest-order TE mode. The factor a is computed by the expression

$$\log(a) = u \log\left(\frac{w}{g}\right) + v$$

where u and v depend on the substrate thickness h (see figure 2.6)

$$u \approx 0.54 - 0.64q + 0.015q^2$$

$$v \approx 0.43 - 0.86q + 0.54q^2$$

with $q = \log(w/h)$.
This dispersion relation behaves like shown in figure 2.7 with an accuracy within 5 % compared to a computer simulation for the parameters $0.1 < w/g < 5$, $0.1 < w/h < 5$, $1.5 < \varepsilon_1 < 50$, $0 < f/f_{\mathrm{TE}} < 10$.

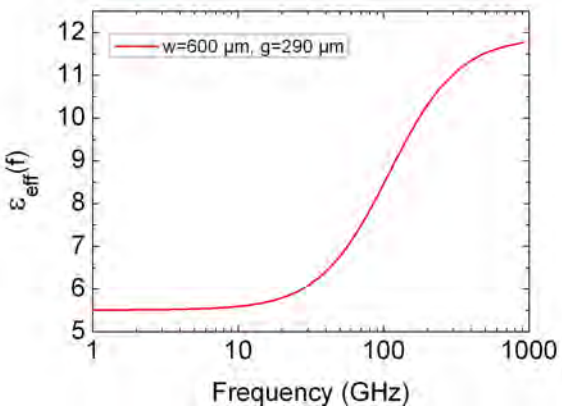

Figure 2.7: Frequency dependence of $\varepsilon_{\text{eff}}(f)$ for the parameters $w = 600\,\mu$m, $g = 290\,\mu$m, $h = 500\,\mu$m and $\varepsilon_{\text{r}} = 11.9$ that were used for the arms of two of the three designed coplanar waveguide hybrid rings.

Superconducting Coplanar Waveguide

Rauch et al. [41] calculated the characteristic impedance of a superconducting coplanar waveguide. The inductance is the sum of an external inductance L_{ext}, which is

$$L_{\text{ext}} = \frac{\mu_0}{4}\frac{K(k_0')}{K(k_0)} \tag{2.31}$$

and an internal inductance, which takes the superconductivity into account:

$$L_{\text{int}} = \mu_0\lambda_{\text{L}}\frac{D}{4AEK(k_0)}\left(\frac{1.7}{\sinh[t/(2\lambda_{\text{L}})]} + \frac{0.4}{\sqrt{[(B/A)^2-1][1-(B/E)]^2}}\right) \tag{2.32}$$

with

$$A = -\frac{1}{\pi} + \frac{1}{2}\sqrt{\left(\frac{2t}{\pi}\right)^2 + w^2}$$

$$B = \frac{w^2}{2A}$$

$$D = B - \frac{t}{\pi} + \sqrt{\left(\frac{t}{\pi}\right)^2 + g^2}$$

$$E = \frac{2t}{\pi} + D.$$

The geometric parameters are the same as in figure 2.6. With (2.23) it is possible to calculate Z_0 by using the effective capacitance as it is given in (2.30). The impedances values of silicon and sapphire show no difference between Z_0 and $Z_{0,\text{sc}}$ up to the first decimal place.

material	w [mm]	g [mm]	h [μm]	t_s [nm]	ε	$\varepsilon_{\text{eff,q}}$	Z_0	$Z_{0,\text{sc}}$
Si	0.6	0.29	525	200	11.9	5.51	50.9	50.9
Al_2O_3	0.200	0.125	500	100	10.6	5.64	54.1	54.3

Table 2.3: Calculated $\varepsilon_{\text{eff,q}}$, Z_0 and $Z_{0,\text{sc}}$ for a coplanar waveguide line with niobium as conductor at 4 K. Z_0 and $Z_{0,\text{sc}}$ do not differ significantly for each material.

2.2.4 Scattering Matrix

In general Voltages, currents and impedances are hard to measured in a direct manner at microwave frequencies. A parameter that can be measured directly is the transmission coefficient of an applied signal. This can be measured through a N-port device by comparing the amplitude and the phase of the transmitted wave to the values of the incident wave. The matrix describing this relationship is called the scattering matrix. An incident wave is partly reflected and partly transmitted. The reflected and transmitted waves can be demonstrated in the optical regime by reflections and transmissions for a lens as shown in figure 2.8. In transmission line the light beam is replaced by the microwave beam and the lens is replaced by the device under test (DUT).

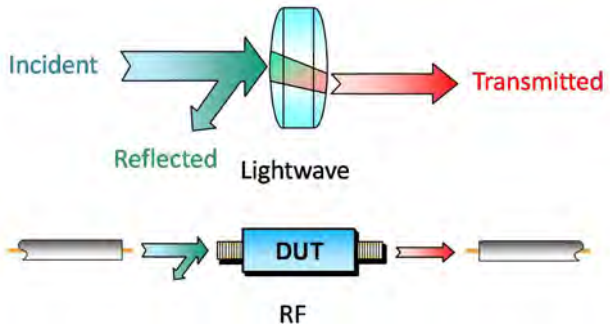

Figure 2.8: Representation of reflected and transmitted (a) lightwave and (b) microwave

Consider a N-port network like the one in figure 2.9. If a wave with an associated equivalent voltage V_k^+ is incident on port k, a reflected wave $V_k^- = S_{kk}V_k^+$ is produced in line k where S_{kk} is the scattering coefficient. The wave can also be transmitted, or reflected at other ports of the network with $V_n^- = S_{nk}V_k^+$ for $n = 1, 2, ..., N$, $n \neq k$ where S_{nk} is a transmission coefficient from line k to line n.
This leads to

$$\begin{bmatrix} V_1^- \\ V_2^- \\ \dots \\ V_N^- \end{bmatrix} = \begin{bmatrix} S_{11} & S_{12} & \dots & S_{1N} \\ S_{21} & S_{22} & \dots & S_{2N} \\ \dots & \dots & \dots & \dots \\ S_{N1} & S_{N2} & \dots & S_{NN} \end{bmatrix} \begin{bmatrix} V_1^+ \\ V_2^+ \\ \dots \\ V_N^+ \end{bmatrix}.$$

$\overleftrightarrow{S}$ is the so called scattering matrix. A specific element of the S-matrix can be

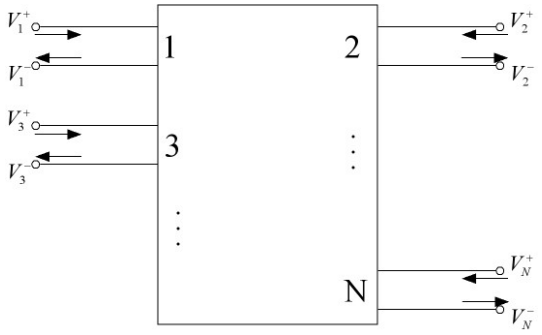

Figure 2.9: N-port network

determined as

$$S_{kl} = \left.\frac{V_k^-}{V_l^+}\right|_{V_j^+=0 \text{ for } j\neq l}$$

For practical application it is useful to calculate the S-parameters in decibel:

$$S[\text{dB}]_{kl} = 20 \cdot \log_{10}(|S_{kl}|)$$

2.3 Design of a 180° Hybrid Ring

The 180° hybrid ring is a four port network where the ports are numbered clockwise from one to four as shown in figure 2.10. At the center frequency f_0 acts as a beam splitter by emitting the constructive and destructive interference at ports two and four of two applied signals at ports one and three.
The phase difference of a wave is $\theta = \beta U/6 = 2\pi\beta R/6$ between ports one and two, two and three and three and four where $U = 2\pi R$ is the circumference of the ring. β is the wave number that was defined in section 2.2.1. Between port one and four there is a phase difference of 3θ. In the case of $\theta = \pi/2$ the signal applied at port one is evenly split into two components with the same amplitude, one wave travelling clockwise and the other one counter clockwise around the ring. These two waves will interfere constructively at ports two and four and destructively at port three. As a consequence ports two and four are 3 dB coupled to port one, whereas port three is isolated from port one. The phase shift of the waves at port four and two is 180°. By applying a signal through port three, this is split into two in-phase components at ports two and four. Therefore, when applying two signals at port one and three, constructive interference occurs at port two and destructive interference is formed at port four.
Hybrid rings were designed in the major transmission line designs - the microstrip (MS) and coplanar waveguide (CPW) design. The CPW design was chosen because of the design of the high-Q line resonator. As mentioned in the introduction, the qubit will be coupled with a resonator which will emit single microwave photons to

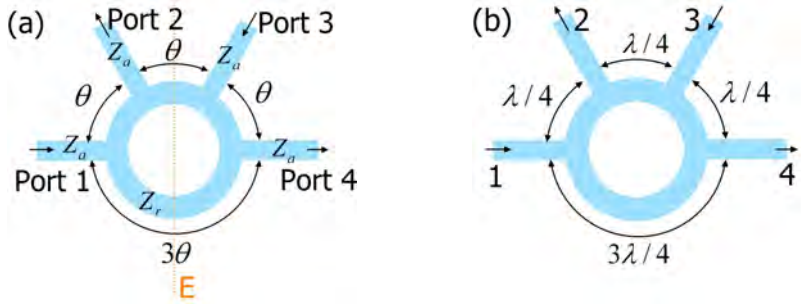

Figure 2.10: Schematic of the 180° hybrid ring (a) general case with the axis of symmetry E (b) case of $\theta = \pi/2$.

the hybrid ring. One expects a better coupling of two CPW devices than of two devices with different design and therefore less losses. Nevertheless, the MS hybrid ring was also measured since the layout is simpler to calculate (see section 2.2.2 compared to 2.2.3) and promises better results.

2.3.1 S-parameters of the Hybrid Ring

The S-parameters of the hybrid ring can be derived by studying the symmetric and antisymmetric cases of applied voltages. The symmetric and antisymmetric excitation of the hybrid ring is in reference to the symmetry plane E as shown in figure 2.10(a). Once having found the corresponding S-parameters, the superposition of this solution directs to the full 4×4-S-matrix of the hybrid ring for the general excitation.
Preconditions for the symmetric case are incident waves V_a^+ and V_b^+ at ports one and two and incident waves V_a^+ and V_b^+ at ports four and three. This leads to the solutions

$$\begin{bmatrix} V_1^- \\ V_2^- \end{bmatrix} = \begin{bmatrix} S_{11}^{\mathrm{oc}} & S_{12}^{\mathrm{oc}} \\ S_{21}^{\mathrm{oc}} & S_{22}^{\mathrm{oc}} \end{bmatrix} \begin{bmatrix} V_a^+ \\ V_b^+ \end{bmatrix}$$

and

$$\begin{bmatrix} V_4^- \\ V_3^- \end{bmatrix} = \begin{bmatrix} S_{11}^{\mathrm{oc}} & S_{12}^{\mathrm{oc}} \\ S_{21}^{\mathrm{oc}} & S_{22}^{\mathrm{oc}} \end{bmatrix} \begin{bmatrix} V_a^+ \\ V_b^+ \end{bmatrix}.$$

Analogous the antisymmetric case when the incident wave at port four and three are $-V_a^+$ and $-V_b^+$. The solutions here are

$$\begin{bmatrix} V_1^- \\ V_2^- \end{bmatrix} = \begin{bmatrix} S_{11}^{\mathrm{sc}} & S_{12}^{\mathrm{sc}} \\ S_{21}^{\mathrm{sc}} & S_{22}^{\mathrm{sc}} \end{bmatrix} \begin{bmatrix} V_a^+ \\ V_b^+ \end{bmatrix}$$

and

$$\begin{bmatrix} V_4^- \\ V_3^- \end{bmatrix} = \begin{bmatrix} S_{11}^{\mathrm{sc}} & S_{12}^{\mathrm{sc}} \\ S_{21}^{\mathrm{sc}} & S_{22}^{\mathrm{sc}} \end{bmatrix} \begin{bmatrix} -V_a^+ \\ -V_b^+ \end{bmatrix}.$$

By superimposing the symmetric and antisymmetric waves, the S-matrices can be written as

$$\begin{bmatrix} V_1^- \\ V_2^- \end{bmatrix} = \begin{bmatrix} S_{11}^{\mathrm{oc}} + S_{11}^{\mathrm{sc}} & S_{12}^{\mathrm{oc}} + S_{12}^{\mathrm{sc}} \\ S_{21}^{\mathrm{oc}} + S_{21}^{\mathrm{sc}} & s_{22}^{\mathrm{oc}} + S_{22}^{\mathrm{sc}} \end{bmatrix} \begin{bmatrix} V_a^+ \\ V_b^+ \end{bmatrix} = \begin{bmatrix} S_{11} & S_{12} \\ S_{21} & s_{22} \end{bmatrix} \begin{bmatrix} V_a^+ \\ V_b^+ \end{bmatrix}$$

and

$$\begin{bmatrix} V_4^- \\ V_3^- \end{bmatrix} = \begin{bmatrix} S_{11}^{\mathrm{oc}} - S_{11}^{\mathrm{sc}} & S_{12}^{\mathrm{oc}} - S_{12}^{\mathrm{sc}} \\ S_{21}^{\mathrm{oc}} - S_{21}^{\mathrm{sc}} & s_{22}^{\mathrm{oc}} - S_{22}^{\mathrm{sc}} \end{bmatrix} \begin{bmatrix} V_a^+ \\ V_b^+ \end{bmatrix} = \begin{bmatrix} S_{41} & S_{42} \\ S_{31} & s_{32} \end{bmatrix} \begin{bmatrix} V_a^+ \\ V_b^+ \end{bmatrix}$$

The other S-parameters are obtained by symmetry considerations: $S_{11} = S_{44}$, $S_{12} = S_{43}$, $S_{13} = S_{42}$, $S_{22} = S_{33}$, and $S_{kl} = S_{lk}$. Thus, the four-port hybrid can be characterized in terms of two sets of two-port scattering-matrix parameters which ends in a 4×4 scattering matrix.

$$\overleftrightarrow{S} = \begin{bmatrix} S_{11} & S_{12} & S_{42} & S_{41} \\ S_{12} & S_{22} & S_{32} & S_{42} \\ S_{42} & S_{32} & S_{22} & S_{12} \\ S_{41} & S_{42} & S_{12} & S_{11} \end{bmatrix}$$

The derivation for the two-port S-parameters can be found in [37], the results are

$$S_{11}^{\mathrm{oc}} = \frac{1}{\Delta}[Y_{\mathrm{a}}^2 - Y_{\mathrm{r}}^2 + B_1 B_2 - Y_{\mathrm{r}}(B_1 + B_2)\cot(\theta) + iY_{\mathrm{a}}(B_2 - B_1)]$$

$$S_{12}^{\mathrm{oc}} = S_{21}^{\mathrm{oc}} = -\frac{2iY_{\mathrm{a}}Y_{\mathrm{r}}\csc(\theta)}{\Delta}$$

$$S_{22}^{\mathrm{oc}} = S_{11}^{\mathrm{oc}} + \frac{2iY_{\mathrm{a}}(B_1 - B_2)}{\Delta}$$

with

$$\Delta = Y_{\mathrm{a}}^2 - B_1 B_2 + Y_1\mathrm{r}(B_1 + B_2)\cot(\theta) + Y_1^1 + iY_{\mathrm{a}}(B_1 + B_2 - 2Y_{\mathrm{r}}\cot(\theta))$$

$$B_1 = -Y_{\mathrm{r}}\tan\left(\frac{3\theta}{2}\right)$$

$$B_2 = Y_{\mathrm{r}}\tan\left(\frac{\theta}{2}\right).$$

Y_{a} and Y_{r} the reciprocal of the characteristic impedance of the arms Z_{a} and of the ring Z_{r}.
S_{11}^{sc}, S_{22}^{sc} and $S_{21}^{\mathrm{sc}} = S_{12}^{\mathrm{sc}}$ are obtained by replacing B_1 by $B_3 = -Y_{\mathrm{r}}\cot(3\theta/2)$ and B_2 by $B_4 = -Y_{\mathrm{r}}\cot(\theta/2)$.
The special case $\theta = \pi/2$ leads to

$$S_{31} = S_{42} = 0$$

$$S_{kk} = \frac{Y_\mathrm{a}^2 - 2Y_\mathrm{r}^2}{Y_\mathrm{a}^2 + 2Y_\mathrm{r}^2} \qquad \text{for} \quad k \in \{1,2,3,4\}$$

$$S_{12} = S_{34} = -S_{41} = S_{32} = -\frac{2iY_\mathrm{a}Y_\mathrm{r}}{Y_\mathrm{a}^2 + 2Y_\mathrm{r}^2}.$$

As expected, at the center frequency ports one and three and ports two and four are isolated. Ports two and four are coupled with port one but the output at port two is 180° out of phase with the output at port four.
$\theta = \pi/2$ leads to $\lambda_0 = V_\mathrm{p}/\beta_0$ which leads to the center frequency f_0 being

$$f_0 = \frac{v_\mathrm{p}}{\lambda_0} = \frac{v_\mathrm{p}\beta_0}{2\pi} = \frac{6v_\mathrm{p}\theta}{2D\pi^2} = \frac{3v_\mathrm{p}}{2D\pi}$$

where D is the diameter of the hybrid ring and v_p the phase velocity.
The matching of the ring impedance to the impedance of the arms of the hybrid ring is done by choosing $Y_\mathrm{a}^2 = 2Y_\mathrm{r}^2$ or $Z_\mathrm{r} = \sqrt{2}Z_\mathrm{a}$: the power entering the hybrid ring at port one or three is equally divided into two components with a phase shift of 180° at ports two and four. The matching of the hybrid ring to the environment requires $Z_\mathrm{a} = 50\,\Omega$. The S_{ij}-parameter is measured by applying a signal at port j and detecting the transmitted signal at port i. To avoid unwanted reflections at the other two ports, these ports has to be terminated. Because the lines of the cables and the arms of the hybrid rings are $50\,\Omega$ matched, $50\,\Omega$ resistances are used to terminated and absorb the microwave signals at the unmeasured ports.
When the hybrid ring is $50\,\Omega$ matched, it is also called 3 dB directional coupler. Then, at the center frequency the four-port scattering matrix simplifies to

$$\overleftrightarrow{S} = \frac{-i}{\sqrt{2}} \begin{bmatrix} 0 & 1 & 0 & -1 \\ 1 & 0 & 1 & 0 \\ 0 & 1 & 0 & 1 \\ -1 & 0 & 1 & 0 \end{bmatrix}. \tag{2.33}$$

For an arbitrary θ the S-parameters are functions of frequency as shown in figures 2.11 and 2.12.

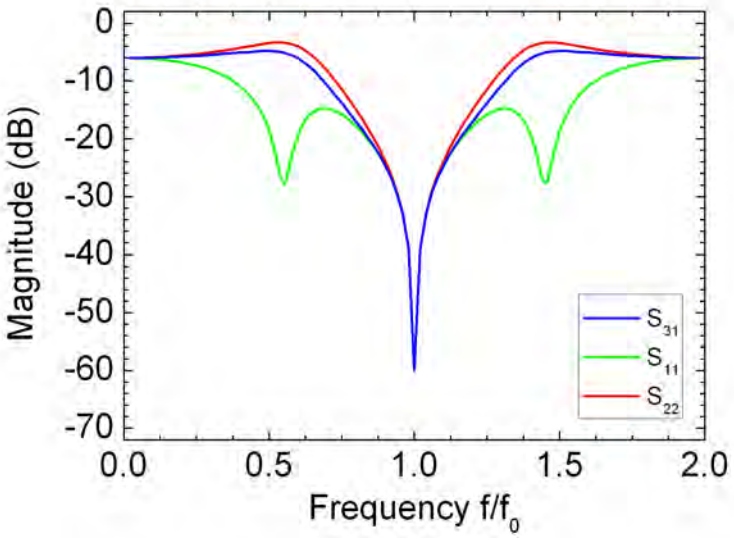

Figure 2.11: The S-parameters S_{11}, S_{22} and S_{31} of a 180° hybrid ring in dB as a function of frequency.

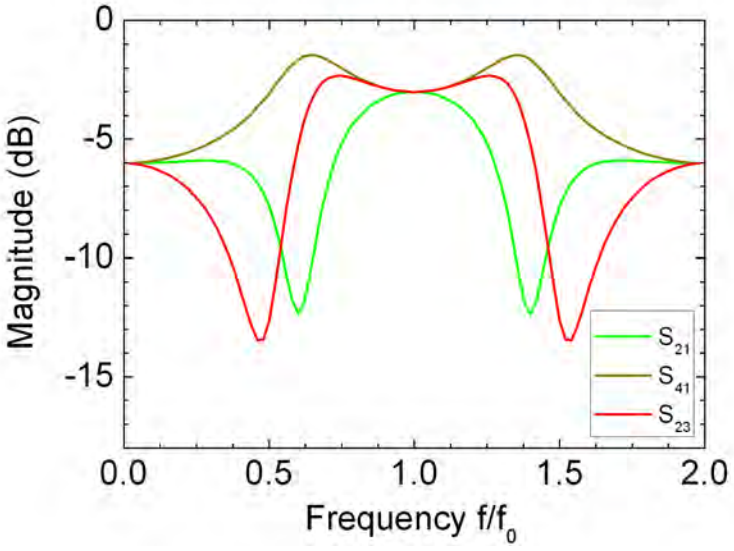

Figure 2.12: S_{21}, S_{41} and S_{32} of a 180° hybrid ring in dB as a function of frequency.

2.4 Design of the Microstrip Hybrid Ring

A. Emmert [24] covered CPW hybrid rings within his diploma thesis. These hybrid rings did not behave as expected leading to the conclusion of designing MS hybrids. The theory predicts the properties of the microwave being depending on the substrate. Therefore MS hybrid rings on two different substrates with two different loss tangents were fabricated and analyzed. The loss tangent of silicon is around 10 times the loss tangent of sapphire.
The designs of the MS hybrid rings must be adapted to the different substrates with respect to the different permittivities ε_r of silicon and sapphire. The parameters of the different MS hybrid rings are listed in table 2.4. The dimensions are explained in figure 2.13, where $R = (R_\mathrm{i} + R_\mathrm{a})/2$ and $w_\mathrm{r} = R_\mathrm{a} - R_\mathrm{i}$, h being the thickness of the substrate and t_s the thickness of the microstrip line.

name	MSH Nb Al_2O_3	MSH Nb Si	MSH Nb Si 500 nm	MSH Nb Si 1 μm	MSH Au	MSH Cu
substrate	Al_2O_3	Si	Si	Si	Si	PTFE/ceramic
conducter	Nb	Nb	Nb	Nb	Au	Cu
ε_r	10.6	11.9	11.9	11.9	11.9	10.2
$R\,[\mu\mathrm{m}]$	4780	4780	4780	4780	4780	4780
$w_\mathrm{a}\,[\mu\mathrm{m}]$	490	420	420	420	420	490
$w_\mathrm{r}\,[\mu\mathrm{m}]$	211	171	171	171	171	211
$h\,[\mu\mathrm{m}]$	500	525	525	525	525	590
$t_\mathrm{s}\,[\mathrm{nm}]$	200	200	500	1000	200	17500
$Z_\mathrm{a}\,[\Omega]$	47.5	49.5	49.5	49.5	49.5	52.9

Table 2.4: Parameters of the MS hybrids

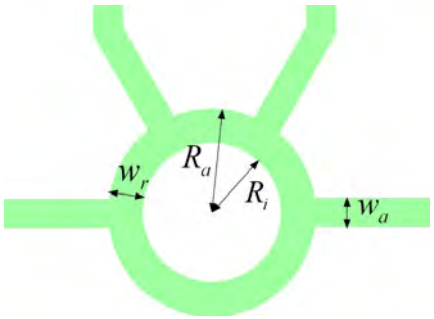

Figure 2.13: Design of a MS hybrid ring

Concerning these parameters, there are some details to consider:

- The dimensions of the MS hybrids have been designed using the formulas in section 2.2.2.

- The phase velocity, which leads to the diameter of the ring, can be calculated with (2.24).
- The desired frequency f_0 is 6 GHz, which leads to a mean radius of 4780 μm. This frequency is limited by the dimension of the substrate which is 20.4 mm $\times$ 15.0 mm and the space the arms of the hybrid rings need. To reach smaller frequencies, larger substrates are necessary.
- As mentioned in section 2.3.1, the lines of the hybrid ring are chosen to result in $Z_a = 50\,\Omega$. This matching was calculated with the formulas (2.25) and (2.26).

2.5 Design of the Coplanar Waveguide Hybrid Ring

The transmission spectra of the CPW hybrid rings produced and measured in reference [24] showed additional peaks. To investigate these peaks, three other CPW hybrid rings were designed lacking the inner ground plane (see figure 2.14).
The design of the CPW hybrid had to meet the same criteria as the MS hybrid ring. Table 2.5 shows the parameters of the different hybrid rings measured within this work[1]. Figure 2.14 explains the used parameters, h being the thickness of the substrate and t the thickness of the centerstrip.

name	CPW 1	CPW 2	H 3 AE	H 3 EH
substrate	Si	Si	Al_2O_3	Si
ε_r	11.9	11.9	10.6	11.9
R [mm]	4.2	4.2	3.825	3.825
w_r [μm]	400	220	90	90
w_a [μm]	600	600	200	200
g_r [μm]	270	400	177	177
g_a [μm]	290	290	125	125
h [μm]	525	525	500	525
t [nm]	200	200	100	200
Z_a [Ω]	50.9	50.9	52.5	52.2

Table 2.5: Parameters of the CPW hybrids

The main difference between H 3 AE and H 3 EH, CPW 1 and CPW 2 is the area of the ground plane. While H 3 has ring shaped ground planes inside and outside the ring, the inner ground plane is missing on H 3 EH. The ground planes of the CPW 1 and CPW 2 are spread over the whole substrate outside the ring and are missing inside the ring (see figure 2.14). The inner ground plane of H 3 AE had to be connected with the outer ones via bonding wires. These bonding wires include

[1] The H 3 hybrid ring on Al_2O_3 was designed and measured by A. Emmert within his diploma thesis: A. Emmert, Circuit-Quantum Electrodynamics with Superconducting Flux Qubits, 2006

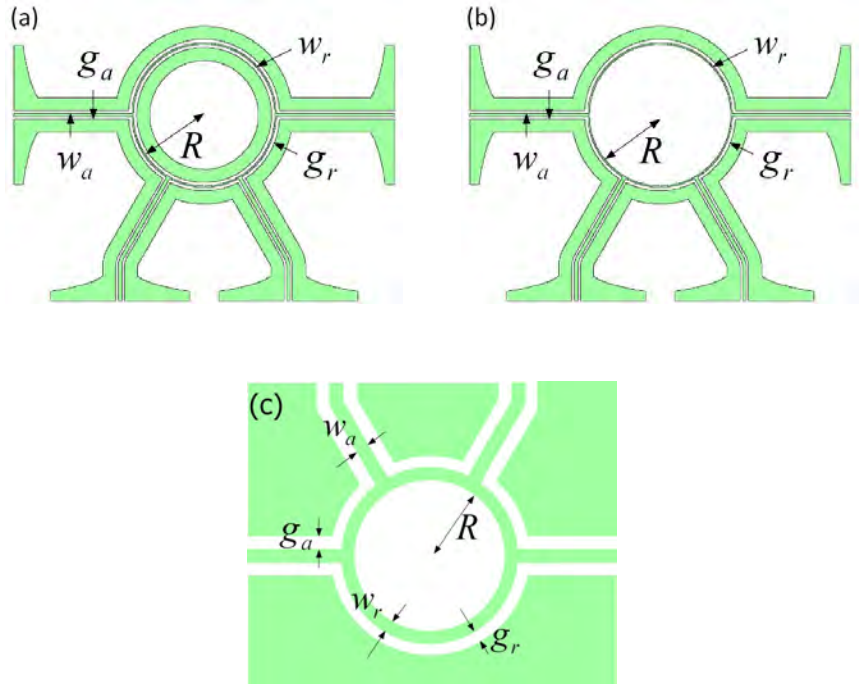

Figure 2.14: Layout of (a) the H 3 AE CPW hybrid ring, (b) the H 3 EH hybrid ring. The difference is the missing inner ground plane. (c) Shows a schematic layout of the CPW 1 and CPW 2 hybrid rings

reactive capacitances and inductances that influence the performance of the hybrid ring. To analyze this influence, H 3 EH was designed without the inner ground plane. Since the width of the lines and the gaps remained unchanged, the matching $Z_\mathrm{a} = \sqrt{2}Z_\mathrm{r}$ was not valid anymore. To ensure this matching, CPW 1 was designed by using formulas for asymmetrical ground planes so that the inner ground plane could be eliminated without influencing the impedances. The design of CPW 2 was copied from reference [42].

3 Sample Fabrication and Experimental Setup

The microstrip (MS) and coplanar waveguide (CPW) hybrid rings were fabricated using optical lithography. The process parameters were adapted to the different materials. This section gives an overview of the lithography process whereas details of the steps can be found in appendix E. Section

3.1 Sample Fabrication

The samples were fabricated on silicon substrates (15.0 mm × 20.4 mm × 525 μm) with an oxide layer (50 nm) or on sapphire substrates (15.0 mm × 20.4 mm × 500 μm). The copper hybrid ring was produced on RO3010 dielectric from Rogers Corporation[1] (15 mm ×20 mm × 590 μm) which was coated with a 17.5 μm thick copper layer on each side.
The fabrication processes for niobium or gold on silicon or on sapphire are similar while the production of the MSH Cu sample differs strongly. An overview of the different production steps is given in this chapter while the process parameters and details of the fabrication can be found in appendix E.
After an initial cleaning of the substrate, the conducting material was sputtered onto the polished side of the sample. Niobium was sputtered directly onto the substrate. To achieve a better adhesion of gold on the substrate, a thin layer (3 nm) of chromium was sputtered first. Then, the 200 nm thick gold layer was applied in situ.

Optical Lithography

After cleaning, the AZ© 5214E image reversal photoresist was spin coated with 8000 rpm to a thickness of less than 1.14 μm and baked (soft bake) at 110° C for 70 s. The high rotation speed was chosen to minimize the so-called *edge wall* (see figure 3.1). This edge wall prevents a good contact of the mask with the structures and the photoresist, which reduces the resolution of the pattern. To remove the edge wall, the sample was exposed for a comparably long time (15 s) with a special pattern (see figure 3.2(a)). The long exposure time was necessary in order to make sure that the edge wall would be completely removed. The edge wall was eliminated after one minute of developing (see figure 3.2(b)). A crucial step was the cleaning of the sample. The sample was first cleaned in a glass with water and dried with nitrogen

[1] Rogers Corporation: http://www.rogerscorporation.com/ (2007)

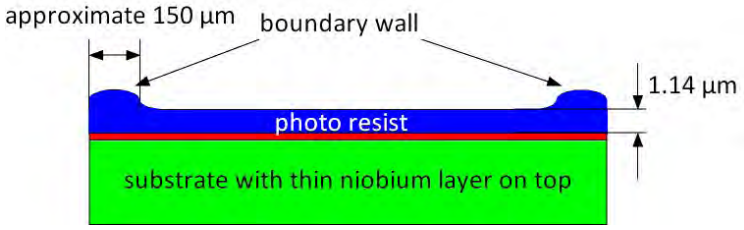

Figure 3.1: Cross section of the substrate with photoresist

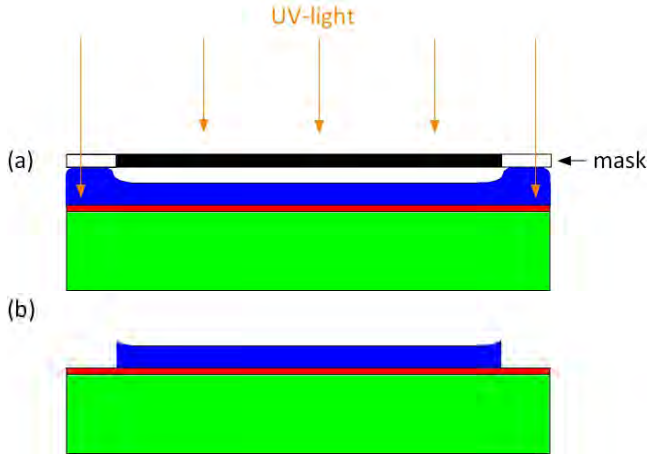

Figure 3.2: (a) Substrate with edge wall and mask. The gap between the photoresist and the structure on mask in the middle of the sample leads to a declining focus of the structure on the sample. The removing of the edge wall results in a smoother photoresist (b).

gas. Any remaining water drops would influence the exposure with the hybrid ring structure.
The optimum exposure and development parameters were found in a dose series. The optimal exposure time is 4 s and development time 2 min.
The exposure and development times of the copper sample were chosen to be 19 s and one minute. The size of the manual cut sample did not allow an additional edge wall removing. Thus, the comparably long exposure and development times were necessary to remove the photoresist with the edge wall at once.

Etching

During the etching process, the excessive conductor, uncovered with photoresist, was removed.
Niobium was etched in a $SF_6 - Ar$ atmosphere which was done in a Plasmalab 80 Plus of Oxford Instruments Incorporated. Therefore, the substrate was placed inside a reactor in which $SF_6 - Ar$ was kindled. A plasma was placed in the gas mixture using

a RF power source, splitting the gas molecules into ions. The ions were accelerated by the RF power and SF_6 could react with the niobium. To achieve better etching results, the RF power was high enough to accelerate the ions to a critical speed that allowed the ions to knock atoms out of the material. This way of etching is called physical reactive ion etching[2]. A test series of different etching durations showed the best results for a duration of 2:10 min for 200 nm niobium.
Gold was etched in an argon ion etching system but the process was similar to the etching of niobium. Here the reactive component was missing but a higher RF power forced the Ar-ions to knock out the gold atoms. The minimum removal time was six minutes, but to ensure good quality, the sample was etched for ten minutes.
The conditioning of copper differed completely from the other etching methods. Copper was not etched in a dry etching process like niobium and gold but in a KI-I_2 solution. Before etching the copper sample, it was necessary to protect its ground plane with resist. This process took around 6 min.
In a final step, the rest of the resist could be ashed with an oxygen plasma (ashing) and removed in hot acetone.

3.2 Sample Preparation

Figure 3.3 shows the box of oxygen free copper with a 3 μm thick gold coating that was used for the measurements. The structures were inserted in this box and connected with SMA connectors (32K724-600S3, panel jack) from Rosenberger Hochfrequenztechnik GmbH & Co. KG[3].

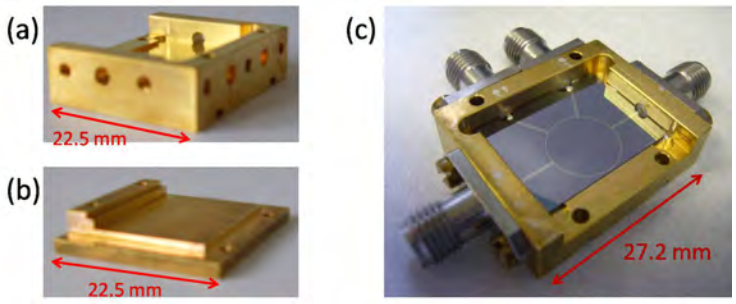

Figure 3.3: (a) Box and (b)top cover after their production; (c) Box with Rosenberger connectors and hybrid ring

There are three different methods that can be used to contact the structure with the SMA connectors including

- Silver glue:
  Silver glue is a paste consisting of silver powder, resin and solvent. A drop of

[2]In comparison with the physical etching, there is also the so-called chemical etching. This etching is performed with a lower RF power but with a higher ion density which leads to less power of the ions. Thus, the ions cannot knock out any niobium atoms.
[3]Rosenberger Hochfrequenztechnik GmbH & Co. KG, http://www.rosenberger.de/ (2007)

silver glue (Leitsilber 200) from Hans Wolbring GmbH[4] was trickled on top of the connector. The liquid silver glue spread out between the connector and the superconducting line as shown in figure 3.4(a). This way of contacting is very simple compared to the alternative methods. On the other hand, the silver glue is very fragile and the measured results are hard to reproduce in exactly the same way as some measurements like 4.10 and 4.13 will show.

- Bonding wires:
  The structure and the connectors were contacted with aluminum bonding wires (see figure 3.4(b)). The measurements (see figure 4.20) show that this way of contacting is less ideal than the use of silver glue because the wires provide a reactive inductance. Using contacts with bonding wires is better for reproduction than the silver glued or the soldered contacts.

- Soldering:
  Two samples were contacted by soldering - a niobium and a copper hybrid ring. Since niobium is hard to solder, an additional sample with a thin gold layer on the line at the contacts was fabricated. The solder was indium with 3 % silver. The copper sample could be connected with standard solder (tin (62 %), lead (36 %) and silver (2 %)). The procedure requires patience and a calm hand and is not very reproducible.

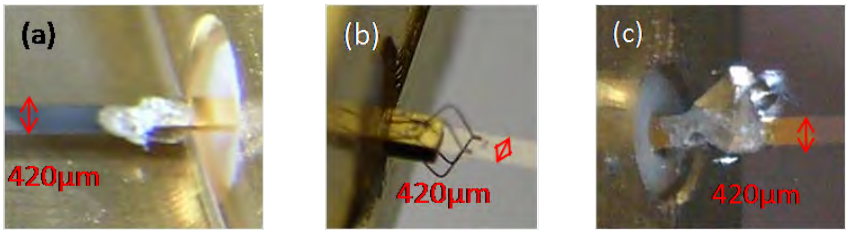

Figure 3.4: Contact with (a) silver glue (b) bonding wires (c) solder between connector with strip line

The ground plane of the CPW hybrid rings had to be connected with the box. This was done by smearing silver glue between the inner walls of the sample holder box and the ground planes of the CPW structures.
As mentioned before, the H3 structure was measured within another diploma thesis. The way of joining the line with the connectors and the ground plane with the box is described in reference [24]. The inner and outer ground planes were connected via bonded airbridges.

[4]Hans Wolbring GmbH, http://www.keramikbedarf.de/ (2007)

3.3 Experimental Setup

The box with the structures was placed inside a cryostat and connected via home made semi-rigid microwave coaxial cables to a HP8722D network vector analyzer (NVA). The measurement setup is shown schematically in figure 3.5. This setup allows measurements between room temperature and 1.5 K.

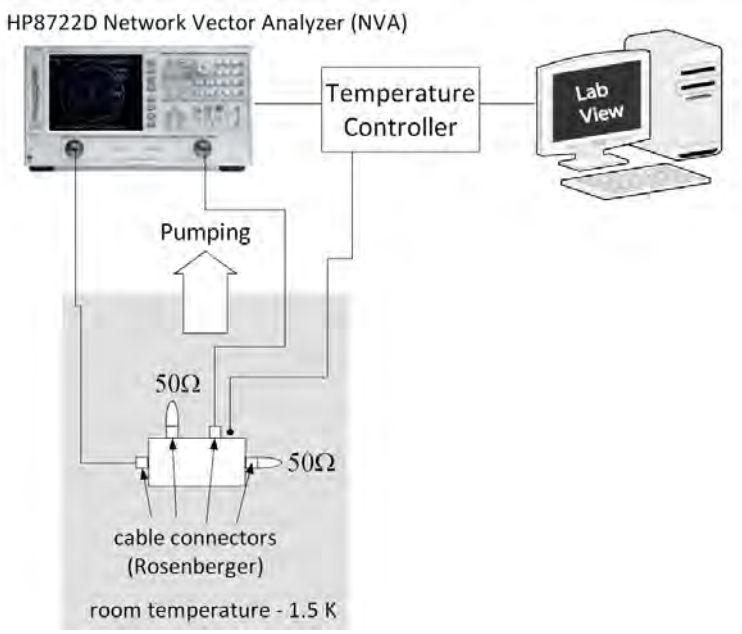

Figure 3.5: Measurement scheme: The S-parameters were measured using a HP8722D NVA which was controlled and readout by a LabView programm. The temperature was recorded by using a NEOCERA LTC-21 temperature controller and a silicon diode. The silicon diode was close to the box with the sample.

The 50 Ω terminations from Huber & Suhner guaranteed a well defined signal at the output port as mentioned in section 2.3.1.
The cables inside the cryostat were fabricated at the WMI. At the end of each cable (semi-rigid: UT-085-SS-SS from MICRO-COAX©[5]) the SMA male RF coaxial cable connectors (SMA-50-2-15 from Huber & Suhner) were soldered before the cables were bent (see figure 3.6) and inserted into the cryostat. The length of each cable is approximately 1 m. The attenuation is shown in figure 3.7 and is similar for all four cables. This measurement was performed with two different values for the input power to analyze the power dependence of the attenuation. It shows that the difference of the two measurements is small. By using power dependent calibration data, this influence can be reduced. Measurements of hybrid rings at different values of the input power will later show the influence of the power being negligible at low temperatures.

[5]MICRO-COAX©, http://www.micro-coax.com

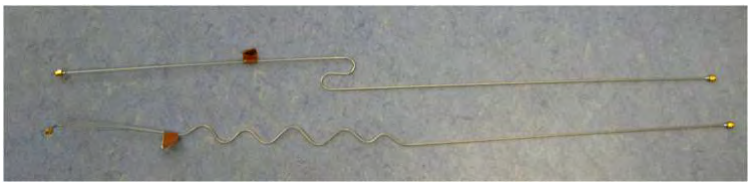

Figure 3.6: Two of the four used semi rigid coaxial cables. The length of each cable is approximate 1 m.

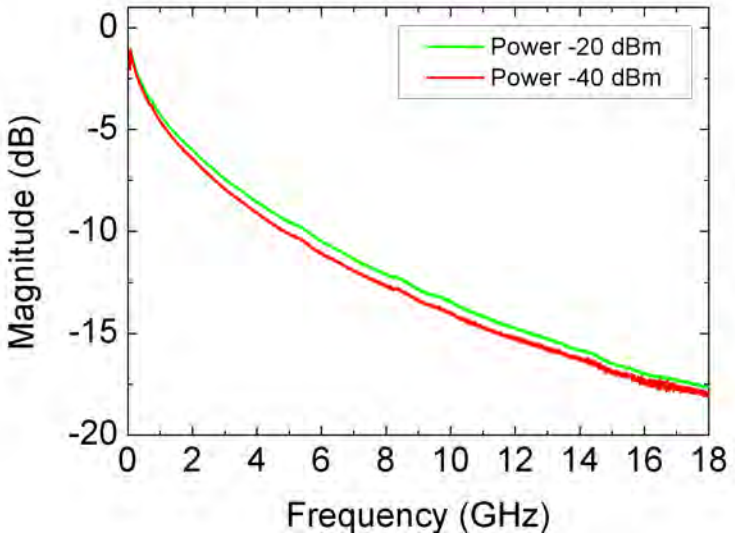

Figure 3.7: Power and frequency dependent attenuation of the semi-rigid coax cables that are used inside the cryostat. The data was averaged of 50 traces at the -40 dBm measurement and of 20 traces at the -20 dBm measurement.

A short description of the NVA is given in reference [21] and a more detailed description can be found in references [43] and [44]. The NVA records a maximum of 1601 different frequency values during one frequency sweep. The frequency range for the measurements in this thesis was chosen to be from 50 MHz to 18 GHz.

Before measuring the S-parameters it is necessary to perform a response calibration. For this purpose, two of the cables were connected with SMA female-female adapter from Huber & Suhner[6] inside the cryostat and the transmission data was measured at room temperature and at 4.2 K. The difference between the measurements at 4.2 K and 1.5 K is negligible. This was done for each possible combination of the four cables inside the cryostat. The calibration data was saved and subtracted from the measurement data. In the end the information contained by the data excluded every information about the cables and the NVA. The subtraction was applicable

[6]Huber & Suhner, http://www.hubersuhner.de

because the data was measured in a logarithmic scala.
The temperature dependency of the calibration data can be seen in figure 3.8. The detected signals show the behavior of the NVA and the cables in a frequency range from 50 MHz to 18 GHz. The explanation for the temperature and frequency dependency on the calibration data is linked to the attenuation and the noise in the cables. At low temperatures the attenuation is lower than at higher temperatures. The attenuation is lower for low frequencies than for high frequencies as well. This can be explained by the drude model (see [45]) where conductively depends on frequency.

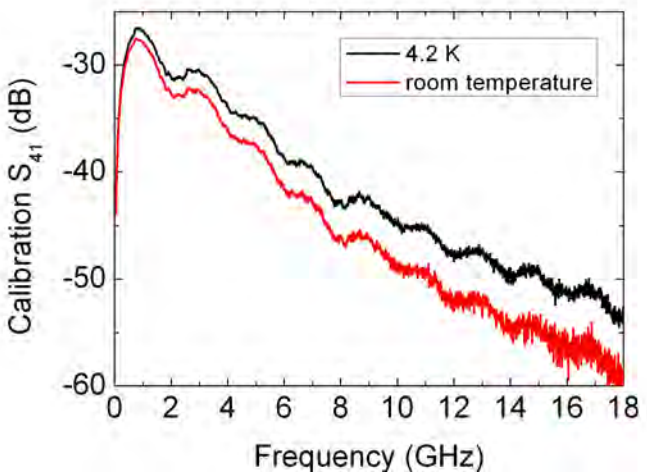

Figure 3.8: The calibration data for S_{41} at room temperature and 4.2 K. This calibration data was subtracted from the measurement data to exclude the behavior of the cables and the NVA.

The adapters have a different electrical length than the box holding the sample. The difference of the electrical length results in a difference of the reflection ratio between the adapter and the box with the sample, hence there is a small systematic error in the response calibration. This one can not be corrected. It only influences phase measurements which were not performed within this work. In the end this error did not influence the accuracy of the measurements.
The error due to the attenuation of the adapter is small and was neglected (the attenuation of the used Rosenberger connectors compensate it quite well).

4 Measurements of the Hybrid Rings

This chapter shows the results of measurements of the S-parameters of the fabricated hybrid rings. The MS hybrid rings were analyzed due to different line thicknesses of the center strip, superconducting and non-superconducting ground planes and different kinds of contacts between center strip and Rosenberger connectors and different conducting materials. The different materials of the hybrid ring allow to investigate the influence of fluxoid quantization on the hybrid ring. Asymmetrical CPW hybrid rings were measured to be compared to symmetrical CPW hybrid rings from a former work.
For a correct interpretation of the measured results of the different hybrid rings, it is useful to give some information about the different measurement parameters and techniques:

Termination

The hybrid ring is a four port device and characterized by the transmission of an applied signal at one port to the other ports. This transmission is measurable by applying a signal at one port, measuring the output at a second port and terminating the last two ports.
In general, there are two different ways to terminate the ports that are not measured - in and outside of the cryostat (see figure 4.1). These $50\,\Omega$ terminations absorb the microwave signal coming out of the ports that are not measured, e. g. when measuring S_{31}, ports two and four are terminated. Thus, ideally no reflections at these ports could influence the S_{31}-parameter. Any reflections that occur at these ports are due to the quality of the connection between the center strip line and the Rosenberger connector.
The comparison of a measured S_{31}-parameters with different termination methods is shown in figure 4.2. The measured hybrid ring was MSH Nb Al_2O_3 with silver glue as ground plane and silver glue for the contacts between the connectors and the line. Both S_{31}-spectra were recorded at 4.2 K with an input power of -40 dBm and 50 traces have been averaged in both measurements. This data does not agree with theory (see figure 2.11) because of a "hump" and a resulting frequency shift, which will be analyzed later.
The termination outside the cryostat has the great advantage of measuring all S-parameters during one cool down whereas the termination inside the cryostat is less noisy. The high noise level for the "outside" measurement is associated with two extra reflections at the ports of the cryostat that were not considered when taking the calibration data. The calibration data was taken for two cables but the

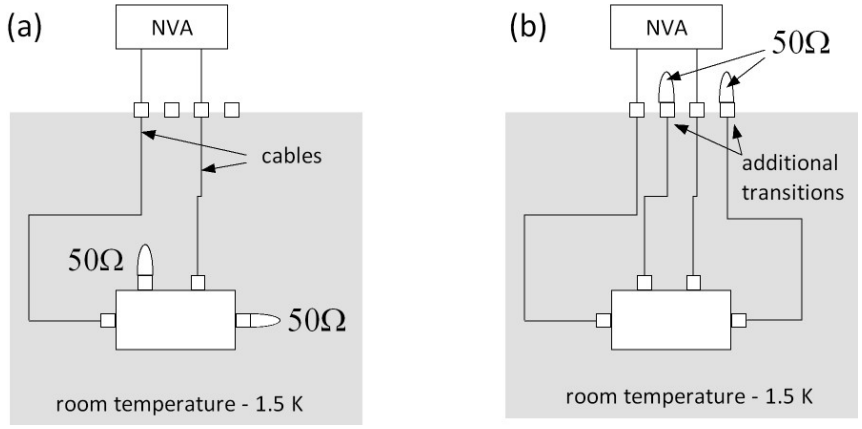

Figure 4.1: (a) termination inside the cryostat; (b) termination outside the cryostat

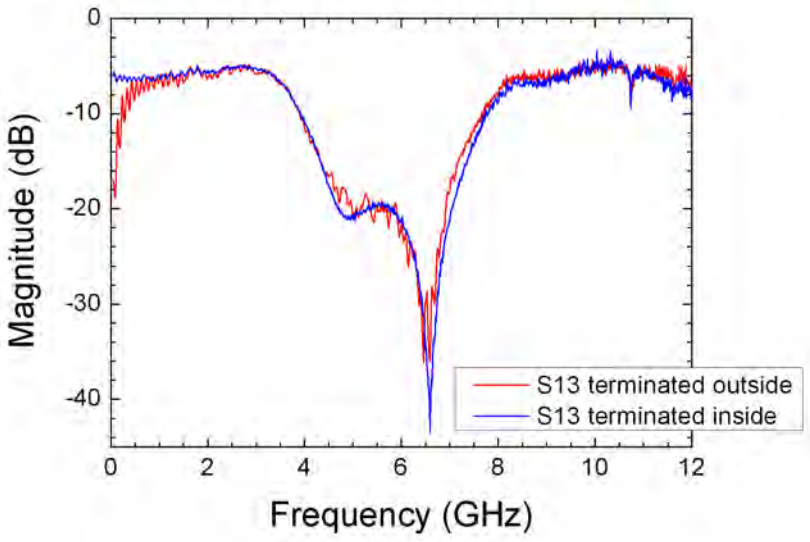

Figure 4.2: Comparison of two different ways of termination

measurement involved four cables. Thus, the reflections of two additional transitions between the two cables and the 50 Ω resistances, as shown in figure 4.1, were not taken into account in the calibration.
For a quick estimate of the performance of the hybrid ring the "outside" measurements was used, whereas for a more detailed look at the transmission spectra the "inside" measurement is preferred. According to figure 4.2 the magnitude of the isolation of the "outside" measurement is -36 dB while the one of the "inside" measurement technique shows a result of -44 dB.

Power

The measurements of the S-parameters were performed at two different power levels: -40 dBm and -20 dBm. As one can see in figure 4.3, the main difference between these two power values is the noise level. For this graph the MSH Cu sample was measured with the 50 Ω terminations inside the cryostat as shown in figure 4.1(a)

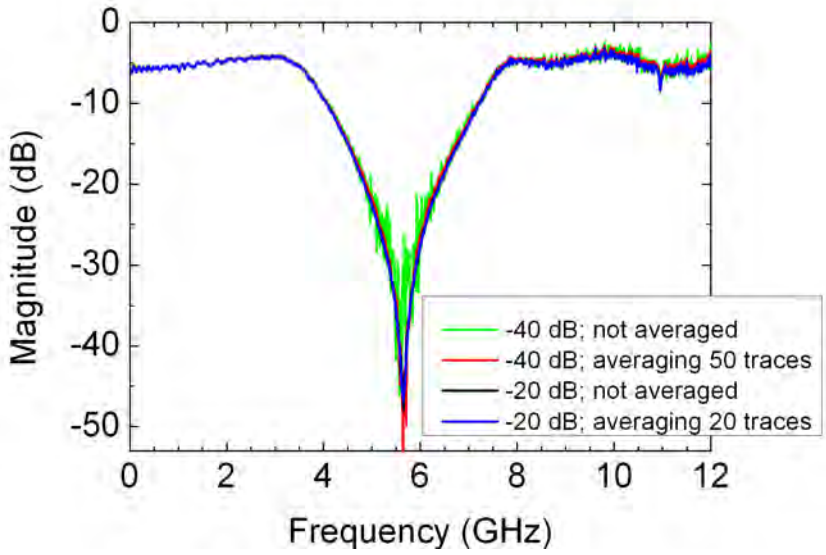

Figure 4.3: Comparison of two input power values: -40 dBm and -20 dBm at 4.2 K (S_{31} of MSH Cu with silver glue for contacting the line with the connectors)

The graph taken with an input power of -40 dBm is very noisy compared to the graph with input power -20 dBm. The advantage of averaging over 50 traces can be seen by comparing the two -40 dBm graphs in figure 4.3. In contrast, the measurements with an input power of -20 dBm show a good agreement between the averaged data and the non averaged data. This in consistent with an increasing signal to noise ratio for higher input powers.
Comparing the averaged data taken at -40 dBm input and the data taken at -20 dBm input leads to the conclusion that the performance of the hybrid ring is independent of the input power in the range of -20 dBm to -40 dBm.

Resonance

Every measurement, except the CPW H 3 sample, shows a resonance at around 11 GHz. This resonance can be identified with a standing wave in the measurement box in liquid helium. The dielectric constant of liquid helium is 1.05 which leads to a phase velocity $v_\mathrm{p} = 2.92 \times 10^8$ m/s. The volume of the box filled with liquid helium is 20.6 mm × 15.2 mm × 2.8 mm which corresponds to a volume diagonal of 25.8 mm. With $f = v_\mathrm{p}/\lambda$ one gets the resonance frequency 11.3 GHz which fits quite well to

the observed 11 GHz. As the derivation shows the resonance frequency depends on the volume diagonal. The inner dimensions of the box are 0.2 mm larger than the sample dimensions. According to the exact position of the sample in the box, the volume diagonal and thus, the resonance frequency can shift about a few MHz (see figure 4.4).

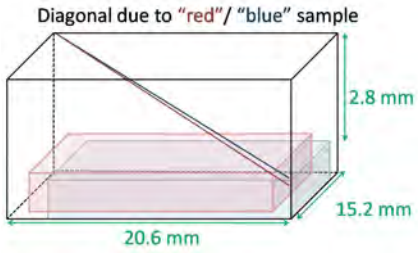

Figure 4.4: Sketch of the sample in the box. The length of the volume diagonal depends on the exact position of the sample in the box.

Figure 4.6 shows a frequency shift of the box resonance between 2.4 K and 31 K. This frequency shift is due to the change of the dielectric constant at the phase transition of helium.
The CPW H 3 sample was measured in another box. This box has inner dimensions of 20.5 mm × 16.0 mm × 5.0 mm which also leads to a resonance frequency of around 11 GHz. Because the spectrum of the H 3 sample shows some irregular peaks, the peak due to the box resonance cannot be identified. More details about this box can be found in reference [24].

Temperature Dependence

The different materials, niobium, gold and copper, show different temperature dependencies of the isolation spectrum. As shown in figure 3.8 the attenuation of the cables decreases with decreasing temperature. Figures 4.5, 4.6 and 4.7 present the temperature dependencies of the S_{31}-parameters of niobium, gold and copper.
All measurements were performed with an input power of -20 dBm and a termination inside the cryostat.
The spectra of the MSH Nb Si sample shown in figure 4.5 show a characteristic change of the S-parameter between 9 K and 10 K. This is linked to the critical temperature T_c which is 9.25 K for niobium. At this temperature the niobium changes from a superconductor to a normal conductor with a finite resistivity.
For temperatures between 30 K and 40 K, the isolation dip broadens until the S_{31}-parameter is not visible anymore. This effect can also be seen in the MSH Au measurement as shown in figure 4.6. The smearing is due to the thickness of the conductor which is 200 nm for both niobium and gold on silicon. The copper on PTFE/ceramic is 17 μm thick and therefore the isolation dip is still visible at room temperature.

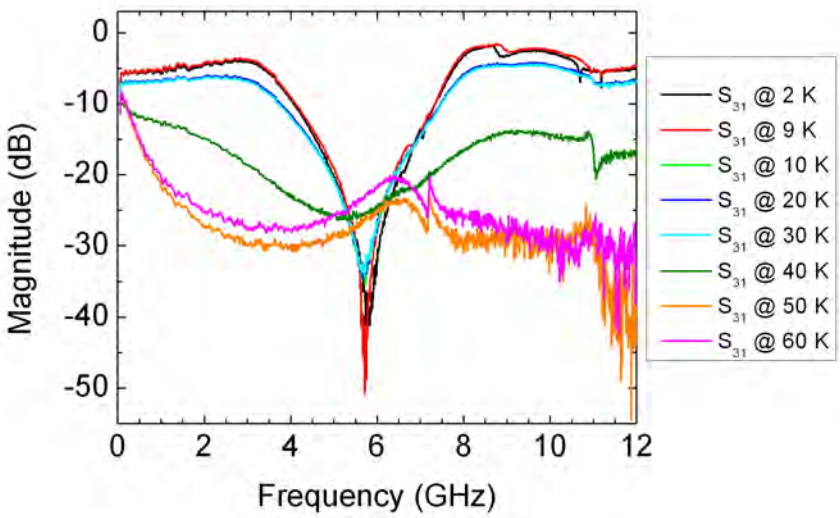

Figure 4.5: Temperature dependence of MSH Nb Si (input power -20 dBm, termination inside the cryostat, not averaged). A clear change of the isolation spectrum between 9 K and 10 K is due to the transition from the superconducting to the normal conducting state.

MSH Cu shows a shift of the isolation dip to higher frequencies with increasing temperature (see figure 4.7). This feature could not be observed with the other samples because the shift is identifiable only for temperatures above 100 K. The frequency shifts is due to the temperature dependence of the resistivity of copper. It increases with temperature which leads to a change of the phase velocity. This results in a shifted center frequency.

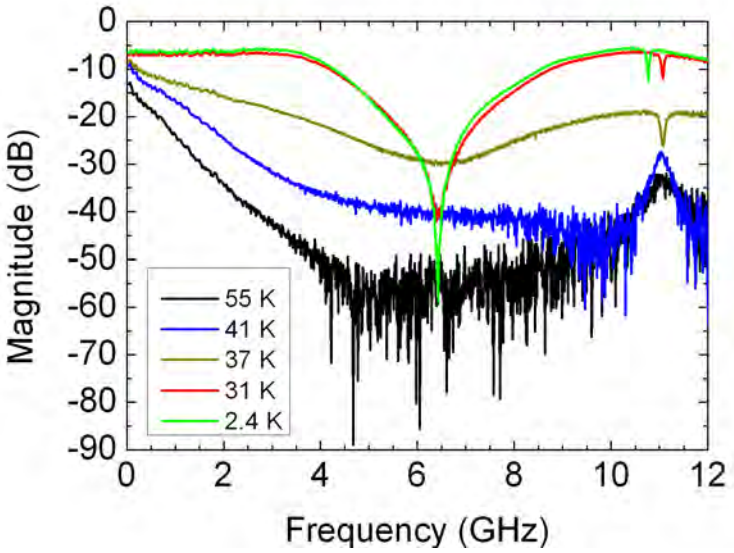

Figure 4.6: Temperature dependence of MSH Au (input power -20 dBm, termination inside the cryostat, not averaged)

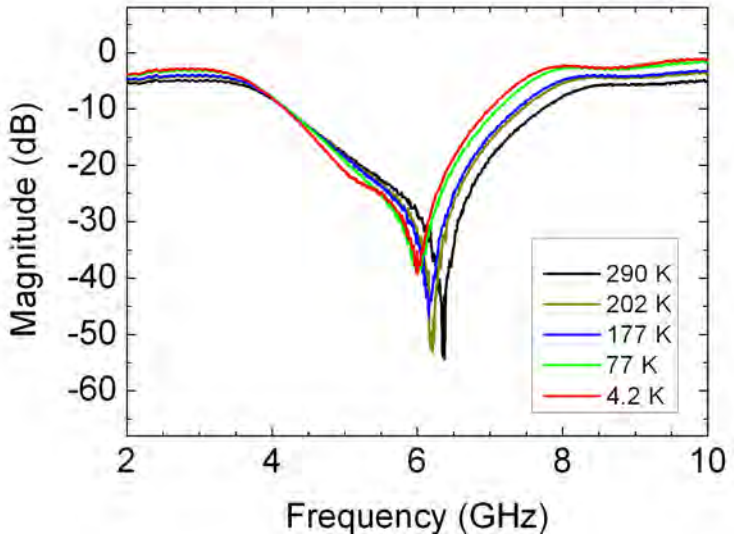

Figure 4.7: Temperature dependence of the isolation spectrum of MSH Cu (input power -20 dBm, termination inside the cryostat, not averaged). The shift of the isolation frequency with increasing temperature is due to the temperature dependence of the resistivity.

4.1 Microstrip Hybrid Ring

The following section shows the results of the fabricated and measured MS hybrid rings. All measurements were performed at 4.2 K.

4.1.1 Niobium on Sapphire and Silicon

Two MSH designs were developed to optimize the characteristic impedance with respect to the different permittivities of silicon and sapphire (see figure 4.8). Since

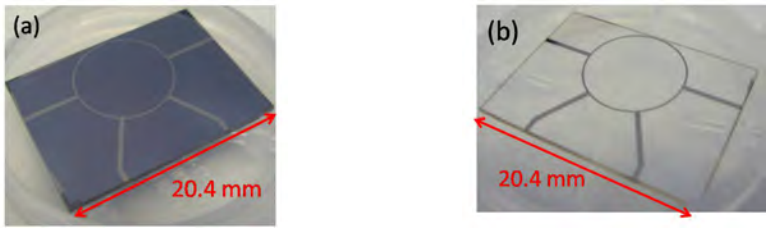

Figure 4.8: Picture of (a) MSH Nb Si; (b) MSH Nb Al_2O_3

the dielectric losses in sapphire are smaller than in silicon due to the lower loss tangent, the MSH Al_2O_3 sample was expected to show better results. Figures 4.9 and 4.10 show the measured data for MSH Nb Si and MSH Nb Al_2O_3.
Both measurements were performed at 4.2 K. A drop of silver glue holds the sample in the box. Silver glue was also used to connect the conductive lines to the connectors. The noise level in the graphs in figures 4.9 and 4.10 is high because the data was not averaged, the terminations were outside the cryostat and the input power value was -40 dB.
Both measurements show similar results. Although being expected, the better isolation due to the smaller loss in sapphire could not be confirmed. The anisotropy of the loss tangent of sapphire might be a possible reason. According to reference [46] the loss tangent parallel to the crystal axis of sapphire is around one magnitude smaller than the loss tangent perpendicular to the crystal axis. Reference [47] and [48] predict the *averaged* loss tangent of sapphire being ten times smaller than the one of silicon at room temperature. Values valid for low temperatures could not be found. Since the hybrid ring is a circular device one has to consider all directions of the (two-dimensional) substrate and not only in the preferred direction.
The measurements in figures 4.9 and 4.10 agree very well with the theory. The isolation dips reach a magnitude of around -40 dB. Since the terminations are outside the cryostat, the magnitudes are expect to be around 10 dB smaller than these measurements show. The coupling parameters of the silicon sample in figure 4.9 reach a magnitude of -3 dB at the center frequency 6 GHz up to 0.5 dB. The coupling parameters of the sapphire sample in figure 4.10 are in better agreement with theory than the coupling parameters of MSH Nb Si.

These hybrid rings meet the conditions the microwave beam splitter has to fulfill and can therefore be used for the homodyne detection of weak microwave signals.

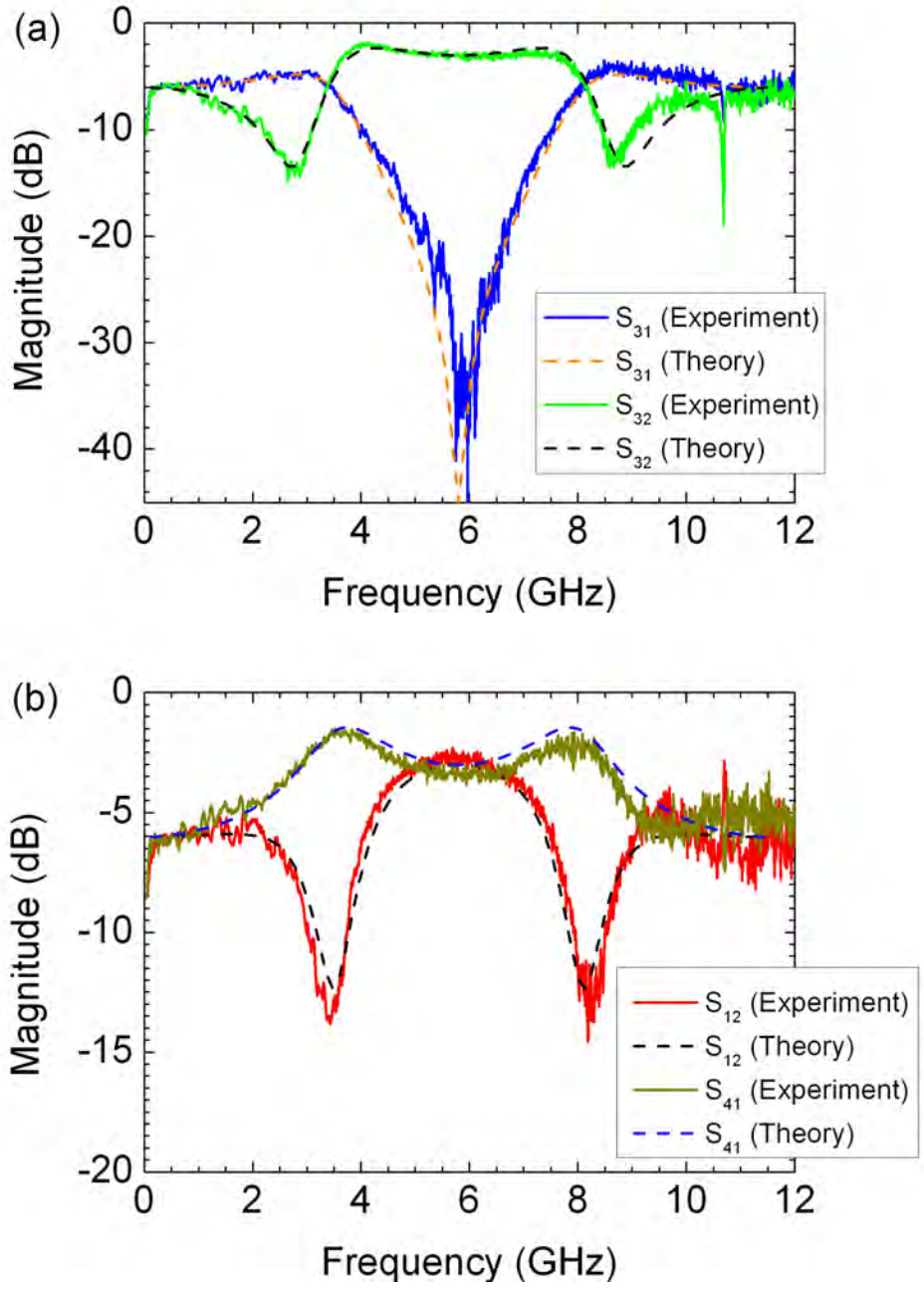

Figure 4.9: Measurements of MSH Nb Si at 4.2 K (not averaged, input power -40 dBm, termination outside the cryostat)

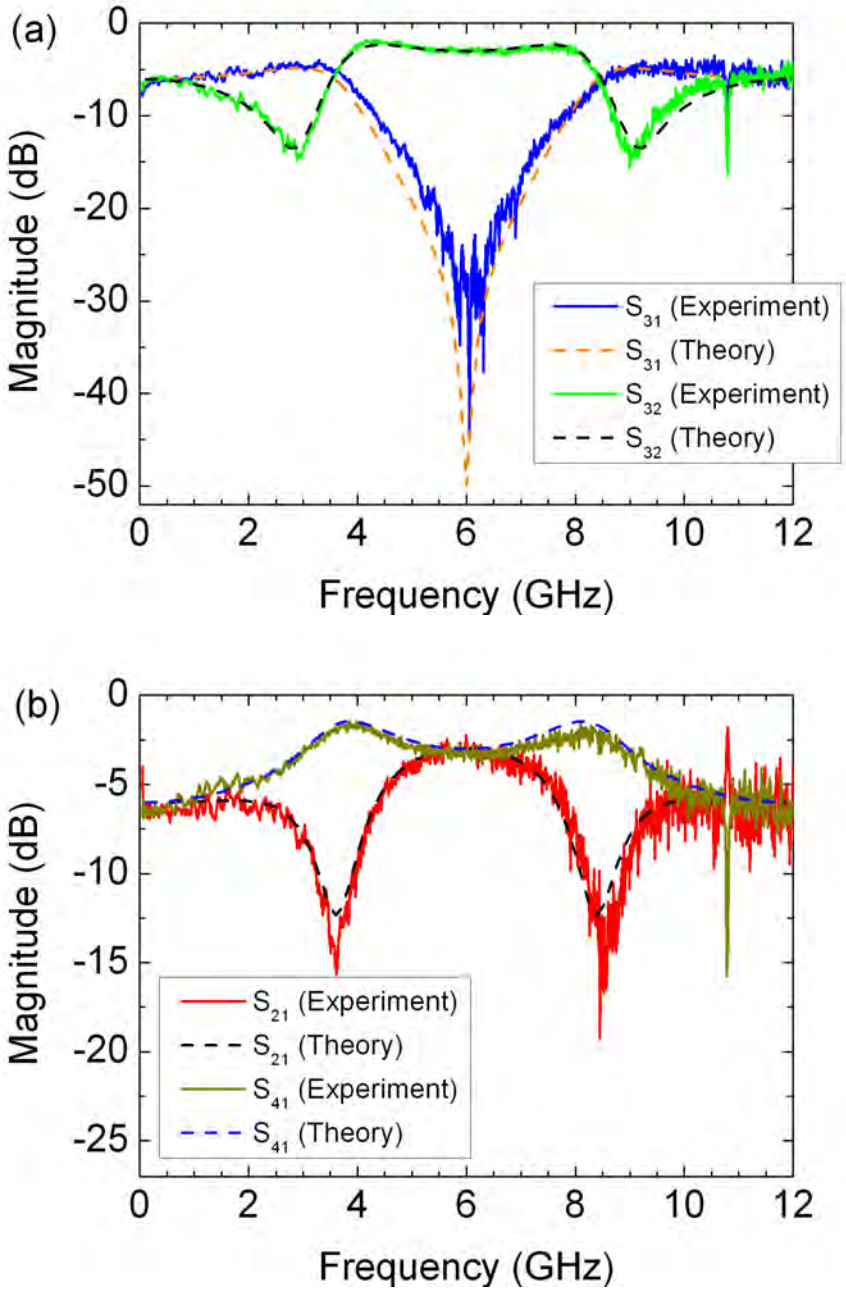

Figure 4.10: Measurements of MSH Nb Al_2O_3 at 4.2 K (not averaged, input power -40 dBm, termination outside the cryostat)

4.1.2 Gold on Silicon

The gold hybrid ring on silicon (MSH Au) was fabricated to investigate the influence of the fluxoid quantization on the hybrid ring.
The measured S-parameters of the MSH Au sample are shown in figure 4.11.
Measurements of the S_{31}-parameter and S_{32}-parameter agree very well with theory while the other spectra differ from the theoretical calculations. A possible explanation is to assume a mismatch between the characteristic impedances of the ring and the arms of the hybrid ring. The measured 4 dB coupling leads to a matching of $Z_\mathrm{r} = 2.2 Z_\mathrm{a}$ instead of $Z_\mathrm{r} = \sqrt{2} Z_\mathrm{a}$. This mismatch of the lines would result in a difference of the line widths of around 100 μm which cannot be caused by the fabrication process.
The isolation of the measurement in figure 4.11(a) with a magnitude of -66 dB has been the best detected isolation so far.
In comparison to the measurements on the niobium hybrid ring, the center frequency for MSH Au is around 6.4 GHz. The reason for this frequency shift is another phase velocity of the microwave due to the different conducting material.

4.1.3 Copper on Teflon/Ceramic

For technical reasons, the gold sample could not be fabricated with a larger film thickness at the WMI. MSH Cu has a line thickness of 17.5 μm.
Figure 4.12 shows the results of the MSH Cu sample. The data was taken with an input power of -40 dBm and was averaged over 50 traces. The 50 Ω-terminations were fixed inside the cryostat. This data is in accordance with theory.
The isolation and coupling parameters meet the theory for a center frequency of 5.7 GHz. Since the design was calculated to fabricate the hybrid ring of niobium on silicon and not copper on teflon/ceramic, the frequency shift was expected.
In contrast to MSH Au, the coupling parameters of the copper hybrid ring are -3 dB at the center frequency. The isolation with a magnitude of -50 dB is similar to the isolation of the niobium samples when keeping in mind that the niobium samples were measured with the terminations outside the cryostat.

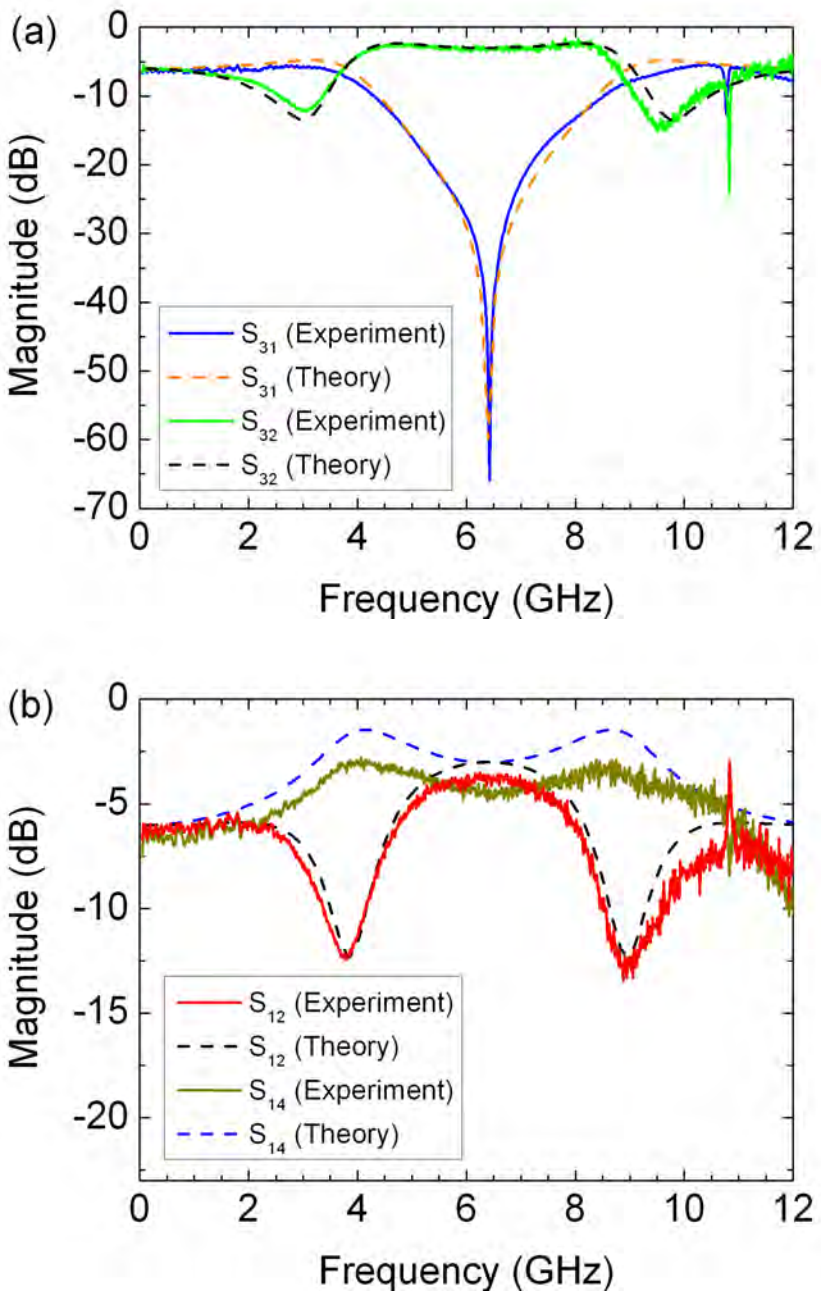

Figure 4.11: Measurements of MSH Au at 4.2 K: S_{41}, S_{32}, S_{21} (50 traces averaged, input power -40 dBm, termination inside the cryostat) and S_{31} (30 traces averaged, input power -20 dBm, termination inside the cryostat). The isolation in (a) has been the best detected isolation so far.

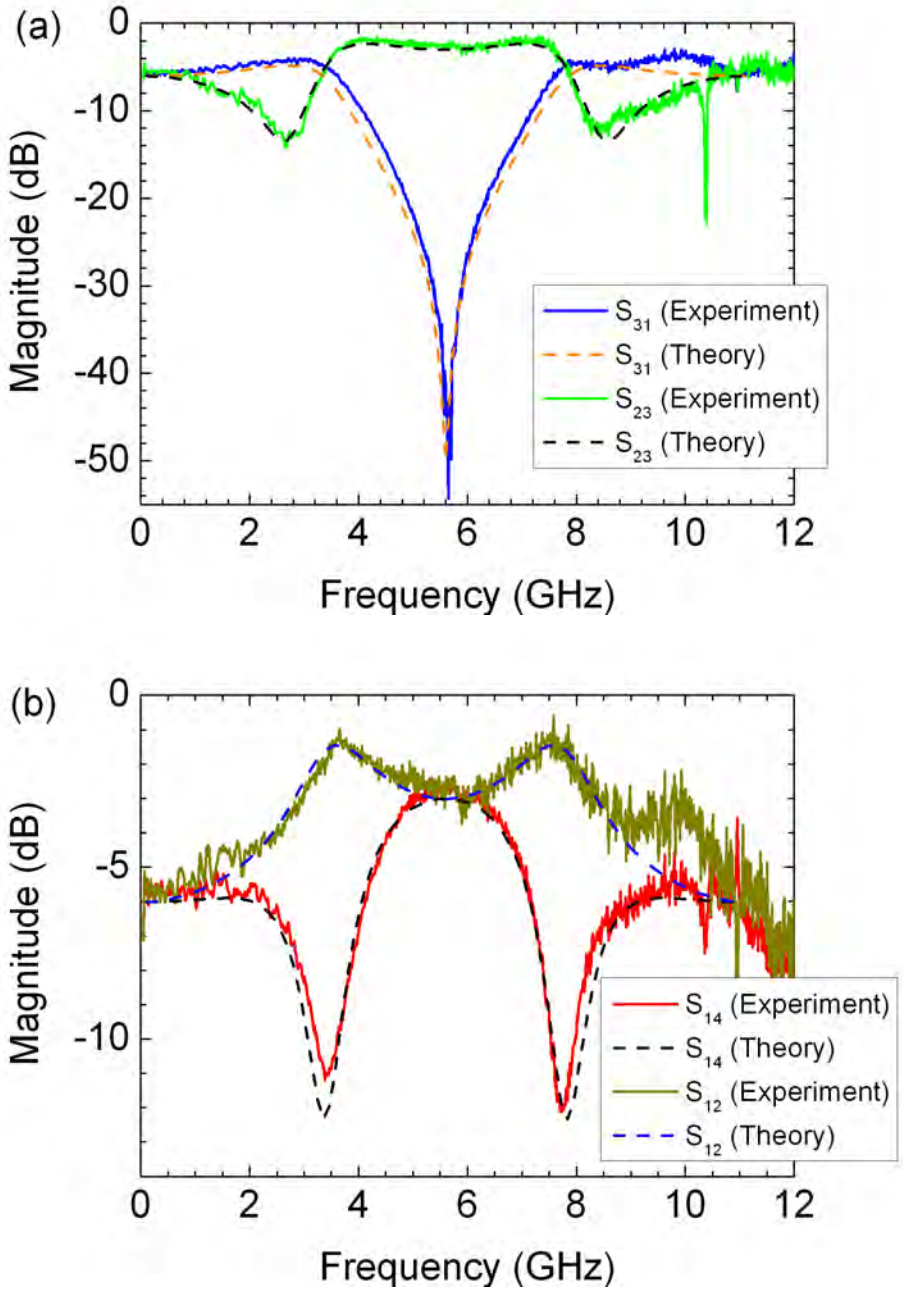

Figure 4.12: Measurements of MSH Cu at 4.2 K (50 traces averaged, input power -40 dBm, termination inside the cryostat)

4.1.4 Reproducibility

The measurements of the niobium hybrid rings on silicon and sapphire have been repeated after dismounting and reinstalling the samples into the box. This time port two and port four were terminated *inside* the cryostat. The value of the input power value remained at -40 dBm and the traces were averaged 50 times. The S_{31}-measurements of MSH Nb Al_2O_3 exhibit a clear hump close to the center frequency with a resulting frequency shift of the isolation dip (see figure 4.13). In the measurement of the silicon sample, the hump is smaller but still visible.

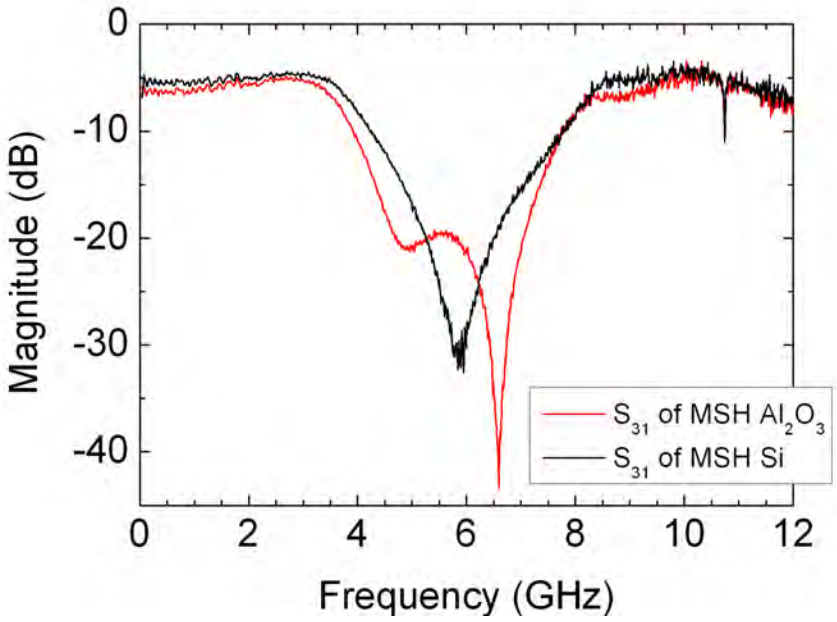

Figure 4.13: Repeated measurement of MSH Nb Si and MSH Nb Al_2O_3 at 4.2 K (average of 50 traces, input power -40 dBm, termination inside). These measurements show a hump and do not confirm the measurements of figures 4.9 and 4.10

This frequency shift of the isolation dip is independent of the termination as both graphs in figure 4.2 show a hump and the same frequency shift.
In summary these measurements show that the frequency shift is independent of the substrate. The origin of the frequency shift is analyzed in more detail in the following.
The first measurements of MSH Au and MSH Cu show no hump and correlated frequency shift. However, the gold and copper samples were also measured a second time. This reference measurements showed a hump as well as a frequency shift under the same experimental conditions (see figure 4.14). The origin of the hump is independent of the conducting material.

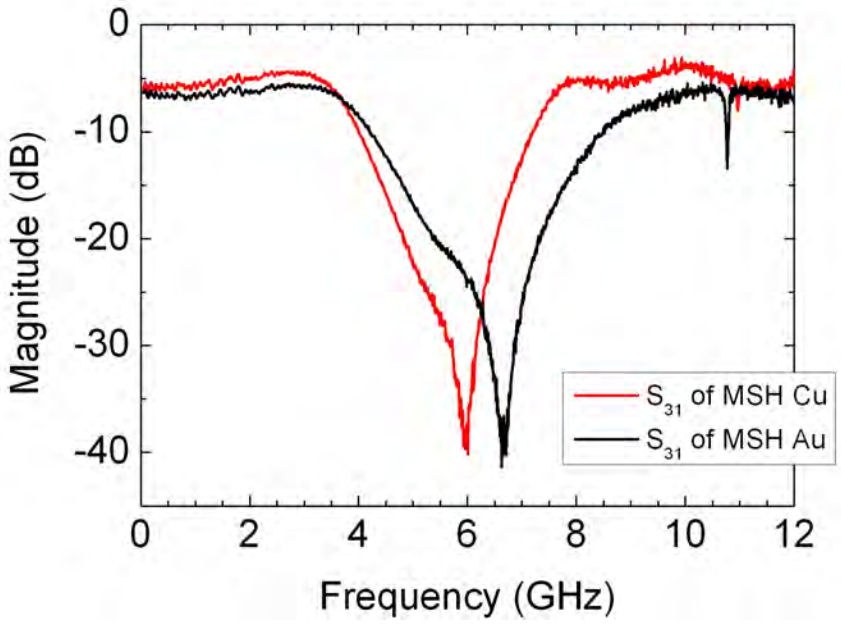

Figure 4.14: Repeated measurement of MSH Cu and MSH Au at 4.2 K (averaged over 50 traces, input power -40 dBm, termination inside). Both isolation spectra show a hump with a correlated frequency shift.

4.1.5 Line Thicknesses

To explore the dependence of the frequency shift on the line thicknesses, the MSH Nb Si sample was fabricated with three different line thicknesses - 200 nm, 500 nm and 1000 nm (see chapter 2.4). The results are shown in figure 4.15. All the measurements were performed with an input power of -40 dBm and the graphs were averaged of 50 traces. The terminations were inside the cryostat.
The three measurements show a small but still visible hump. Thus, the hump is independent of the thickness of the conducting line.
On closer examination the isolation dip seems to move to higher frequencies with increasing line thicknesses but this assumption has to be analyzed in detail. Three measurements with three small humps and three related small frequency shifts are no prove for this statement.
The influence of different ground plane materials on the hump are discussed next.

4.1.6 Ground Planes

In the following, measurements are discussed to check if the origin of the hump might be related to the use of different materials for the ground plane or the way of fixing the sample in the box. Therefore, a 200 nm niobium ground plane was sputtered on the back side of the Al_2O_3 sample to get a superconducting (sc) ground plane. This

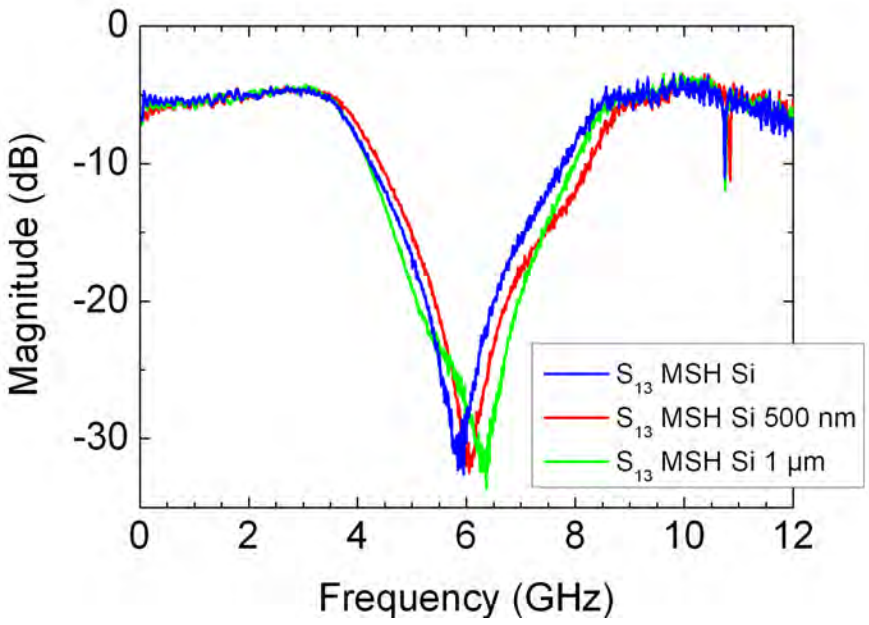

Figure 4.15: Measurements of MSH Nb Si, MSH Nb Si 500 nm and MSH Nb Si 1 μm at 4.2 K (input power -40 dBm, termination inside the cryostat, averaged of 50 traces).

sample was glued with a little bit of silver glue (SG) at all four edges into the box. A second sample without a superconducting ground plane was glued with a drop of SG inside the box, such that the SG acted as ground plane. A third measurement was performed by using a dielectric resin called VGE-7031[1] (GE) to fix the sample into the measurement box. This time the 3 μm thick gold layer of the box is the ground plane.
Figure 4.16 shows the results of the different measurements. Every measurement was performed with termination inside the cryostat and input power -40 dB. 50 traces were averaged. The ground plane influences the isolation of the hybrid rings in an unpredictable manner. However, the origin of the hump could not be related to the presence of a superconducting ground plane or to the different variations of gluing the hybrid ring into the box.
In figure 4.17 the data of two measurements with the same sample and the same superconducting ground plane are shown. For both measurements silver glue was used for the contact between the connectors and the microstrip line. This data shows the hump, the correlated frequency shift and the direction of the frequency shift being independent of the ground plane, the substrate, the conducting line, the box and the measurement setup because these parameters were constant for both measurements.

[1] http://www.lakeshore.com/temp/acc/am_varnishpo.html (2008)

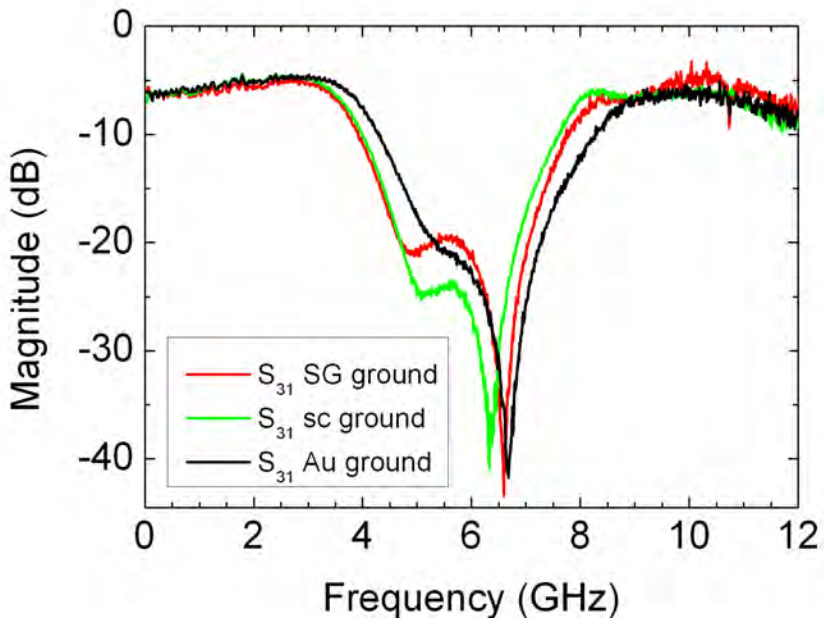

Figure 4.16: Measurements of MSH Nb Al_2O_3 with different ground planes (SG, superconducting niobium and gold) at 4.2 K (input power -40 dBm, termination inside the cryostat, 50 traces averaged)

This measurement led to another possible reason for the frequency shift: the type and quality of the connection between the connectors and the line.

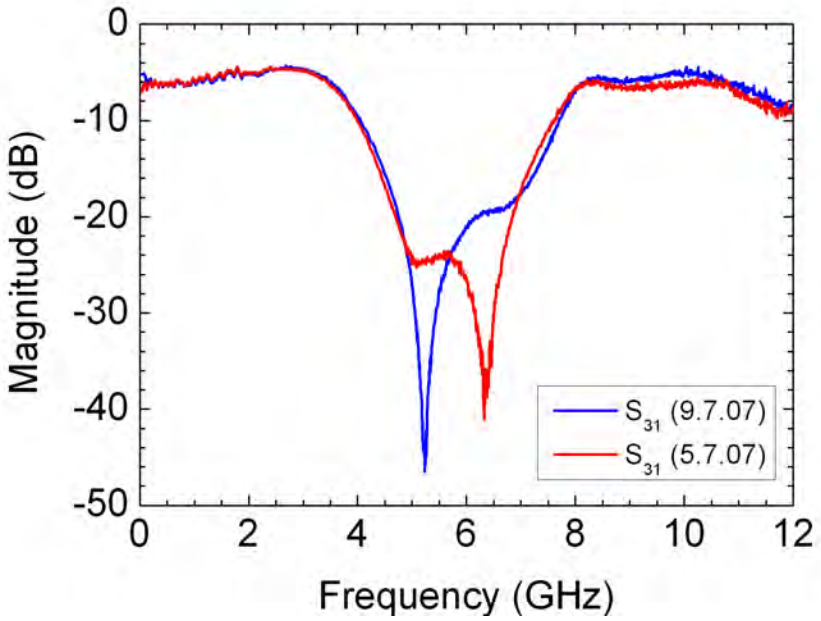

Figure 4.17: Measurements of the same sample that was remounted into the box. Both measurements were performed at 4.2 K (input power -40 dBm, termination inside the cryostat, 50 traces averaged)

4.1.7 Contacting

Usually, the SMA connectors were contacted via silver glue to the strip line of the hybrid ring. To check whether the origin of the hump can be related to the type of contact, different connections were realized via air bonds, soldering or with indium. Before each measurement, the DC resistance between the various ports was measured. A lower resistance indicates a higher quality of the connection and a higher quality of the isolation as figure 4.18 shows. This figure shows the data of the MSH Nb Al_2O_3 sample at 4.2 K with an input power of -40 dBm, an averaging of 50 traces and the termination inside the cryostat. The DC resistance for the low quality measurement are around twice the DC resistance of the high quality measurement where the DC resistances are around 50 Ω. The same figure also shows the data where indium was used for contacting the line with the connectors.

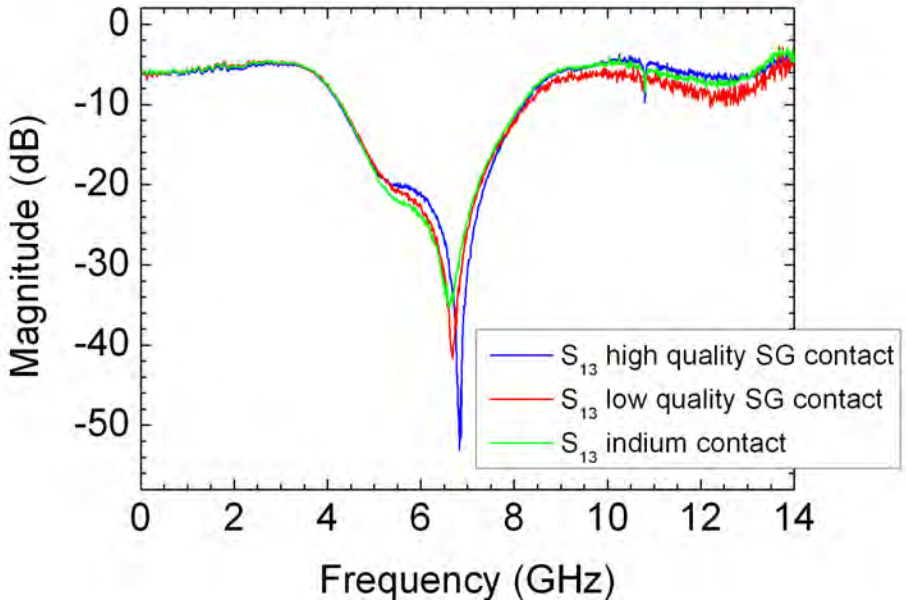

Figure 4.18: Different contacts of MSH Nb Al_2O_3 at 4.2 K (input power -40 dBm, termination inside the cryostat, 50 traces averaged). The indium contacts with the lowest quality have the worst isolation, while with increasing contact quality the isolation increases. The DC resistance of the low quality silver glue contact measurement is around twice of the high quality one.

For one measurement, a sample was contacted with indium which is a very soft metal. Thus, it is possible to squeeze the indium between line and connector. The results of the isolation measurement show that the indium contact is possible but the quality is comparably low.
Since niobium is very difficult to solder, a sample was created with an extra thin gold layer on the contacts (see figure 4.19). This sample was soldered with an

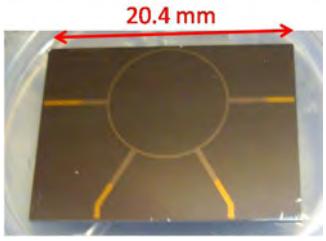

Figure 4.19: MSH Nb Si with an additional gold layer on the arms for soldering

alloy of indium (93 %) and silver (3 %). The temperature for soldering was around 300° C. Other solders were also tried but either the flux of the industrial fabricated ones destroyed the gold layer or solders for lower temperature did not stick to the Rosenberger connectors that are made out of copper-beryllium. The dimensions of the hybrid ring and the connectors require a highly accurate soldering. The gold layer improves the possibility to solder but it is still very difficult. The technique of soldering contacts of micrometer size is not fully developed at the WMI yet. Figure 4.20 shows the result of this measurement.

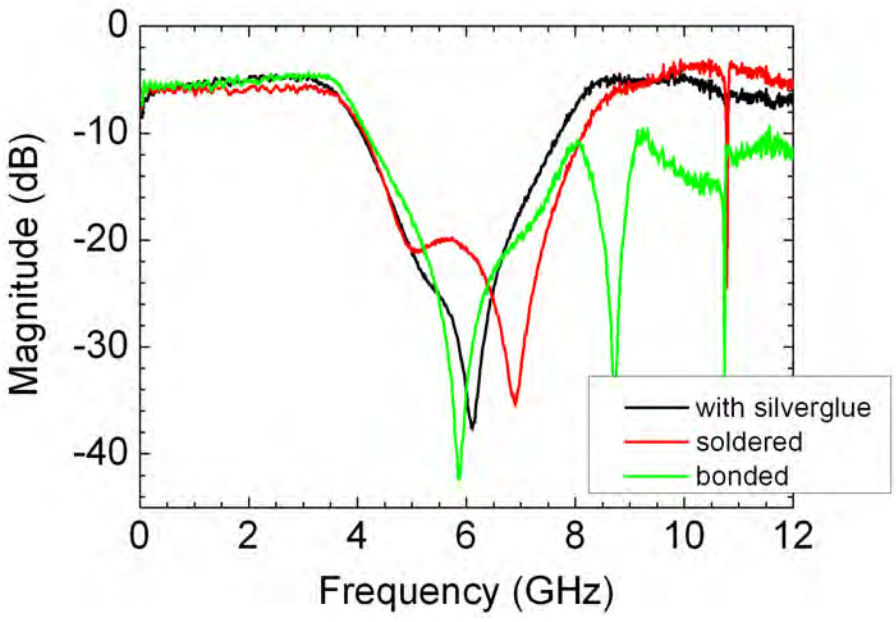

Figure 4.20: Different contacts of line with connector at 4.2 K: silver glue contact, bonded contact of MSH Nb Si and soldered contact of HSM Si with an extra gold layer (input power -20 dBm, termination inside the cryostat, 20 traces averaged)

MSH Cu could be soldered with an industrial fabricated solder: tin (62 %), lead (36 %) and silver (2 %). The measurement results (see figure 4.21) show that solder-

ing is almost as good as SG contacts but much more difficult. Therefore, soldered contacts have a lower quality than contacts with silver glue.

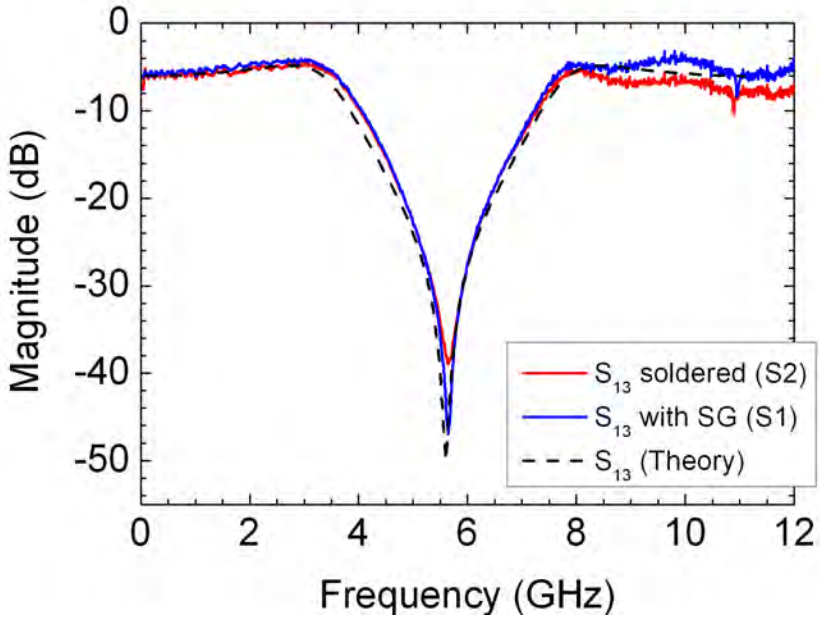

Figure 4.21: Different contacts of MSH Cu at 4.2 K: silver glue contact compared with solder contact (input power -20 dBm, termination inside the cryostat, 20 traces averaged)

Figure 4.20 shows that the measurements with the bonding wires lead to even worse results. A spurious resonance around 8.7 GHz joined the still present hump and frequency shift. The origin of this resonance might be related to the reactive inductances and capacitances of the bonding wires in series with the hybrid ring.
The presented measurements lead to a dependence of the frequency shift on the quality of the contacts. Figure 4.22 gives an impression how sensitive the contacts are. Since the spectra of the MSH Cu hybrid ring are visible at room temperature it was possible to measure changes of the connection between the signal line and the connectors. For this measurement, the input power was -20 dBm and the graph was averaged with 5 traces. The 50 Ω terminations were mounted directly on the box. While measuring the S_{31}-parameter, a smooth stress was imposed upon the connectors by a toothpick. Starting at port three, which was the input port, stress was imposed vertically on the connector's pin. In figure 4.22, one can see that the course of the isolation spectrum changed. After the pin relaxed, the isolation spectra looked similar to the initial measurement. A re-applying showed the irreproducibility of the experiment. The curve in figure 4.22 shows the isolation spectrum when applying stress a second time on port three differs from the graph that was measured when applying stress for the first time on that port. Imposing stress on port four

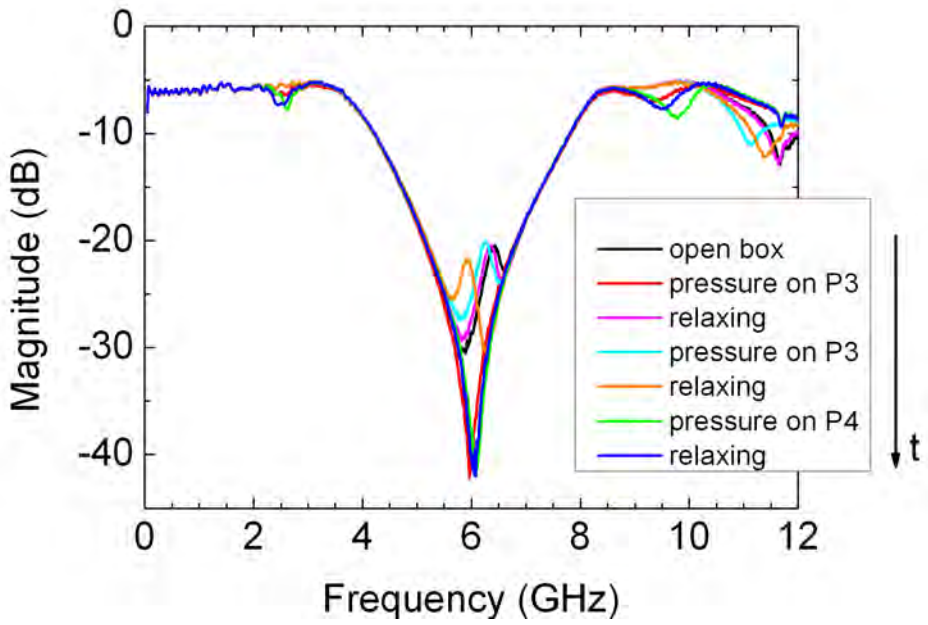

Figure 4.22: Imposing pressure on the contacts at room temperature (5 traces averaged, input power -20 dBm). The arrow indicates the chronological order.

that was a terminated coupling port resulted in a perfect isolation of the hybrid ring that stayed unchanged after removing the stress.
In the end the SG of the connection at port four was in crumbs. These measurements lead to the conclusion that the behavior of the S_{31}-parameter is highly sensitive to the kind and quality of the connection between the strip line and the port and in particular to the quality of the connection between the line and the terminated ports. This behavior could also be seen in other experiments where one of the Rosenberger connectors was not pulled tight. Sometimes when pulling tight the cables of the cryostat or the 50 Ω termination at the connector, this connector was rotated and the result was a broken silver glue at this port. Figure 4.23 shows such a measurement. In this case a DC connection could be measured at low temperatures which excludes an completely broken connection between the line and the connector. After warming up, the connections were investigated under an optical microscope: three out of four connections showed capillary cracks. This again shows that the hybrid characteristics depend sensitively on possible reflections at the contacts.
The transition between the different materials excites reflections that are influencing the isolation. These reflections depend on the materials. A transition from a superconductor to a normal conductor leads to more reflections than from normal to normal conductor. This hypothesis is supported by the temperature dependence of MSH Nb Si in figure 4.5. The superconducting hybrid ring shows more additional features of the isolation spectrum than the non superconducting one at 10 K.

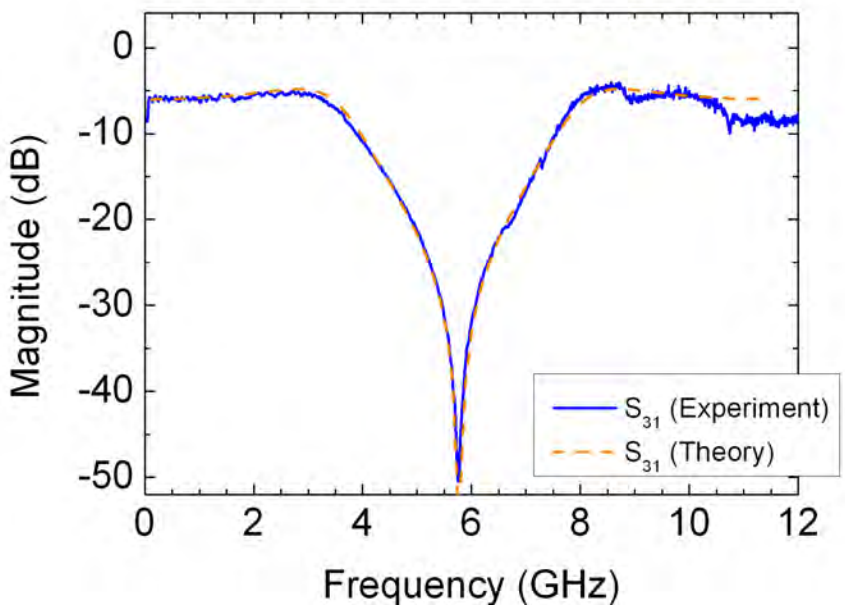

Figure 4.23: Measurement of MSH Nb Si with superconducting ground plane (20 traces averaged, input power -20 dBm, termination inside the cryostat)

4.2 Measurements on CPW Hybrid Rings

Basic transmission line theory does not distinguish between CPW and MS hybrid rings. However, CPW geometries are in general more difficult to fabricate and as the following measurements will show, the transmission spectra of the CPW hybrid rings differ from the transmission spectra of the MS hybrid rings.

4.2.1 H 3: With and Without Inner Ground Plane

The H 3 AE hybrid ring was designed and measured by Andreas Emmert within his diploma thesis [24]. There, the measured transmission spectra showed additional peaks. The origin of these peaks can be related to the bonding wires that were used to contact the inner ground plane to the outer ground planes. To analyze this hypothesis, the H 3 EH was designed having exactly the same dimensions as the H 3 AE except the missing inner ground plane ring.
H 3 AE was fabricated on sapphire and measured with an input power of -10 dBm. The terminations were inside the cryostat. To characterize the additional peaks, H 3 EH was manufactured on silicon and measured. The value of the input power was -20 dBm and the terminations were also mounted directly onto the box as in the measurement of H 3 AE. In both cases, the data were not averaged. Figures 4.24 and 4.25 show the comparison of these measurements.
It is obvious that both measurements are not comparable with transmission line theory but both measurements show a similar behavior: the isolation and coupling is destroyed by a peak at the center frequency. This peak is shifted depending on the substrate of the sample. The H 3 sample was designed for sapphire but the H 3 sample without the inner ground plane was produced on silicon. The slightly different effective permittivity leads to different phase velocities directing to different center frequencies and to shifted peaks.
$\lambda_0 = v_\mathrm{p}/f_0$ and $v_\mathrm{p} = c/\sqrt{\varepsilon_\mathrm{eff}}$ result in

$$\frac{v_\mathrm{p,Si}}{v_\mathrm{p,Al_2O_3}} = \frac{f_\mathrm{0,Si}}{f_\mathrm{0,Al_2O_3}} = \sqrt{\frac{\varepsilon_\mathrm{eff,Al_2O_3}}{\varepsilon_\mathrm{eff,Si}}}$$

With the formulas from chapter 2.2.3 the calculated effective permittivities are 5.6 for H 3 on sapphire and 6.3 for H 3 on silicon. This leads to

$$\frac{f_\mathrm{0,Si}}{f_\mathrm{0,Al_2O_3}} = 0.94.$$

The frequency shift at the center frequency 7.5 GHz is around 400 MHz. This fits quiet well with the observed frequency shift of the peaks. It can be concluded that the peaks in the transmission spectra depend on the structure of the H 3 Hybrid ring and are not box resonances or setup depending artifacts.
To characterize this behavior, two other sample were fabricated - one was designed with formulas that were proposed by reference [37] and the dimensions of the other one were copied from Heimer et al. [42]. Both hybrid rings take the asymmetry of the missing inner ground plane into account.

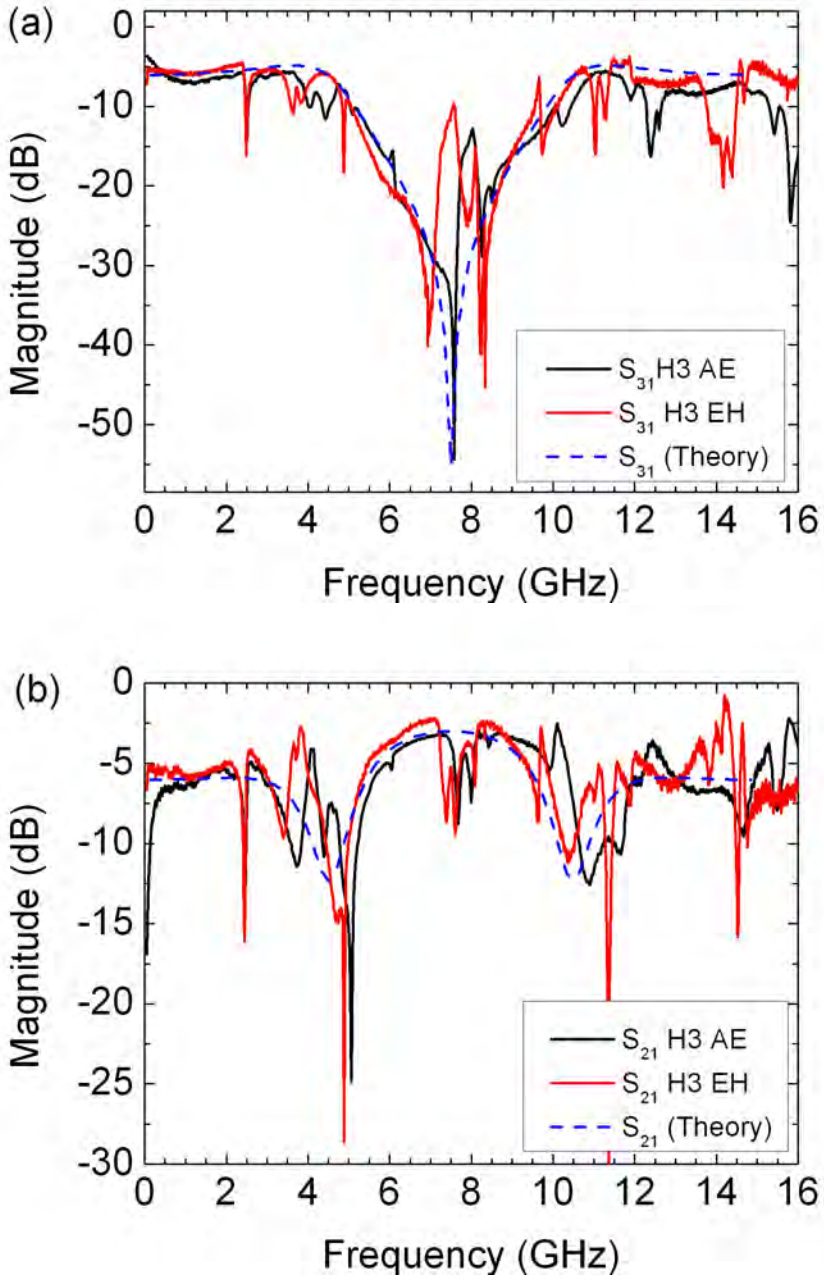

Figure 4.24: Comparison of H 3 AE (H 3 with inner ground plane) and H 3 EH (H 3 without inner ground plane) at $T = 4.2\,\mathrm{K}$. H 3 AE was designed, fabricated and measured by A. Emmert [24]. (a) shows the isolation spectrum S_{31} and (b) the S_{21} coupling. The isolation and the 3 dB coupling are destroyed by additional peaks at the center frequency.

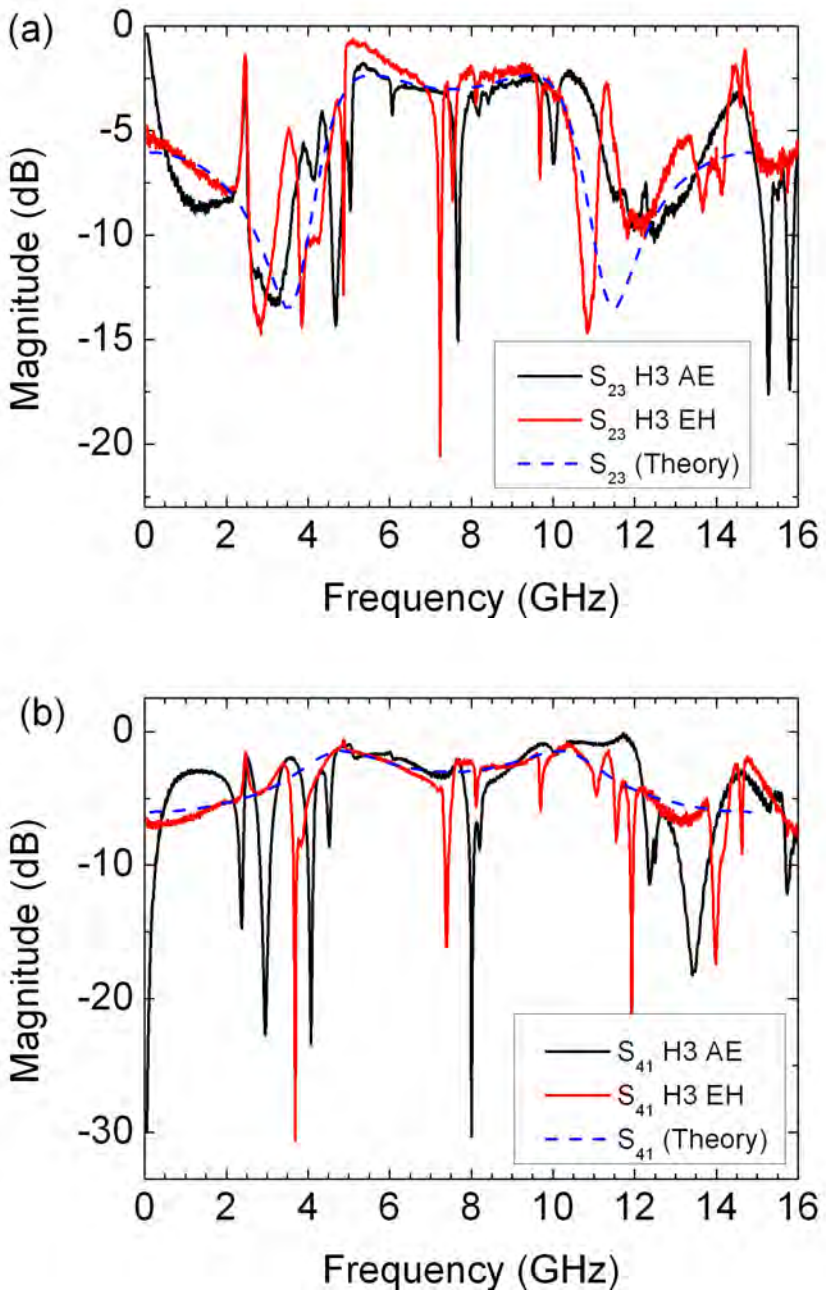

Figure 4.25: Comparison of H 3 AE (H 3 with inner ground plane) and H 3 EH (H 3 without inner ground plane) at $T = 4.2\,\mathrm{K}$. H 3 AE was designed, fabricated and measured by A. Emmert [24]. (a) S_{32} coupling, (b) S_{41} coupling. The coupling at the center frequency is destroyed by an additional peak at all four measurements.

4.2.2 CPW 1

The characteristic impedance of the geometry CPW 1 was calculated with the formulas from reference [37]. This hybrid ring was measured twice, once without and once with bonded airbridges close to the T-junctions for the connection between the ground planes, as one can see in figure 4.26. Figure 4.27 shows the measured data of

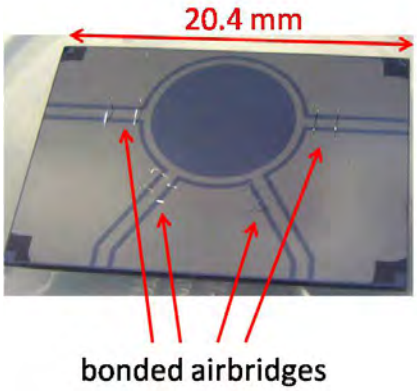

Figure 4.26: CPW 1 hybrid ring with two bonded airbridges close to the T-junctions of the arms.

the CPW 1 hybrid ring. Both measurements of the hybrid ring was performed with an input power -20 dBm and the 50 Ω terminations were inside the cryostat. The measurement of the CPW without bonded airbridges was averaged with 30 traces and the one with the bonded airbridges was not averaged.
Both measurements show peaks in the transmission spectra that cannot be explained by theory.
On the other hand these measurements show the influence of the bonded airbridges. The bonding wires lead to reactive capacitances and inductances. A. Emmert analyzed the influence of bonding wires in reference [24], too. In his theses the bonding wires had similar effects on the measured S_{31}-parameter. It seems that the bonded airbridges contribute to an unwanted crosstalk of ports that ought to be isolated.
The here observed additional peaks are similar to the ones of the H 3 AE and H 3 EH hybrid rings. This leads to the conclusion that also the omitted inner ground plane results in no improvement compared with the H 3 AE hybrid ring. However the isolation spectrum seems to be smoother. Thus, an influence of the inner ground plane cannot be excluded.

4.2.3 CPW 2

For analyzing the peaks in the transmission spectra of the CPW hybrid rings, a structure that was described in a publication by Heimer et al. [42] was fabricated. The line widths of the arms and the ring of this hybrid were calculated with Sonnet

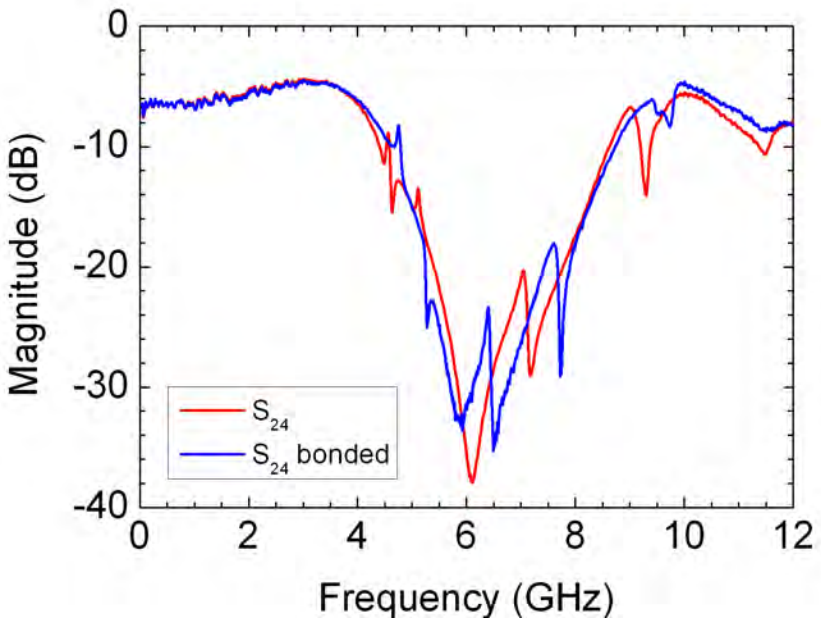

Figure 4.27: Measurement of CPW 1 at 4.2 K with and without bonded airbridges (input power -20 dBm, termination inside, 30 traces averaged (without bonded airbridges), not averaged (with bonded airbridges)). The airbridges influence the behavior of the isolation spectra of the CPW hybrid ring.

Software[2]. The radius of the hybrid ring was adapted to the size of the silicon substrate. The radius of 10.25 mm that was used in reference [42] results in a center frequency of 3 GHz. The radius of 4.2 mm that was used within this diploma thesis ends in a center frequency of 6 GHz.
The hybrid ring (CPW 2) showed peaks close to the center frequency in the isolation spectra. These peaks cannot be explained. Figure 4.28 presents the measurements of the isolation spectra S_{31} and S_{24}. The peaks occur for both data sets at the same frequency and with the same intensity.
By comparing the measurements of figure 4.28 to data presented in reference [42] (see figure 4.29) it can be concluded that the problems with the CPW hybrid rings are due to the setup scheme such as cables. This is supported by a S-parameter measurement of CPW 2 that was performed in Erlangen (see figure 4.30) at the chair of experimental physics (superconductivity) at the Friedrich-Alexander-Universität Erlangen-Nürnberg.

[2]Sonnet Software is a registered trademark of Sonnet Software, Inc., Liverpool, NY.

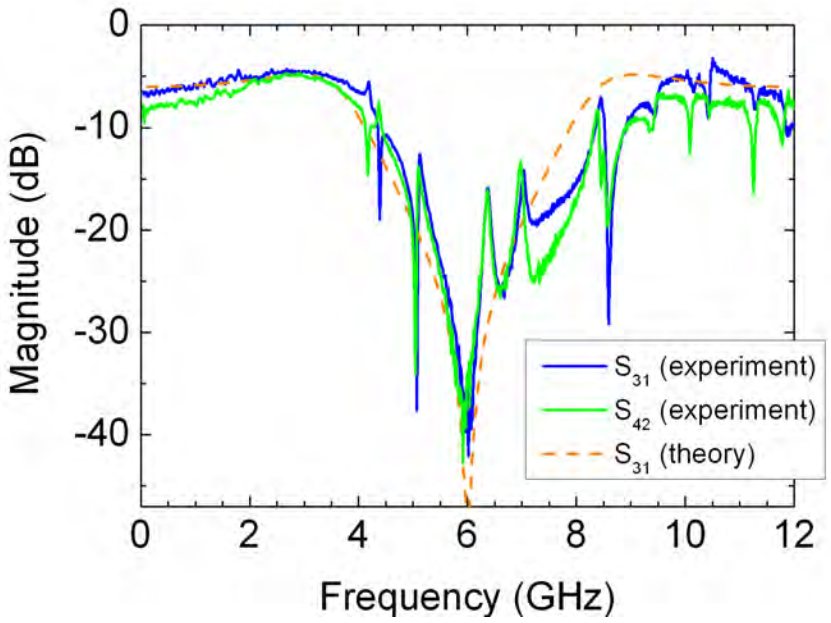

Figure 4.28: Measurement of the isolation of CPW 2 at 4.2 K (input power -40 dBm, termination inside, averaged of 30 traces)

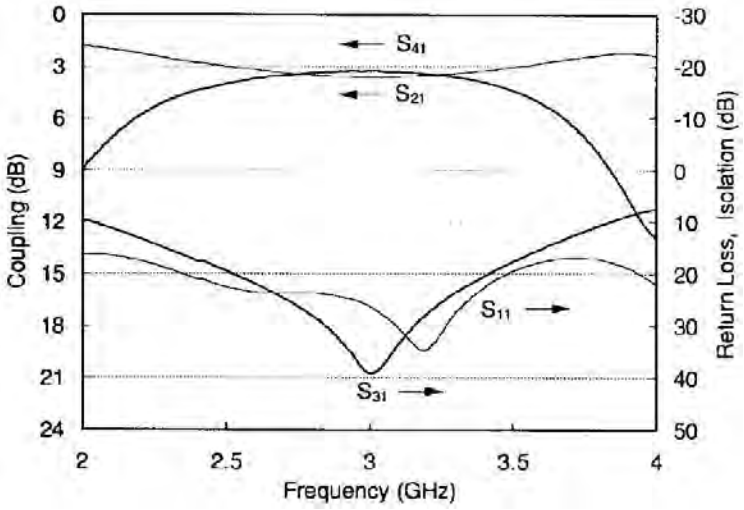

Figure 4.29: Measured data of Heimer et al. [42]. The hybrid ring was designed for a center frequency of 3 GHz. The S_{31}-parameter fits quiet well with that center frequency.

4.3 LTLSM-Measurements

The S-parameters are very useful to characterize a perfect hybrid ring but if the spectra of the parameters differs from the theory the S-parameters cannot explain the origin of the problem. For further analysis of the frequency shift of the MS hybrid ring's isolation spectra and of the CPW hybrid ring's peaks a new method had to be used, measuring the hybrid ring with a low temperature laser scanning microscope (LTLSM). This technique is based on the principle of scanning a focused laser beam across the sample and simultaneously recording the electrical response of the sample. Principally a change of any measured S-parameter's characteristic of the hybrid ring due to local heating or absorption of photons may serve as the response signal.
A continuous microwave signal is fed into one port of the hybrid ring. The output port is connected to a diode which measures the power transmitted through the hybrid as a function of the laser impact coordinate. The change of the transmitted power can than be plotted versus the laser coordinate.

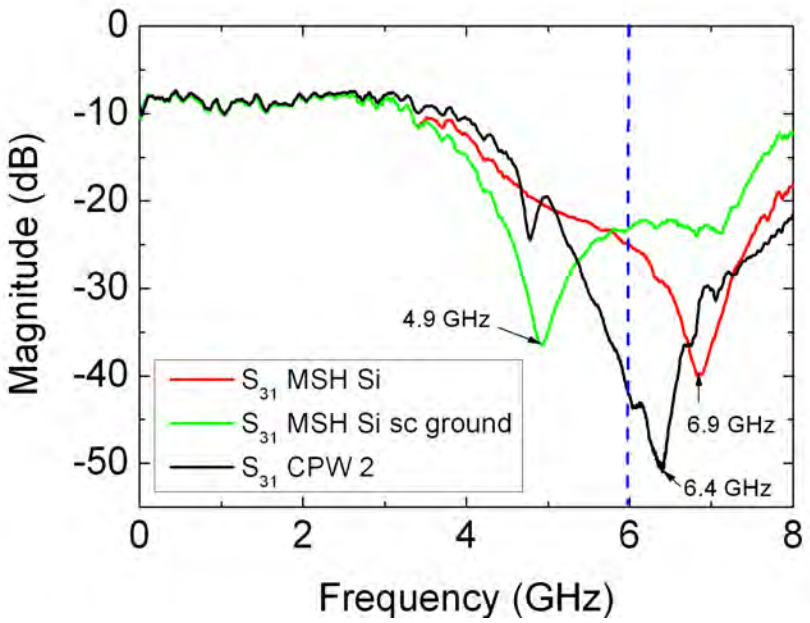

Figure 4.30: Measurement of the isolation of MSH Nb Si, MSH Nb Si with a superconducting ground plane and CPW 2 at 4.2 K: input power -20 dBm, termination inside, not averaged. Each measurement shows a center frequency different of 6 GHz.

These measurements were done with three hybrid rings: MSH Nb Si, MSH Nb Si with superconducting ground plane and CPW 2. The two MS samples were chosen to analyze the influence of a superconducting ground plane. CPW 2 was chosen,

because it promised the best results of the coplanar waveguide hybrid rings so far. The S_{31}-parameters of figure 4.30 were directly measured before scanning the sample. For the measurements of the CPW 2 sample and the MSH Nb Si hybrid ring with niobium as ground plane, port two was used as the input port, thus, ports one and three are the coupling ports while port four is the output port. The MSH Nb Si sample was measured by terminating ports four and two using port one as input and port three as output port. The isolation frequencies were found to be 6.9 GHz for the MSH Nb Si sample, 4.9 GHz for the MSH Nb Si hybrid ring with the superconducting ground plane and 6.4 GHz for CPW 2. So each sample was measured at 6 GHz which is the theoretical center frequency and at its measured center frequency.
Because the circumference of the hybrid ring is $3/2\lambda_0$, one expects minima at the input and output ports and one on the half ring from port one to port four (see figure 4.31) at the center frequency f_0. The maxima are on the two terminated ports and

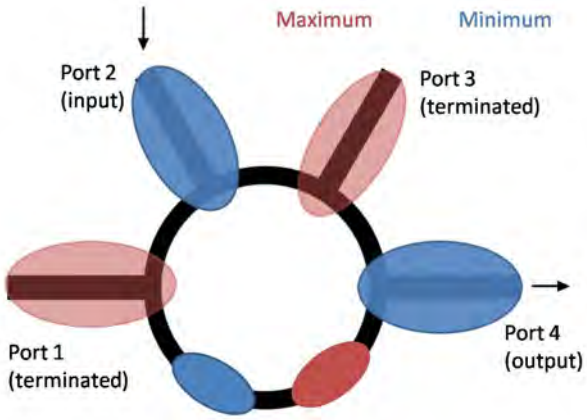

Figure 4.31: Expectation of the LTLSM-measurements of the hybrid rings at the center frequency.

also one on the half ring from port one two port four. At any other frequency the maxima and minima are expected to be shifted.

MSH Nb Si

The first LTLSM-measurement was performed with the MSH Nb Si sample - niobium on silicon. This measurement was done with a 5 times magnification on the used microscope. Each picture shows therefore just a small section of the hybrid ring as one can see in figure 4.32(a). The scaling of each picture differs because the control software chose the optimum scaling for each picture. This scaling problem could be dealt by re-scaling the data using Origin[3]. One can see that the minimum which should occur at port three is slightly shifted. The same behavior was recognized when measuring the MSH Nb Si sample with a niobium ground plane. The direct

[3]OriginLab Corporation, http://www.originlab.de (2008)

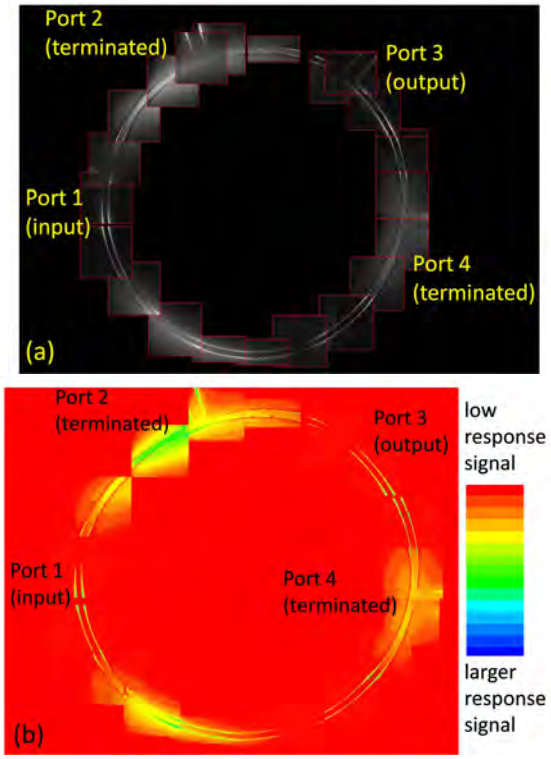

Figure 4.32: LTLSM-measurements of the MSH Nb Si sample at 6 GHz (a) composition of the pictures, each picture has its own amplitude scaling, (b) composition of graphs re-scaled by Origin. global.

comparison of the interesting ports two, three and four leads already to some kind of mismatch and an unperfect superposition of the waves on the hybrid ring (see figure 4.33). The different scaling of the 6 GHz and the 6.9 GHz measurements is due to the different input powers (-27 dBm at 6 GHz and -17 dBm at 6.9 GHz) that were necessary to optimize the pictures. Over all, the measurements agree well with the measured S_{31}-parameter.

MSH Nb Si with Superconducting Ground Plane

The MSH Nb Si sample with niobium as ground plane was measured at two different frequencies - at 6 GHZ and at its previous measured center frequency 4.9 GHz. The measurements are shown in figure 4.34.
The 6 GHz frequency measurements (figure 4.34(a) and (b)) do not show the maxima and minima where they are expected but they show nodes and antinodes on the arms of the hybrid ring. The reason for these standing waves could be reflections on the intersections of the connection from the strip line to the connectors. These reflections superimpose with the wave on the ring which leads to a shift of the maxima and minima. With the shifted maxima and minima the calculated center frequency of

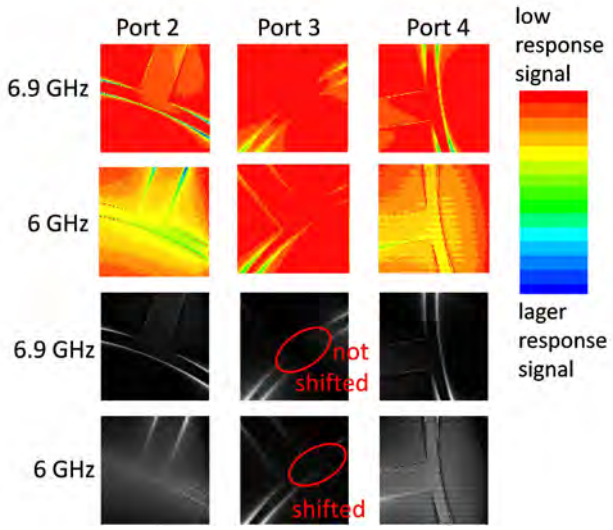

Figure 4.33: LTLSM-measurements of the MSH Nb Si sample at 6 GHz and at 6.9 GHz: Port two, three and four are shown each once at 6 GHz and at 6.9 GHz. The scale of the first row is around ten times the scale of the second row. Each picture in the third and last row is optimal scaled to show the response signal.

6 GHz is not the center frequency anymore. The "new" center frequency depends on the amplitude of the reflections which differs depending on the quality of the contacts between the strip line and the connector. Because the amplitudes of the signal on the -3 dB coupling ports are much higher than the amplitudes of the signals on the isolation ports, the amplitude of the reflections on the coupling ports is also much higher than the amplitude of the reflections on the isolation ports. Thus, the contacts on the coupling ports are more sensitive than the contacts of the isolation ports. This agrees well with the observations of the measurement shown in figure 4.22.
The pictures show that the extension along the ring of a maximum is larger than for the minimum. Therefore, the S-parameters that describe the coupling (S_{21}, S_{41} and S_{32}) are not as strongly affected as the S_{42} and S_{31}-parameters.
The figures 4.34(c) and (d) show the LTLSM-data at the measured center frequency of 4.9 GHz. Here the maxima and especially the minima coincide better with the ports than at the 6 GHz measurement. This results in the new isolation frequency. In general the pictures of figure 4.34 are in good agreement with the measured S_{42}-parameter of figure 4.30.

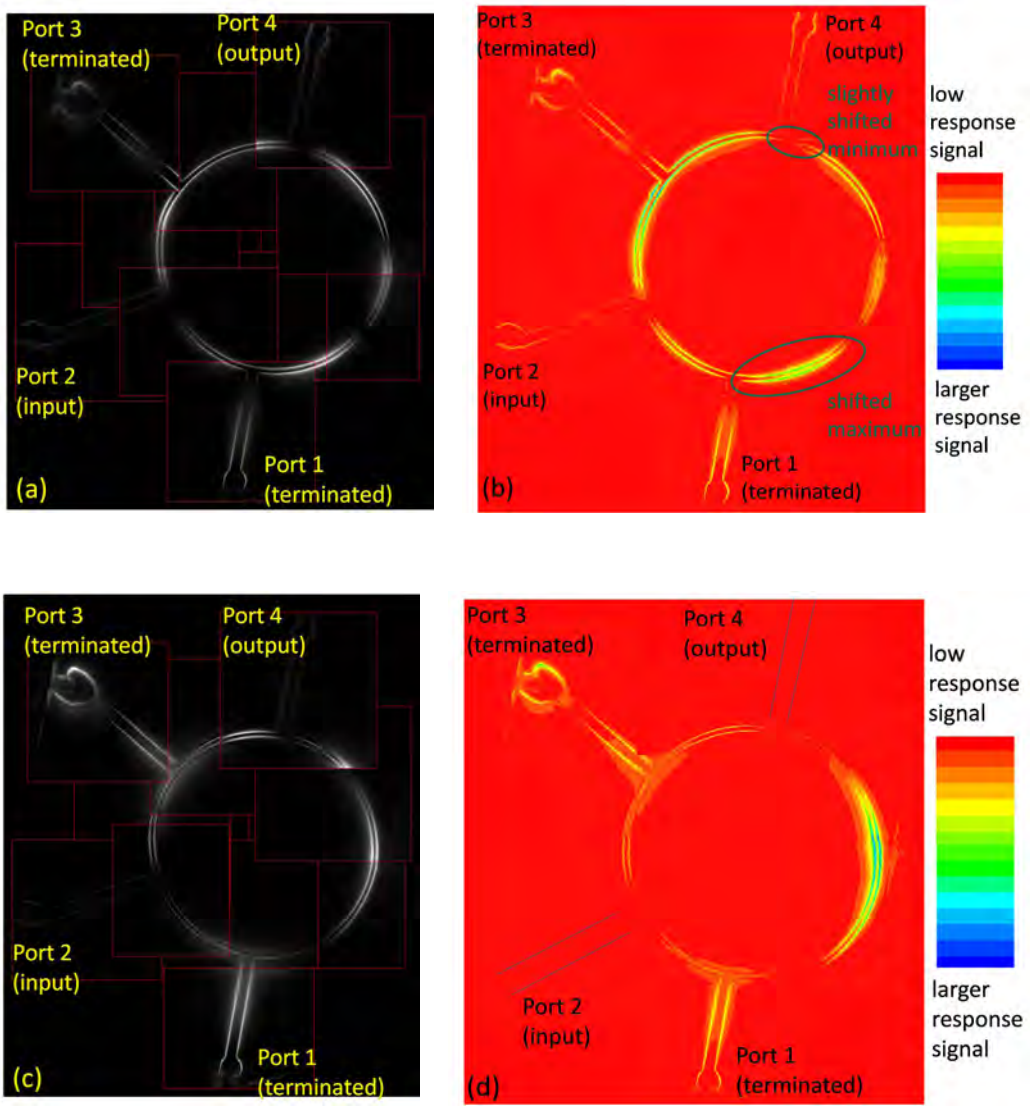

Figure 4.34: LTLSM-measurements of the MSH Nb Si sample with a superconducting ground plane. (a), (b) pictures at 6 GHz: (a) composition of the pictures, each picture has its own amplitude scaling, (b) composition of graphs re-scaled by Origin. (c), (d) the same as (a) and (b) but for the measured center frequency 4.9 GHz.

CPW 2

The results of the LTLSM-measurements of the coplanar waveguide hybrid ring CPW 2 are shown in figure 4.35.
In this case the theoretic and the measured center frequency are comparable. Thus, the maxima and minima are shifted by a smaller amount as the ones of the MSH Nb Si measurements. The S_{31}-measurement in figure 4.30 did not show an extra peak like the isolation spectrum of the coplanar waveguide hybrid rings before but behaved like the MS hybrid ring spectra. So, it was not possible to analyze the extra peak with this method. Two points of the shown pictures in figure 4.35 are to be mentioned - the asymmetric response power signal on port four and the light spot on the edge of the ground plane. The light spot shows a high voltage density. In principal this can be explained by the divergent electric field at the edge but port four is the isolation port and it is not expected to show a high response power signal. A response signal like this is more highly expected on one of the coupling ports. The asymmetric response power signal cannot be explained.
At the moment it is impossible to say wether the extra dips are linked with the asymmetric behavior of the hybrid ring or if the dips are independent of that asymmetry. In any case, one single picture has too little explanatory power to say more about the untypical behavior of the coplanar waveguide hybrid rings.

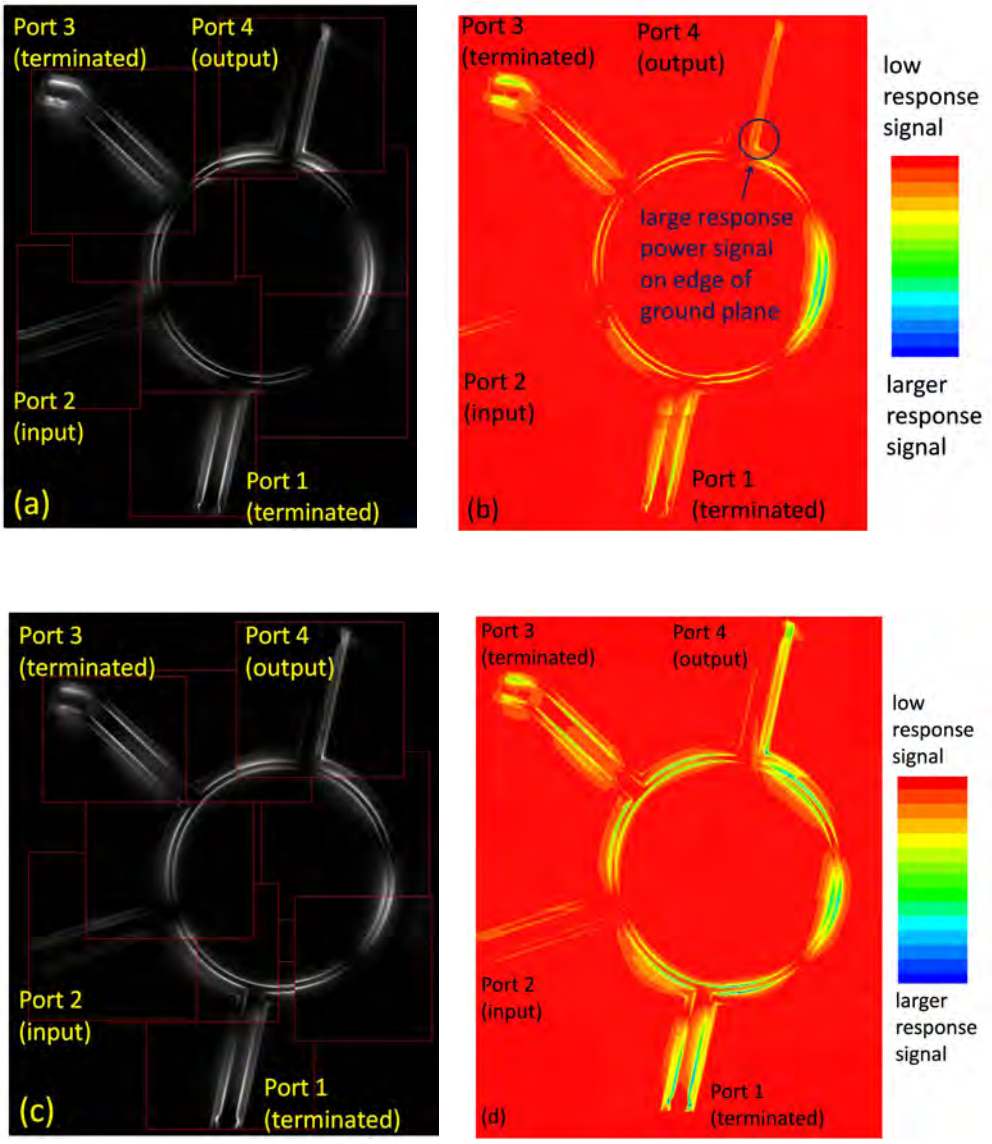

Figure 4.35: LTLSM-measurements of the coplanar waveguide hybrid ring CPW 2. (a), (b) pictures at 6 GHz: (a) composition of the pictures, each picture has its own amplitude scaling, (b) composition of graphs re-scaled by Origin. (c), (d) the same as (a) and (b) but for the measured center frequency 6.4 GHz.

5 Time Domain Measurement

The hybrid ring should act as a microwave beam splitter and superpose the applied signals at port one and port three. This interference was measured with two hybrid rings at room temperature in the time domain: a commercial hybrid ring from MITEQ[1] and the MSH Cu sample. Two microwave signals at the center frequency are fed into two input ports of the hybrid ring and the constructive and destructive interference is detected at the two output ports.

5.1 MITEQ Hybrid Ring

First, the measurements and the calculation of the commercial microstrip hybrid ring from MITEQ will be presented. The measured amplitudes A_2 and A_4 of the output ports two and four will be compared to values computed for perfect interference.

5.1.1 Measurement

The superposition of two input signals was performed by a microstrip hybrid ring bought from MITEQ. This hybrid ring has a line width of the arms of 406.4 μm, while the line width of the ring is 736.6 μm. It consists of four layers of conducting materials on the substrate: at the bottom an alumina layer, then a tantalum (III) nitride layer (50-60 nm) and a layer of titanium-tungsten (100-200 nm). The top layer is made of 2.54-3.05 μm thick gold. This hybrid ring shows perfect S-parameter spectra and is predestined to analyze the fundamental working principle of the hybrid ring (see figure 5.1).
The measurement setup is shown in figure 5.2. The attenuation of the different cables at 6 GHz has been measured with the NVA that had been already used for the S-parameter measurements.
A microwave of power 0 dBm - corresponding to a power of 1 mW - at a frequency of 6 GHz is emitted by a microwave generator (Rohde&Schwarz®: SMP 04, Microwave Signal Generator[2]), split by a power divider (PD) (Agilent Technologies: 11667C Power Splitter[3]) and then connected to port one and three of the hybrid ring. The superposed signals at port two and four are detected by an oscilloscope (LeCroy: WaveMaster^{TM} 8600A[4]).
The detected voltages are shown in figure 5.3. The amplitudes of the measured data

[1] MITEQ, http://www.miteq.com/ (2008)
[2] R&S®, http://www.rohde-schwarz.com/ (2008)
[3] Agilent Technologies, http://www.agilent.com (2008)
[4] LeCroy, http://www.lecroy.com/homepage/germany/default.aspx (2008)

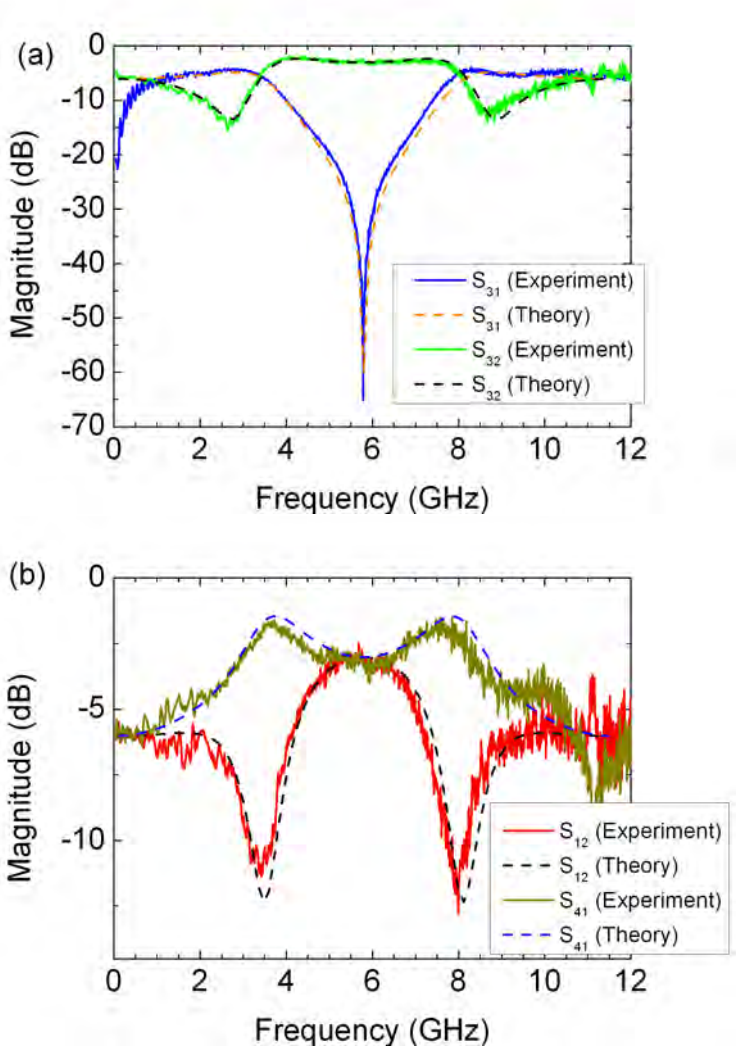

Figure 5.1: Measurements of the S-parameters od the MITEQ hybrid ring at 4.2 K. S_{31} is averaged with 50 traces, the other measurements are not averaged.

are $A_2 = 125\,\mathrm{mV}$ and $A_4 = 60\,\mathrm{mV}$ with an error of 2 mV each.

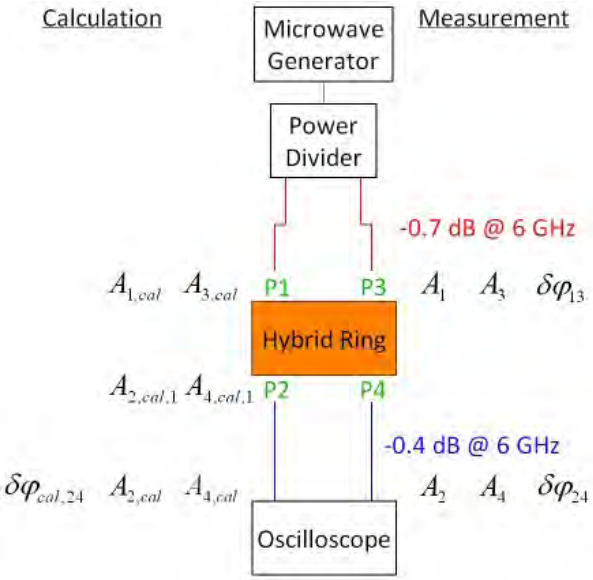

Figure 5.2: Setup scheme for applying two signals to the hybrid ring: the cables from the power divider to the hybrid ring (red) have an attenuation of -0.7 dB at 6 GHz and the cables from the hybrid ring to the oscilloscope exhibit an attenuation of -0.4 dB at 6 GHz

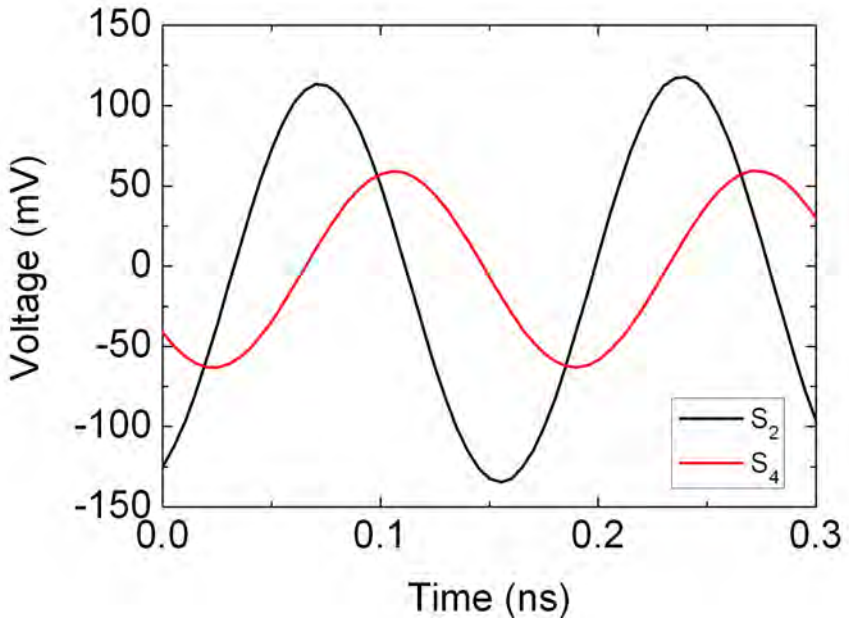

Figure 5.3: Measured signals at port two and four of the hybrid ring

5.1.2 Calculation

In the following section this measured data will be compared with the calculated values. This computing based on transmission theory was performed by using the calculated signals at port one and three of the hybrid ring to compute the voltage signals at port two and four.
While the attenuation in the PD can be neglected the attenuation in the cables connecting the microwave generator to the hybrid ring are $D_1 = -0.7\,\mathrm{dB}$ at $f = 6\,\mathrm{GHz}$ with an error of $\Delta D_1 = 0.05\,\mathrm{dB}$. The attenuation of the cables connecting the hybrid ring and the Oscilloscope are $D_2 = -0.5\,\mathrm{dB}$ at $f = 6\,\mathrm{GHz}$ with an estimated error of $\Delta D_2 = 0.02\,\mathrm{dB}$.
The following calculations were done with the formulas:

$$p_\mathrm{W} = 10^{p_\mathrm{dB}/10} 10^{-3}\,\mathrm{W} \tag{5.1}$$

$$A = \sqrt{2 p_\mathrm{W} 50\,\Omega} \tag{5.2}$$

where p_dB is the power expressed in decibel and p_W is the power in watt. A is the voltage amplitude.
Thus, the PD divides the 0 dBm signal in two -3.01 dBm signals. The attenuation of the cables leads to signals of $p_{\mathrm{cal},0} = -3.71\,\mathrm{dBm}$ at the input ports. This is equal to $p_{\mathrm{cal},0} = 0.426\,\mathrm{mW}$ or to $A_{\mathrm{cal},0} = 206\,\mathrm{mV}$. The zero in the formulas represents the signal *before* the readout of the oscilloscope. The reading of the oscilloscope of 6 GHz signals is attenuated by -3 dB compared to the reading of low frequency signals which is equal to a factor of 1/2. This is due to the analog bandwidth at 50 Ω. Thus, the calculated amplitude has to be divided by a factor of two and is given by $A_\mathrm{cal} = A_{1,\mathrm{cal}} = A_{3,\mathrm{cal}} = 103\,\mathrm{mV}$. The measured amplitudes at the input ports of the hybrid ring $A_1 = 96\,\mathrm{mV}$ and $A_3 = 105\,\mathrm{mV}$ were measured by connecting the PD directly with the oscilloscope and agree quiet well with the calculated values. The difference of the measured amplitudes is due to the input amplifier of the two used inputs of the oscilloscope.
The 0.05 dB error in the attenuation leads to an error of 1 mV in the amplitude, which was calculated by Gaussian's error propagation:

$$\Delta A_\mathrm{cal} = \sqrt{\left(\frac{\partial A_\mathrm{cal}}{\partial D_1}\Delta D_1\right)^2} = \left(\frac{1}{20}\ln(10) A_\mathrm{cal}\right) \cdot 0.05\,\mathrm{V} = 1.2\,\mathrm{mV}$$

The measured phase shift of the two signals S_1 and S_3 is $\delta\varphi_{13} = 0.29\pi$. Thus, the measured voltages are

$$S_1 = 96\,\mathrm{mV} \cdot \cos\left(6\,\mathrm{GHz}/(2\pi) \cdot t\right)$$

$$S_3 = 105\,\mathrm{mV} \cdot \cos\left(6\,\mathrm{GHz}/(2\pi) \cdot t + 0.29\pi\right).$$

The calculated signals are

$$S_{1,\mathrm{cal}} = 103\,\mathrm{mV} \cdot \cos\left(6\,\mathrm{GHz}/(2\pi) \cdot t\right)$$

$$S_{3,\mathrm{cal}} = 103\,\mathrm{mV} \cdot \cos\left(6\,\mathrm{GHz}/(2\pi) \cdot t + 0.29\pi\right).$$

These signals are calculated to allow a comparison to the measured data. Since this data is reduce by a factor of two due to the bandwidth of the input amplifier, the calculated signals have to be multiplied by a factor of two to be used for the computation of the constructive and destructive interference of the hybrid ring. It is useful to compute the amplitudes at the output ports with the calculated and not with the measured amplitudes of the input signals because the measured amplitudes are deviated due to the input amplifier of the oscilloscope. So the signals $S_{2,\mathrm{cal},1}$ and $S_{4,\mathrm{cal},1}$ on the output ports of the hybrid rings are

$$S_{2,\mathrm{cal},1} = (2S_{1,\mathrm{cal}} + 2S_{3,cal})/\sqrt{2} = \frac{4A_{\mathrm{cal}}}{\sqrt{2}} \cos\left(\frac{2\omega t + \delta\varphi_{13}}{2}\right) \cos\left(\frac{\delta\varphi_{13}}{2}\right) \tag{5.3}$$

and

$$S_{4,\mathrm{cal},1} = (2S_{3,cal} - 2S_{1,\mathrm{cal}})/\sqrt{2} = \frac{4A_{\mathrm{cal}}}{\sqrt{2}} \sin\left(\frac{2\omega t + \delta\varphi_{13}}{2}\right) \sin\left(\frac{\delta\varphi_{13}}{2}\right) \tag{5.4}$$

with $\delta\varphi_{13} = 0.29\pi$, $\omega = 6\,\mathrm{GHz}/(2\pi)$ and $A_{\mathrm{cal}} = 103\,\mathrm{mV}$. To compare the calculation with the measurement, it is necessary to consider the attenuation of the cables from the hybrid ring to the oscilloscope. The amplitudes of the emitted signals at the output ports of the hybrid ring are $A_{2,\mathrm{cal},1} = 261\,\mathrm{mV}$ and $A_{4,\mathrm{cal},1} = 130\,\mathrm{mV}$. With the given formulas (5.1) and (5.2) it is possible to transform this voltage amplitudes into powers and subtract the attenuation of the cables. By applying the factor 1/2 to the voltage amplitude due to the input amplifier of the oscilloscope, one gets $A_{2,\mathrm{cal}} = 124\,\mathrm{mV}$ and $A_{4,\mathrm{cal}} = 62\,\mathrm{mV}$. The calculated signals are shown in figure 5.4.
A point that has not been yet considered are the reflections at the two input ports. The design of the hybrid ring predicts no reflections on each port at the exact center frequency (see (2.33)). Thus, these reflections were assumed to be negligible.
The calculation of the errors depend on the error due to the attenuation and the error of reading the amplitudes A_1 and A_3.

$$\Delta A_{i,\mathrm{cal}} = \sqrt{\left(\frac{\partial A_{i,\mathrm{cal}}}{\partial D_2}\Delta D_2\right)^2 + \left(\frac{\partial A_{i,\mathrm{cal}}}{\partial A_{i,\mathrm{cal},1}}\Delta A_{i,\mathrm{cal},1}\right)^2} \qquad (i \in \{2,4\})$$

With $A_{i,\mathrm{cal},1} = A_1\cos(\Omega t) \pm A_3\cos(\Omega t + \phi)$ and $\Omega = 6\,\mathrm{GHz}/(2\pi)$ the error of $A_{i,\mathrm{cal},1}$ is

$$\begin{aligned}\Delta A_{i,\mathrm{cal},1} &= \sqrt{\left(\frac{\partial A_{i,\mathrm{cal},1}}{\partial A_1}\Delta A_1\right)^2 + \left(\frac{\partial A_{i,\mathrm{cal},1}}{\partial A_3}\Delta A_3\right)} \\ &= \sqrt{(\cos(\Omega t)\cdot 0.002\,\mathrm{V})^2 + (\cos(\Omega t + 0,13\pi)\cdot 0.002\,\mathrm{V})^2}\end{aligned}$$

which results in $\Delta A_{2,\mathrm{cal},1} = 2.8\,\mathrm{mV}$ which was calculated for $t = 0.16\,\mathrm{ns}$ and $\Delta A_{4,\mathrm{cal},1} = 1.5\,\mathrm{mV}$ for $t = 0.19\,\mathrm{ns}$. Figure 5.4 shows how the times were chosen.

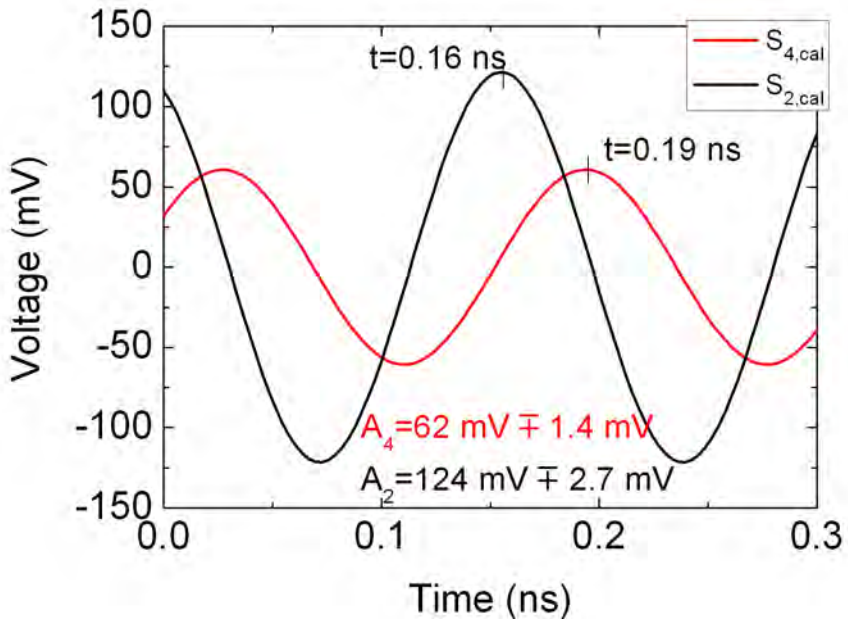

Figure 5.4: Calculated signals at port two and four of the MITEQ hybrid ring

calculation	measurement
$A_{1,\mathrm{cal}} = 103 \pm 1.2\,\mathrm{mV}$	$A_1 = 96 \pm 2\,\mathrm{mV}$
$A_{3,\mathrm{cal}} = 103 \pm 1.2\,\mathrm{mV}$	$A_3 = 105 \pm 2\,\mathrm{mV}$
	$\delta\varphi_{13} = 0.29\pi$
$A_{2,\mathrm{cal}} = 124 \pm 2.7\,\mathrm{mV}$	$A_2 = 125 \pm 2\,\mathrm{mV}$
$A_{4,\mathrm{cal}} = 62 \pm 1.4\,\mathrm{mV}$	$A_4 = 60 \pm 2\,\mathrm{mV}$
$\delta\varphi_{\mathrm{cal},24} = 0.5\pi$	$\delta\varphi_{24} = 0.5\pi$

Table 5.1: Comparison of the calculated and measured amplitudes.

With these values it is possible to get the errors $\Delta A_{2,\mathrm{cal}} = 2.7\,\mathrm{mV}$ and $\Delta A_{4,\mathrm{cal}} = 1.4\,\mathrm{mV}$. So the calculated amplitudes are $A_{2,\mathrm{cal}} = 124 \pm 2.7\,\mathrm{mV}$ and $A_{4,\mathrm{cal}} = 62 \pm 1.4\,\mathrm{mV}$.

Table 5.1 compares the calculated and measured amplitudes. The measured and computed values agree within the uncertainties. The deviation of the amplitudes and the asymmetry of A_1 and A_3 is due to the asymmetric input amplifier of the two input ports of the oscilloscope. S_1 and S_4 were measured with the same input port of the oscilloscope while S_3 and S_2 were measured by the other one.

calculation	measurement
$A_{1,\mathrm{cal}} = 103 \pm 1\,\mathrm{mV}$	$A_1 = 98 \pm 4\,\mathrm{mV}$
$A_{3,\mathrm{cal}} = 103 \pm 1\,\mathrm{mV}$	$A_3 = 109 \pm 4\,\mathrm{mV}$
	$\delta\varphi_{13} = 0.12\pi$
$A_{2,\mathrm{cal}} = 136 \pm 2.8\,\mathrm{mV}$	$A_2 = 112 \pm 2\,\mathrm{mV}$
$A_{4,\mathrm{cal}} = 27 \pm 1.3\,\mathrm{mV}$	$A_4 = 60 \pm 2\,\mathrm{mV}$
$\delta\varphi_{\mathrm{cal},24} = 0.5\pi$	$\delta\varphi_{24} = 0.5\pi$

Table 5.2: Comparison of the computed and measured values of the MSH Cu sample.

5.2 MSH Cu

The copper hybrid ring is measured in the same way as the commercial gold hybrid ring, however, at 5.7 GHz which is the center frequency (see figure 4.12 in section 4.1.3). Since both hybrid rings were not measured at the same time, the rearrangement of the cables and the different isolation frequency results in a phase shift $\delta\varphi_{13} = 0.12\pi$. The amplitudes of the signals S_1 and S_3 are $A_1 = 98\,\mathrm{mV}$ and $A_3 = 109\,\mathrm{mV}$ respectively and are similar to the amplitudes of the measurements on the MITEQ device. Since the layout of the measurement setup and the value of the input power has not changed, the calculated amplitude A_{cal} is again 103 mV.
By using equations (5.3) and (5.4), the calculation of the MSH Cu sample is performed in the same way as in the case of the MITEQ hybrid ring. After considering the attenuation of the cables from the hybrid ring to the oscilloscope and the bandwidth of the input amplifier, one gets $A_{2,\mathrm{cal}} = 136 \pm 2.8\,\mathrm{mV}$ and $A_{4,\mathrm{cal}} = 27 \pm 1.3\,\mathrm{mV}$. The measured amplitudes at port four and two are $A_2 = 112\,\mathrm{mV}$ and $A_4 = 60\,\mathrm{mV}$ with an error of 2 mV each. Table 5.2 compares the measured with the calculated amplitudes of the signals. The difference of the computed and measured values shows, that the copper sample does not behave as a perfect interference device. Reflections at the ports due to impedance mismatch could be the origin of the different measured and calculated amplitudes.

5.3 Reference Measurement

Both the MITEQ device and the MSH Cu, measurements were repeated with an Agilent[5] infiniium DSA80000B oscilloscope at Infineon[6]. This oscilloscope is able to detect signals with a frequency up to 8 GHz. The measurements were repeated to exclude systematic errors due to the bandwidth of the input amplifier of the used LeCroy oscilloscope at the WMI.
The measurements at Infineon confirmed the performance of the commercial MITEQ hybrid ring being superior to that of the copper hybrid ring. The measured and

[5] Agilent Technologies, http://www.home.agilent.com/agilent/home.jspx (2008)
[6] Infineon Technologies AG, http://www.infineon.com/cms/de/product/index.html (2008)

calculation	measurement	
	MITEQ hybrid ring	MSH Cu
$A_{1,\mathrm{cal}} = 135 \pm 1\,\mathrm{mV}$	$A_1 = 133 \pm 4\,\mathrm{mV}$	$A_1 = 133 \pm 4\,\mathrm{mV}$
$A_{3,\mathrm{cal}} = 135 \pm 1\,\mathrm{mV}$	$A_3 = 130 \pm 4\,\mathrm{mV}$	$A_3 = 130 \pm 4\,\mathrm{mV}$
	$\delta\varphi_{13} = 0.13\pi$	
$A_{2,\mathrm{cal}} = 178 \pm 2.8\,\mathrm{mV}$	$A_2 = 173 \pm 4\,\mathrm{mV}$	$A_2 = 118 \pm 4\,\mathrm{mV}$
$A_{4,\mathrm{cal}} = 38 \pm 1.3\,\mathrm{mV}$	$A_4 = 38 \pm 3\,\mathrm{mV}$	$A_4 = 61 \pm 3\,\mathrm{mV}$
$\delta\varphi_{\mathrm{cal},24} = 0.5\pi$	$\delta\varphi_{24} = 0.5\pi$	$\delta\varphi_{24} = 0.5\pi$

Table 5.3: Comparison of the calculated and measured values of the amplitudes of the MITEQ and MSH Cu hybrid ring. The measurements were performed at Infineon.

calculated data is listed in table 5.3.

6 Conclusion

This thesis was motivated by the idea to design and create a superconducting 180° hybrid ring in microstrip and coplanar waveguide geometry that can be used in a homodyne detection scheme. This hybrid ring is a crucial component of the set up scheme presented in chapter one, where a quantum object interacts with the quantized modes of a resonator. This experiment belongs to the class of c-QED experiments.
The dimensions of the hybrid rings were chosen to match the impedance of standard microwave equipment. Different fabrication processes were used to fabricate the hybrid rings with different materials.
The S-parameters measurements of the MS hybrid rings look almost as theory predicts. The coupling parameters fit quite well with the theoretical calculations and the isolation spectra show in general the expected behavior. The sometimes observed frequency shift seems to depend on the quality of the connection of the strip line to the connector and especially to the $50\,\Omega$ terminations. The reflections at the transitions of the different materials depend on the conducting properties of the line. The transition from a superconducting to a normal conducting material is more problematic than the transition between two normal conducting materials. Superconducting materials have lower attenuations in the lines than normal conducting materials. Therefore the reflections on the ports in a superconducting material such as niobium, execute more influences on the signal in the lines than reflections in normal conducting materials. So, the contacts of the gold or copper sample are less sensitive compared to the contacts of the niobium samples.
The reflections on the ports could be visualized by measuring the current density with an LTLSM. In the arms of the hybrid a standing wave became visible which can help to explain the shift of the center frequency. Analyzing these reflections in more detail could be the work of a future diploma thesis.
The present thesis shows that the properties of the MS hybrid rings (except the contacting problem) are almost independent of the conducting material. Thin layers of normal conductors might be a problem because the ohmic resistance is inversely proportional to the cross section area of the conductor. To prove this statement, a microstrip hybrid ring with a thickness of at least $1\,\mu$m should be fabricated and characterized.
Sapphire as substrate was expected to yield better results due to its smaller loss tangent. From experiments, there are no differences to identify between silicon and sapphire as substrate.
While the MS hybrid rings act almost as expected, the CPW hybrid rings show some non trivial features. The extra dips in the transmission spectra were observed for all

coplanar waveguide hybrid rings expect for the measurement that was performed in Erlangen at the chair in experimental physics of the Friedrich-Alexander-Universität Erlangen-Nürnberg. This measurement shows some non expected response power signal on the ground plane close to the output port. This densities might be linked with the observed peaks in the transmission spectra of the coplanar waveguide hybrid rings. More LTLSM measurements in combination with a theoretical modeling of the response signal might help to explain that property.
Apart from the S-parameter measurements, time domain measurements were performed with two hybrid rings at room temperature. The commercial hybrid ring was bought from MITEQ and because of the relatively thick gold layer of around 2.5 to $3\,\mu$m its properties are still measurable at room temperature. The calculation was realized by using the calculated amplitude A_{cal} to compute the amplitudes $A_{2,\mathrm{cal}}$ and $A_{4,\mathrm{cal}}$ as the constructive and destructive interference of the two signals. The calculations agree well with the measured data.
The same time domain measurement was performed with the MSH Cu sample. Comparing the measured data to the computed values shows a disagreement. This disagreement is unexplained since the measured S-parameters of the copper sample were in agreement with theory.
Despite the problems that are still present, it is possible to design a hybrid ring that meets the requirements for a quantum homodyne measurement scheme of weak signals.

A Quantum Bits and Circuit Quantum Electrodynamics

A.1 Quantum Bit

As mentioned in the introduction, quantum bit or qubit is a quantum mechanical two level system with basis states $|0\rangle$ and $|1\rangle$. Thus, any state $|\Psi(t)\rangle$ of the qubit can be interpreted as a superposition of these two basis states:

$$|\Psi(t)\rangle = \alpha(t)|0\rangle + \beta(t)|1\rangle,$$

where $\alpha(t)$ and $\beta(t)$ are complex amplitudes that have to satisfy the normalization conditions

$$|\alpha(t)|^2 + |\beta(t)|^2 = 1.$$

As shown in figure A.1 the qubit state $|\Psi\rangle$ can be described by a unit vector on the Bloch sphere. With this representation the qubit state can also be expressed by the

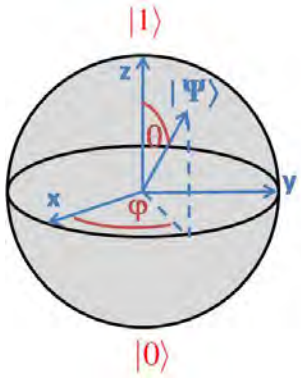

Figure A.1: Representation of the qubit state by a point on the Bloch sphere. The state can be described by the azimuth angle θ and the polar angle ϕ

two angles θ and ϕ by

$$|\Psi(t)\rangle = \sin\left(\frac{\theta}{2}\right) e^{-i\phi/2}|0\rangle + \cos\left(\frac{\theta}{2}\right) e^{i\phi/2}|1\rangle.$$

The qubits that will be used in the future for quantum computing must fulfill a number of criteria, also known as the *Di Vincenzo* criteria [49]. One needs

1. a scalable two-level quantum system

2. the possibility to initialize the qubits in the ground state
3. long decoherence times compared to operation times
4. a universal set of quantum gates
5. the possibility to readout every single qubits

Two extra criteria for the quantum communication are:

6. the feasibility of transforming a stationary qubit into a flying qubit and vice versa
7. the possibility of qubit state transport

As mentioned in the introduction, qubits can be realized with different physical system such as ions in ion traps, cold atoms in optical lattices, quantum dots or superconducting qubits based on Josephson juntions.
The advantage of superconducting qubits over any other solid-state based quantum mechanical two-level system is the possibility to isolate the qubit from the environment and thereby reduce decoherence effectively. This can be done because the superconducting ground state is separated by an energy gap ($\sim$ meV) from the quasiparticle excitation spectrum, see figure A.2.

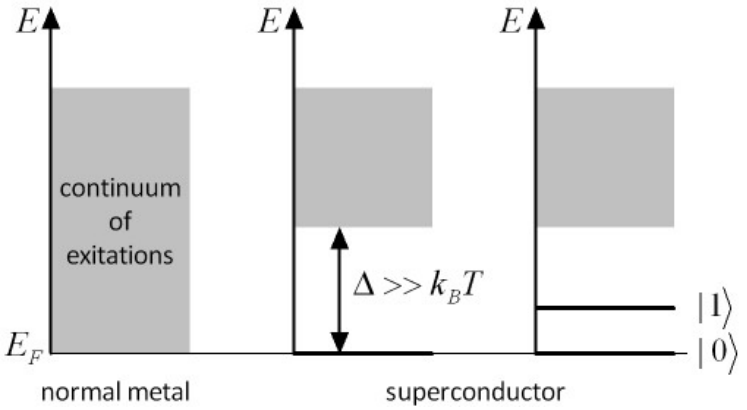

Figure A.2: Advantage of superconductors for constructing solid state based qubits: the Cooper pairs can condense into the same energy level and leave an energy gap Δ above them which inhibits the kind of collision interactions that lead to ordinary resistivity. Such a gap do not exist for normal metals.

The DiVincenzo criteria can be fulfilled by using superconducting qubit systems:

1. In several types of superconducting circuits based on Josephson junctions, elementary manipulations of the quantum state were demonstrated, see [8, 9, 10, 11, 12, 1].

2. At very low temperatures (several mK) the qubit relaxes into a well-defined ground state.

3. In 2005 Ithier et al. [50] presented experiments which characterized the sources of decoherence in a qubit circuit. The experiments of Houck, Schuster et al. [19] and Steffen et al. [51] showed that the decoherence times are long enough to realize the readout of the qubit.

4. An overview of single and two bit gates is given in reference [14] and in 2003 Yamamoto et al. [15] introduced a conditional gate operation using a pair of superconducting charge qubits.

5. Dispersive as well as quantum non-demolition readout schemes for superconducting circuits have been realized [52, 13].

6. A possible transformation of stationary qubits to flying qubits is given by mapping the qubit state onto a photon [19]. This will be explained in section A.4. In 2002, Marcikic et al. [53] created pairs of non-degenerate time-bin entangled photons with ultrashort pump pulses.

7. Each flying qubit can easily be transmitted and therefore be used for qubit transport [19]. A second possibility is to couple different qubits and to map the qubit state from one qubit onto another. This was done in references [54, 55, 56, 57].

   A third variation opens the possibility of coupling of two qubits via a resonator [16] while Helmer et al. [18] proposed a cavity grid which allows to couple any two qubits on the grid independent of their distance and transfer their state.

The superconducting circuits are candidates for implementing qubits.
Depending on the ratio of the characteristic energy scales of the qubits Josephson junctions, the family of superconducting qubits can be divided into: charge qubits, phase qubits and flux qubits (also known as persistent current qubits). In the following, the flux qubit will be described in more detail.

A.2 The Flux Qubit

Flux qubits are micrometer sized superconducting loops interrupted by several Josephson junctions (see figure A.3). The Josephson junctions are characterized by their Josephson coupling energy E_J and their charging energy E_C. Flux qubits differ from other types of superconducting qubits (charge qubit, phase qubit) by the ratio of the coupling energy and the charging energy. Typically in a flux qubit E_J is 10-100 times greater than E_C. It is this ratio that allows the Cooper pairs to flow continuously around the loop which results in a persistent current I_p.
In general, the hamiltonian of the flux qubit is given by

$$H_\mathrm{q} = \frac{1}{2}(\varepsilon\sigma_z + \delta\sigma_x)$$

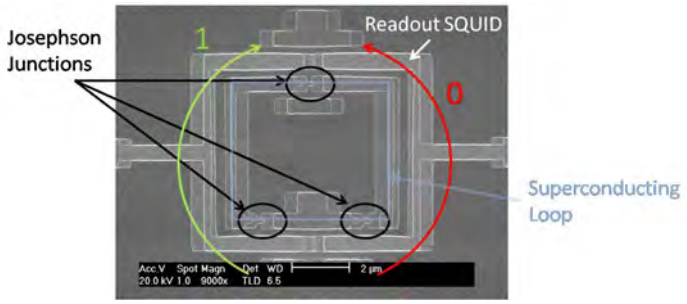

Figure A.3: Scanning electron micrograph of a flux qubit: the inner superconducting ring is interrupted by three Josephson junctions. The classical states correspond to persistent current flowing either clockwise or counter clockwise which represents the basic qubit states $|L\rangle$ and $|R\rangle$.

where σ_x and σ_z are the Pauli spin matrices.
For vanishing tunnel coupling ($\delta = 0$) the two qubit states correspond to the classical states $|L\rangle$ and $|R\rangle$ with clockwise and counterclockwise persistent currents I_p circulating in the loop. These states are separated by the flux-dependent energy $\varepsilon = 2I_p(\Phi_\mathrm{x} - \Phi_0/2)$, where Φ_x is the applied flux through the loop area and $\Phi_0 = h/(2e)$ is the flux quantum. For finite coupling ($\delta > 0$), one obtains superpositions of $|L\rangle$ and $|R\rangle$ at the degeneracy point ($\Phi_\mathrm{x} \approx \Phi_0/2$) (see figure A.4). This re-

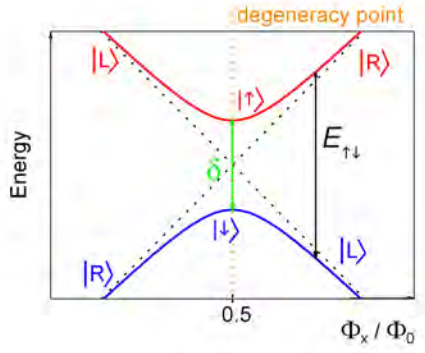

Figure A.4: Energy level diagram of a flux qubit for finite coupling ($\delta > 0$). At the degeneracy point, the two energy states $|L\rangle$ and $|R\rangle$ superimpose to a symmetrical ($|\uparrow\rangle = \sqrt{1/2}(|L\rangle + |R\rangle)$) and an antisymmetrical state ($|\downarrow\rangle = \sqrt{1/2}(|L\rangle - |R\rangle)$). With $\Phi_\mathrm{x} = \Phi_0/2$ the energy gap corresponds to δ.

sults in new qubit eigenstates $|\downarrow\rangle$ and $|\uparrow\rangle$ with the energy difference $E_{\uparrow\downarrow} = \sqrt{\varepsilon^2 + \delta^2}$. At the degeneracy point the energy gap $E_{\uparrow\downarrow}$ corresponds to δ which is independent of Φ_x. This independence of the flux leads to an independence of the flux noise which is the reason of dephasing. Thus, the qubit is protected from dephasing, at the degeneracy point. Therefore, this point represents the optimal point for the coherent manipulation of the qubit. The qubit eigenstates at the degeneracy point

are equal superpositions of $|L\rangle$ and $|R\rangle$, i.e., the expectation value of the persistent current vanishes. Far away from the degeneracy point ($\varepsilon \gg \delta$) the qubit behaves as a classical two-level system.
The main advantage of flux qubits over other types of superconducting qubits is that they are less susceptible to fluctuating charges on the substrate. However they are sensitive to flux noise. This sensitivity has been analyzed in details as references [13, 58, 59] show.

A.3 Circuit Quantum Electrodynamics

In quantum optics isolated Rydberg atoms with electrical dipole moment d are coupled to the vacuum state electric field E_0 of a cavity. When the Rabi frequency $\nu_{\text{Rabi}} = 2dE_0/h$ exceeds the rates of relaxation and decoherence of both the atom and the field, the coherent oscillations of a single excitation between the atom and the cavity can be observed at ν_{Rabi}.
In 2004, A. Wallraff et al. [1] observed the coherent exchange of a microwave single photon between a superconducting charge qubit strongly coupled to an on-chip microwave cavity. This initiated the field of circuit quantum electrodynamics (c-QED). The coherent exchange of energy between the qubit and the cavity can be observed if the relaxation rates γ of the qubit and κ of the cavity are smaller than the coupling constant g of the qubit to the cavity (strong coupling criterion). The resulting entangled states can be detected spectroscopically.
M. Mariantoni et al. [20] and T. Lindström et al. [60] proposed to couple a superconducting flux qubit to an on-chip microwave cavity (see figure A.5), which is basically a resonator with a capacitor at each end (see figure A.7). The capacitors act as mirrors for microwaves where a standing wave is established between the mirrors. The main source of dissipation is the loss of photons from the resonator through the capacities at a rate κ (see figure A.6). The difference between the coupling of a charge qubit to a resonator and a flux qubit to a resonator is, apart from the qubits, the field that couples to the qubit. The charge qubits couple to the electric field and the flux qubits couple to the magnetic field.
The superconducting resonator can be modeled as a harmonic oscillator with the hamiltonian

$$H_{\text{r}} = \hbar\omega_{\text{r}} \left(a^\dagger a + 1/2 \right)$$

where $\langle a^\dagger a \rangle = \langle \hat{n} \rangle = n$ is the average photon number inside the resonator and ω_{r} the resonance frequency. The eigenstates of the resonator described by the hamiltonian are Fock states $|0\rangle ... |n\rangle$ with n photons.
The coupled qubit-resonator system is described by the Jaynes-Cumming hamiltonian:

$$H_{\text{JC}} = H_{\text{r}} + H_{\text{q}} + H_{\text{g}}$$

where H_{g} is the hamiltonian describing the interaction between the qubit and the cavity. One has to differentiate between two regimes: the *resonant* regime with

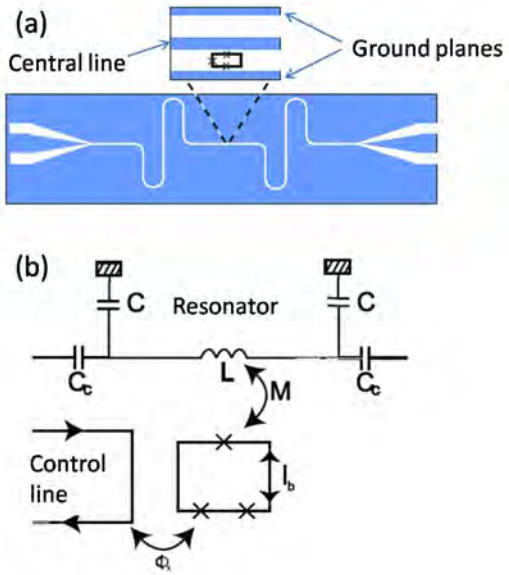

Figure A.5: (a) Sketch of a coplanar waveguide resonator. The qubit can be placed in the gab between the center conductor and the lateral ground plane. (b) Schematic diagram of a superconducting qubit coupled to a resonator. M is the mutual inductance between the resonator and the persistent current qubit that is permeated by the magnetic flux Φ_x. [60]

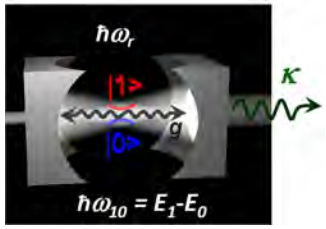

Figure A.6: The capacitors of the resonator that are used in c-QED acts like mirrors. The microwave is trapped in that cavity but can dissipate through the capacities at the rate κ.

$\omega_0 = \omega_r$ and the *dispersive* regime with $|\Delta| = |\omega_0 - \omega_r| \gg 0$.
Figure A.8 gives an overview of the energy levels of the coupled qubit-cavity system. Starting on the left of the diagram, the qubit and the resonator are far detuned ($|\Delta| \gg 0$). The qubit state influences the transmission spectrum of the resonator which leads to a shift of g^2/Δ in the resonance frequency of the resonator. The eigenstates of the coupled system are: $|0,\downarrow\rangle$, $|0,\uparrow\rangle$, $|1,\downarrow\rangle$ and $|1,\uparrow\rangle$. The shift in the resonance frequency of the resonator depends on the qubit state (see figure A.9). Thus, the dispersive regime is favorable for quantum non-demolition measurements of the qubit state.
When varying the external flux, the transition frequency of the qubit can be brought

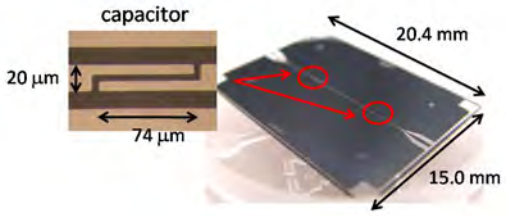

Figure A.7: Design of a line resonator with a capacitor at each end

into resonance with the resonance frequency of the resonator. At this point the interaction between the electromagnetic field inside the cavity and the qubit is described by a dipole interaction

$$H_{\mathrm{g}} = \hbar g(a^{\dagger}\sigma^{-} + a\sigma^{+}),$$

where $\sigma^{+}(\sigma^{-})$ is the raising (lowering) operator for the qubit. In this regime, the resonator and the qubit cannot be understood as two separated systems with their own energy levels. An analogue are two hydrogen-atoms: while they are separated they have the same energy levels but the coupled system is called hydrogen-molecule where each of the origin energy levels is split into two components.
H_{g} couples the states $|0,\uparrow\rangle$ and $|1,\downarrow\rangle$ and lifts their degeneracy (see figure A.8). The oscillations between $|0,\uparrow\rangle$ and $|1,\downarrow\rangle$ can be observed at the Rabi frequency $\nu_{\mathrm{Rabi}} = g/\pi$. One can visualize this as a cycle in which the resonator and the qubit continuously exchange an amount of energy equal to one photon. This proposed scheme allows the generating of single microwave photons without initialization the qubit in the exited state $|1\rangle$.

A.4 Single Microwave Photon Source

In 2007, Houck, Schuster et al. [19] demonstrated an on-chip single-photon source by using the coupling of a qubit with a cavity. The qubit state is mapped onto the photon which acts as a flying qubit and transmits the quantum information across the chip. For this experiment they used a resonator as cavity with two different capacitors at the ends. One capacitor is used as input capacitor and the other, larger one is used as output capacitor as figure A.10 shows. This allows an efficient collection of light emitted from the cavity. The qubit is located on one side of the resonator.
To verify the single-photon output there are three unique characteristics to consider: First, the output is expected to be oscillatory in the amplitude of the control pulse, which is applied to rotate the qubit. Second, the produced mean amplitude should agree well with the expected value for a single photon. Third, the state tomography measured for the photons should show complete agreement with the one obtained from independent measurements of the qubit if the output of the system depends

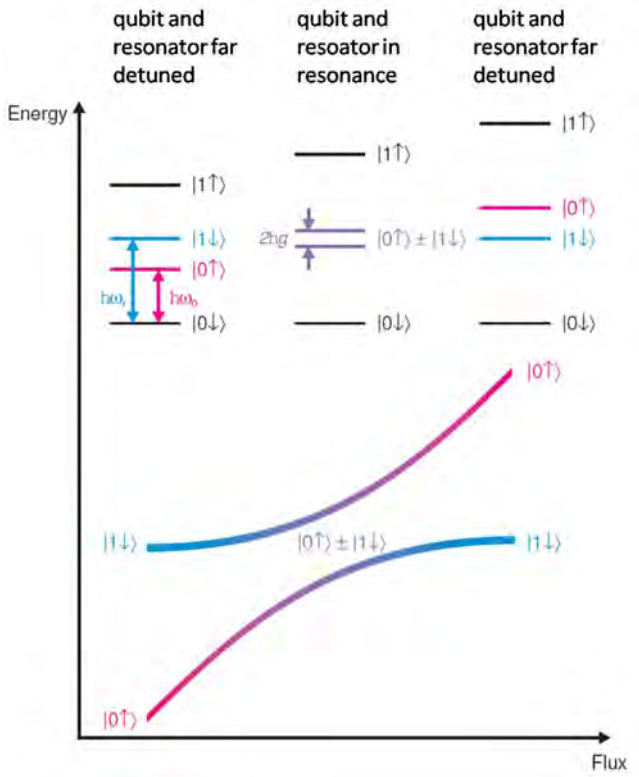

Figure A.8: Energy levels of the coupled qubit-cavity system. On the left and the right of the diagram the qubit is far detuned from the resonator. In the middle, the magnetic flux threading the qubit loop is increased, tuning the qubit transition frequency into resonance with the cavity.[60]

only on the state of the qubit. These three characteristics are all met by the source as the following paragraphs will show.

A gaussian control pulse rotates the qubit state by the Rabi angle that is proportional to the pulse amplitude. This can be visualized by rotating the vector on the bloch sphere (figure A.1) by the angle θ. The excited qubit will then relax while generating a new photon state at the qubit frequency. The control pulse leaves the cavity at a rate that is much faster than the rate of spontaneous emission. Thus, the control pulse and the measurement signal can be separated in time, see figure A.11. As seen in this figure the measured control signal increases linearly while the spontaneous emission oscillates as the qubit is rotated from the ground to the exited state and back. This confirms the spontaneous emission being proportional to the qubit state.

In figure A.12(a) the photon number output of the cavity $\langle a^\dagger a \rangle$ detected with a diode is compared to the measured qubit state $\langle \sigma_z \rangle$. The agreement between qubit and photon states verifies that the photon generation occurs as expected. A second comparison between the integrated voltage of the output photons $i\langle a^\dagger - a \rangle$ and the qubit state $\langle \sigma_y \rangle$ underlines this agreement. Thus, the phase of superposition states

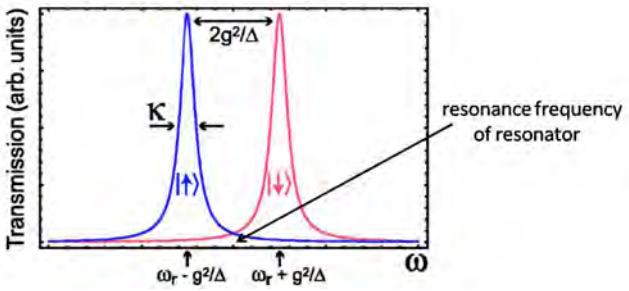

Figure A.9: Transmission spectrum of a qubit-resonator system in the dispersive regime. The resonance frequency of the cavity is shifted by g^2/Δ, depending on the qubit state.[61]

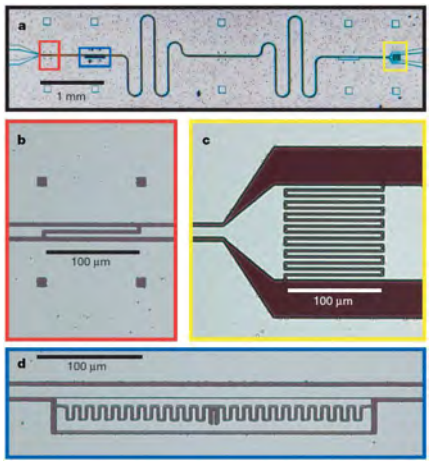

Figure A.10: The circuit quantum electrodynamics device for generating single photons. (a) A transmission line cavity is formed between two capacitors, with the input capacitor shown in (b) (red box in (a)) and the output in (c) (yellow box in (a)). Because the output capacitor is much larger, most radiation leaving the cavity leaves from this port. (d) Transmon Qubit at a voltage anti-node of the cavity (blue box in a). [19]

is also transferred from the qubit to the photon.
The third characteristic is proven by comparing the results of state tomography measurements for the photons to that of the qubit. Figure A.13 shows the excellent agreement of the recorded quadratures of the output homodyne voltages (A.13(b), (c)) and the expected σ_x and σ_y components of the qubit state (A.13(e), (f)). The different labeling of the axis is due to the difference of the experiments that were performed. This tomography allows a full characterization of the qubit by looking the spontaneous emission at the output, directly observing a qubit at its Lamor frequency. Additionally, the qubit state at an arbitrary point of the bloch sphere can be transferred onto a photon state and so acts as a "flying" qubit.
This mapping of a qubit state onto photon states allows the use of microwave photons

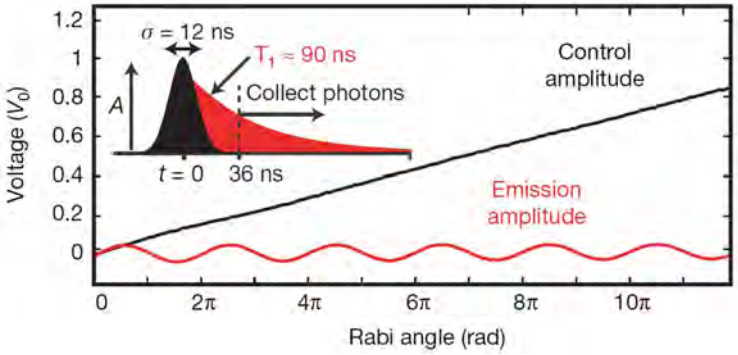

Figure A.11: Measurement drive (at $t = 0\,\text{ns}$) and spontaneous emission voltage (at $t = 36\,\text{ns}$) of cavity output in units of zero-point fluctuations V_0. The inset shows the time sequence, with a gaussian pulse at the qubit frequency and subsequent photon emission with relaxation time T_1. [19]

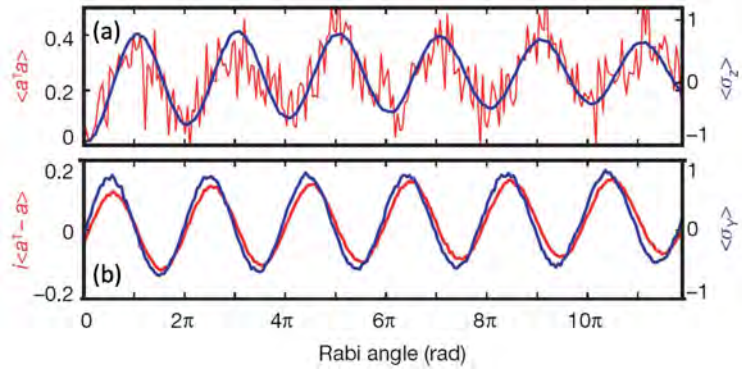

Figure A.12: (a)Photon number output of cavity $\langle a^\dagger a\rangle$ (red line) compared with the measured qubit state $\langle\sigma_z\rangle$. (b) Integrated voltage of the output photons $i\langle a^\dagger - a\rangle$ compared with the qubit state $\langle\sigma_z\rangle$ [19]

as a carrier of quantum information on a chip.

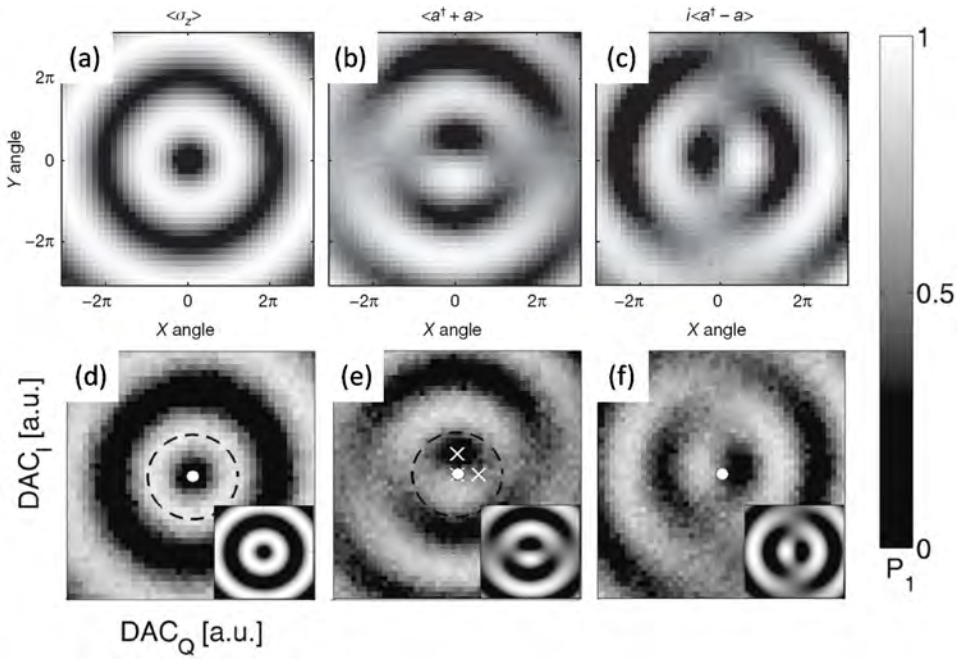

Figure A.13: (a-c) were performed by [19] and (d-f) by [51]: (a,d)Measurement of qubit state $\langle\sigma_z\rangle$ after rotations by pulses of arbitrary amplitudes and phases.(b-c) The amplitudes of the voltage measured in each homodyne quadrature (b) $\langle a^\dagger + a\rangle$ and (c) $i\langle a^\dagger - a\rangle$ agree with (e) and (f), that show the measurements for the qubit corresponding states.

B Fluxoid Quantization in the Hybrid Ring

An important characteristic of superconductivity is the fluxoid quantization. There is a possibility of flux quantization influencing the hybrid ring close to the operating frequency. The total fluxoid penetrating a superconducting loop has to be a multiple of the flux quantum $\Phi_0 = h/(2e)$ which was demonstrated by Doll and Näbauer [62] and Deaver and Fairbank [63] in 1961.

$$\oint_C \Lambda \mathbf{j}_\mathrm{s} \cdot \mathrm{d}\mathbf{l} + \int_S \mathbf{B} \cdot \mathrm{d}\mathbf{s} = n \cdot \Phi_0$$

where S is the surface defined by a closed contour C and $\mathrm{d}\mathbf{l}$ is an infinitesimal length of C. $\mathrm{d}\mathbf{s}$ is normal to S and quantifying an infinitesimal area.
The hybrid ring may be influenced by the following mechanism (see figure B.1): The current $I = I_\mathrm{n} + I_\mathrm{s}$ is split unequally into two components I_L and I_R. This includes the unequal splitting of the supercurrent $I_\mathrm{s,L}$ and $I_\mathrm{s,R}$ such that the total flux $\Phi_\mathrm{s} = n \cdot \Phi_0$ through the ring due to the supercurrent remains constant. Hence the ratio of $I_\mathrm{s,l}$ and $I_\mathrm{s,R}$ should be the inverse ratio of the corresponding distances on the ring between ports one and two. Therefore, to get a maximum isolation[1] between these two ports at the operating frequency, the ratio $I_\mathrm{s,L}/I_\mathrm{s,R}$ should be equal to 1. However, the hybrid ring would be less efficient.

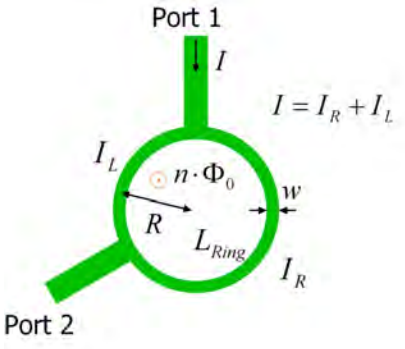

Figure B.1: The hybrid ring modeled as a two port device, consisting of a superconducting ring with width w and radius R. The ring has a self inductance L_ring.

[1] The characteristics of the hybrid ring are explained in 2.3

This is a very simple demonstration of the influencing of the hybrid ring by the fluxoid quantization. Since the wavelength is in order of the ring dimension, namely the circumference is $3\lambda/2$, it is very hard to predict an additional influence of the fluxoid quantization. A complete theoretical calculation around the working frequency of the hybrid ring should be based on the general Maxwell's equations together with the fluxoid quantization and should result in a system of inhomogeneous partial differential equations.
The presented measurements of superconducting hybrid rings (MSH Nb Al_2O_3 and MSH Nb Si) and normal conducting hybrid rings (MSH Au and MSH Cu) showed no influence on the hybrid ring by the fluxoid quantization.

C Fringe Field Factor

The fringe field factor is used in chapter 2.2.2. According to reference [35], it can be computed as follows

$$K(w,h,t) = \frac{h}{w}\frac{2}{\pi}\ln\left(\frac{2r_\mathrm{b}}{r_\mathrm{a}}\right)$$

with

$$\ln r_\mathrm{a} = -1 - \frac{\pi w}{2h} - \frac{p+1}{p^{1/2}}\tanh^{-1}\left(p^{-1/2}\right) - \ln\left(\frac{p-1}{4p}\right)$$

$$r_\mathrm{b} = \begin{cases} r_{\mathrm{b}0} & \text{for } w/h \geq 5 \\ r_{\mathrm{b}0} - \sqrt{[(r_{\mathrm{b}0}-1)(r_{\mathrm{b}0}-p)]} + (p+1)\tanh^{-1}\left(\frac{r_{b0}-p}{r_{b0}-1}\right)^{1/2} & \\ \qquad -2p^{1/2}\tanh^{-1}\left(\frac{r_{\mathrm{b}0}-p}{p(r_{\mathrm{b}0}-1)}\right)^{1/2} + \frac{\pi w}{2h}\sqrt{p} & \text{for } 5 > w/h \geq 1 \end{cases}.$$

$$r_{\mathrm{b}0} = \eta + \frac{p+1}{2}\ln\Delta$$

Δ is the larger value of η or p:

$$\eta = \sqrt{p}\left\{\frac{\pi w}{2h} + \frac{p+1}{2\sqrt{p}}\left[1 + \ln\left(\frac{4}{p-1}\right)\right] - 2\tanh^{-1}(\sqrt{p})\right\}$$

$$p = 2\left(1+\frac{t}{h}\right)^2 - 1 + \sqrt{\left[2\left(1+\frac{t}{h}\right)^2 - 1\right]^2 - 1}$$

The fringe field factor is plotted versus the aspect ratio w/h in figure C.1
When the aspect ratio $w/h \to \infty$, the fringe factor will reduce to one.

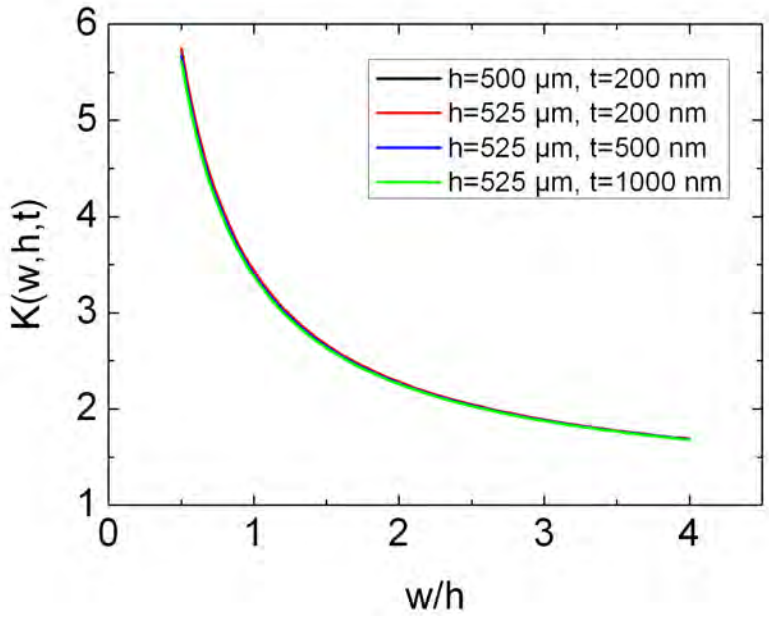

Figure C.1: The fringe factor $K(w, h, t)$ versus w/h for some given values of t and h. The different graphs are more or less identical.

D General Coplanar Waveguide

As shown in figure D.1 a coplanar waveguide consists of a substrate and the conducting line and the ground plane on the same site of the substrate. In general the substrate can consists of more than one layer. Gevorgian et al. [38] showed a way to calculate the effective permittivity and the characteristic impedance for a two layered substrate.

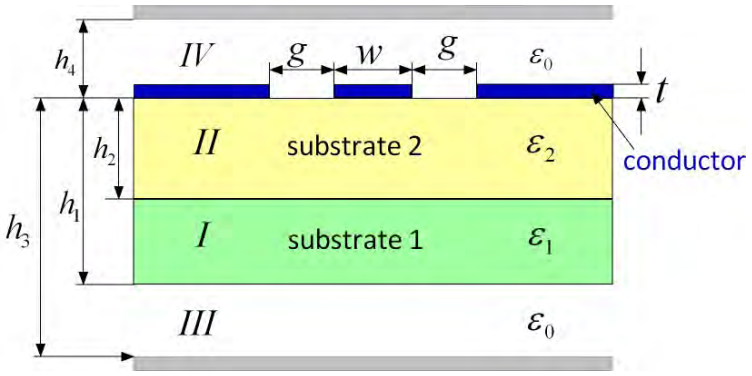

Figure D.1: The profile of a coplanar waveguide transmission line with a double layered substrate.

According to reference [38], the total capacitance C per unit lenght can be interpreted as a connection in parallel of the partial capacitances to a resultant parallel-plate capacitor with $C = C_{04} + C_{03} + C_1 + C_2$. Since regions III and IV are filled with air it is $\varepsilon_3 = \varepsilon_4 = \varepsilon_0$ and

$$C_{0j} = \varepsilon_0 \frac{K(k_j)}{K(k_j')} \qquad (j = 3, 4) \tag{D.1}$$

where the modulus of the complete elliptic integrals $K(k_j)$, $K(k_j')$ are defined by

$$k_j = \frac{\tanh\left(\frac{\pi w}{4h_j}\right)}{\tanh\left(\frac{\pi}{2h_j}\,(w/2+g)\right)}$$

$$k_j' = \sqrt{1-k_j^2}.$$

The capacitances due to the substrate are

$$C_1 = (\varepsilon_1 - 1)\varepsilon_0 \frac{K(k_1)}{K(k_1')} \tag{D.2}$$

with

$$k_1 = \frac{\sinh\left(\frac{\pi w}{4h_1}\right)}{\sinh\left(\frac{\pi}{2h_1}\left(w/2+g\right)\right)}$$

$$k_1' = \sqrt{1-k_1}$$

and

$$C_2 = (\varepsilon_2 - \varepsilon_1)\varepsilon_0 \frac{K(k_2)}{K(k_2')} \tag{D.3}$$

with

$$k_2 = \frac{\sinh\left(\frac{\pi w}{4h_2}\right)}{\sinh\left(\frac{\pi}{2h_2}\left(w/2+g\right)\right)}$$

$$k_2' = \sqrt{1-k_2}\,.$$

Hence the total capacitance can be written as

$$C = (\varepsilon_1 - 1)\varepsilon_0 \frac{K(k_1)}{K(k_1')} + (\varepsilon_2 - \varepsilon_1)\varepsilon_0 \frac{K(k_2)}{K(k_2')} + \varepsilon_0 \left[\frac{K(k_3)}{K(k_3')} + \frac{K(k_4)}{K(k_4')}\right].$$

Inducing the effective permittivity

$$\varepsilon_{\mathrm{eff,q}} = 1 + \frac{K(k_1)}{K(k_1')}\left[\frac{K(k_3)}{K(k_3')} + \frac{K(k_4)}{K(k_4')}\right](\varepsilon_1 - 1) + \frac{K(k_2)}{K(k_2')}\left[\frac{K(k_3)}{K(k_3')} + \frac{K(k_4)}{K(k_4')}\right](\varepsilon_2 - \varepsilon_1) \tag{D.4}$$

the capacitance is

$$C = 2\varepsilon_0 \varepsilon_{\mathrm{eff,q}} \left[\frac{K(k_3)}{K(k_3')} + \frac{K(k_4)}{K(k_4')}\right]. \tag{D.5}$$

By using equation(2.23) the characteristic impedance is

$$Z_0 = \frac{60\pi}{\sqrt{\varepsilon_{\mathrm{eff,q}}}} \left[\frac{K(k_3)}{K(k_3')} + \frac{K(k_4)}{K(k_4')}\right]^{-1}. \tag{D.6}$$

E Fabrication Parameters

Within this work different fabrication processes were used depending on the different conducting materials. Figures E.1-E.4 show schematically the processes for the different samples while the detailed parameters are given in tables E.2-E.4. Table E.1 lists those parameters that all processes have in common.

process step	process parameters
cleaning the sample	C1: cleaning in an ultrasonic bath with 1st acetone (p.a.), 2nd acetone (p.a.), 3rd isopropanol (p.a.) (each 2 min @ 20° C, power 2 or 1) C2: boiling the sample in acetone (10 min), step C1
cleaning the quartz mask	clean with 1st acetone (p.a.), 2nd acetone (p.a.), 3rd isopropanol (p.a.) dry with N_2

Table E.1: details of fabrication steps that are used in every process

Niobium on Silicon or Sapphire

The fabrication steps for niobium on sapphire or silicon are shown in figure E.1. The parameters of the single steps are given in table E.2.

A niobium hybrid ring with a thin (200 nm) gold layer on the contacts was also fabricated. This hybrid ring was necessary because niobium is very difficult to solder. The thickness of the niobium line was also 200 nm like the gold layer. The fabrication steps are shown in figure E.2

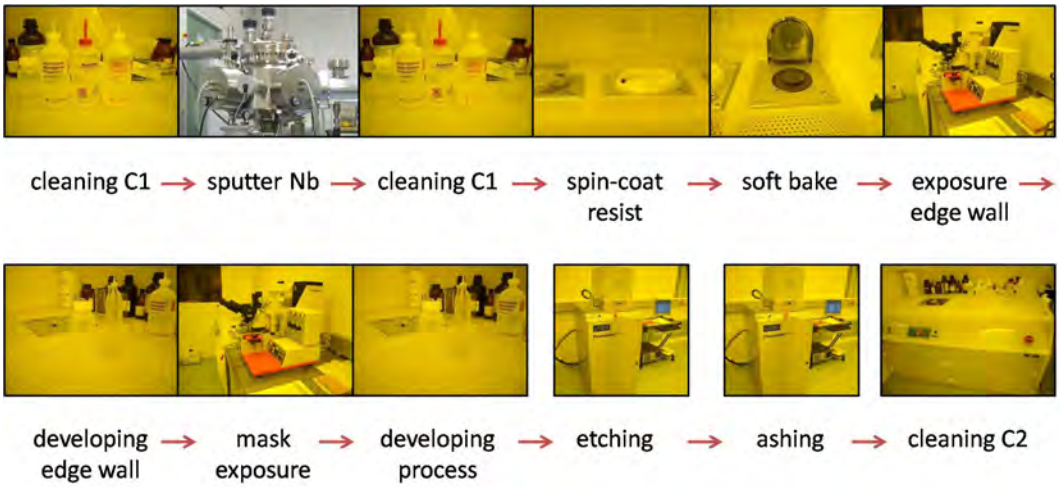

Figure E.1: Overview of the fabrication process for niobium on silicon or sapphire

process step	process parameters
sputtering niobium	process pressure: $2.7 \cdot 10^{-3}$ mbar power 200 W Ar flow rate: 10 sccm/min duration: 60 s presputtering, 600 s for 200 nm, 1500 s for 500 nm, 3000 s for 1 μm thickness
evaporating gold	process voltage: 8.5 kV temperature: room temperature purity of gold: 5N rate: 5 Å/s emission current: 68 mA filament current: 28-29 A process pressure: $4.1 \cdot 10^{-7}$ mbar duration: 6:40 min for 200 nm
spin-coat the resist	resist: AZ© 5214E image reversal photoresist spin speed 4000 rpm @ 3 s, 8000 rpm @ 1 min
hot plates	soft bake: 110° C @ 70 s

process step	process parameters
exposure	mask aligner (MJB3, Karl Süss GmbH) exposure of edge wall: 15 s mask exposure: 4 s
developing	developer: AZ© developer 20 ml stirred with 20 ml H_2O developing of edge wall: 1 min developing process: 2 min
etching (chemical) gold	$KI - I_2$ (25° C @ ca. 20 s)
etching (physical) niobium	Reactive Ion Etching (RIE) (Plasmalab 80 Plus, Oxford Instruments Inc.) argon flow rate: 10 sccm/min SF_6 flow rate: 20 sccm/min APC controller: set pressure: 15 mTorr, set position: 0, strike pressure: 30 mTorr, ramp rate: 5 mTorr/s ICP forward power: 50 W RF forward power: 100 W duration: 2:10 min - 3 min
ashing	Reactive Ion Etching (RIE) (Plasmalab 80 Plus, Oxford Instruments Inc.) O_2 flow rate: 50 sccm/min APC controller: set pressure: 5 mTorr, set position: 0, strike pressure: 50 mTorr, ramp rate: 0 mTorr/s ICP forward power: 0 W RF forward power: 100 W duration: 2:30 min - 3 min

Table E.2: details of fabrication process for niobium on sapphire or silicon

Gold on Silicon

MSH Au consists of a 200 nm thick gold line on a 525 μm thick silicon substrate that has no oxide layer. The fabrication procedure is show in figure E.3 and the details are listed is E.3.

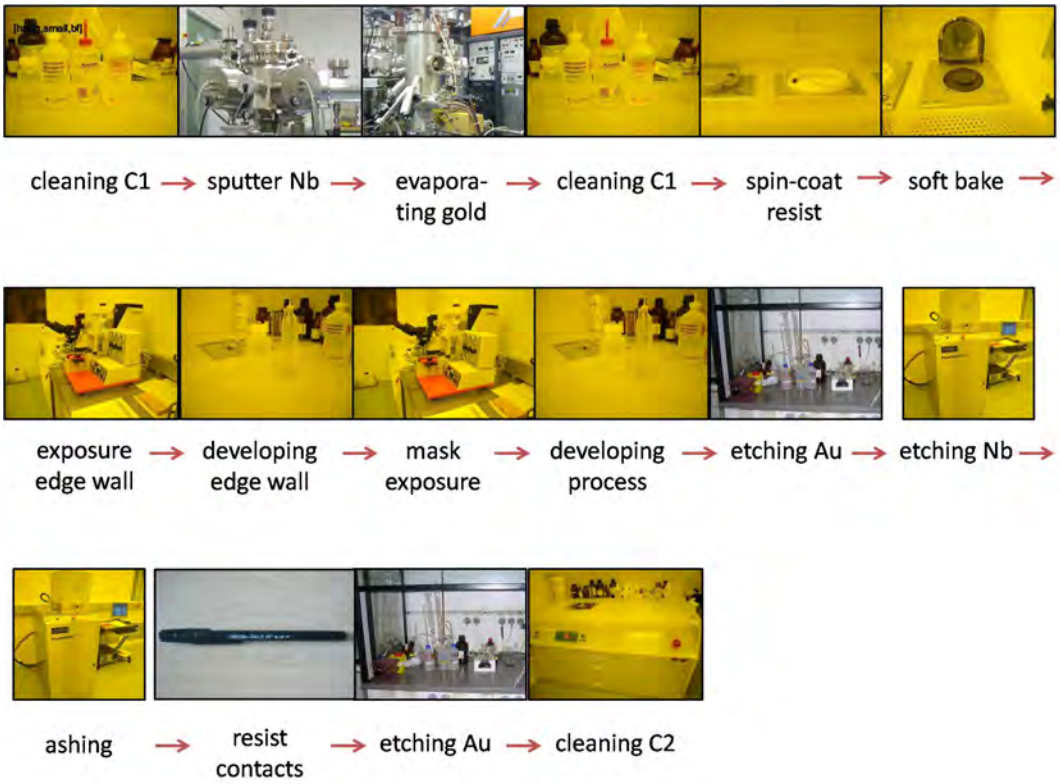

Figure E.2: Overview of the fabrication process for niobium on silicon with a gold layer for soldering

process step	process parameters
sputtering chromium	Med 020 Choating System, Bal-Tec Ag process pressure: $5 \cdot 10^{-2}$ mbar current: 120 mA duration: 18 s for 3 nm, thickness
sputtering gold	Med 020 Choating System, Bal-Tec Ag process pressure: $5 \cdot 10^{-2}$ mbar current: 45 mA duration: 291 s for 200 nm, thickness
spin-coat the resist	resist: AZ© image reversal photoresist spin speed 4000 rpm @ 3 s, 8000 rpm @ 1 min

process step	process parameters
hot plates	soft bake: 110° C @ 70 s
exposure	mask aligner (MJB3, Karl Süss GmbH) exposure of edge wall: 15 s mask exposure: 4 s
developing	developer: AZ© developer 20 ml stirred with 20 ml H_2O developing of edge wall: 1 min developing process: 2 min
etching (physical)	Ion Etching process pressure: $4.2 \cdot 10^{-5}$ mbar E_{Ar}: 500 eV cathode filament current: 4.56 A discharge current: 0.25 A, discharge voltage: 53,6 V beam current: 12 mA, beam voltage: 500 V accelerator current: 0 mA, accelerator voltage: 350 V neutralizer emission current: 15 mA filament current: 4.5 A duration: 10 min
ashing	Reactive Ion Etching (RIE) (Plasmalab 80 Plus, Oxford Instruments Inc.) O_2 flow rate: 50 sccm/min APC controller: set pressure: 5 mTorr, set position: 0, strike pressure: 50 mTorr, ramp rate: 0 mTorr/s ICP forward power: 0 W RF forward power: 100 W duration: 10 s

Table E.3: details of fabrication process for gold on silicon

Copper on PTFE/Ceramic

MSH Cu is made out of RO3010 substrate of Rogers Corporation. This substrate has 17.5 μm copper layers on each side. Thus, sputtering is unnecessary. The optical

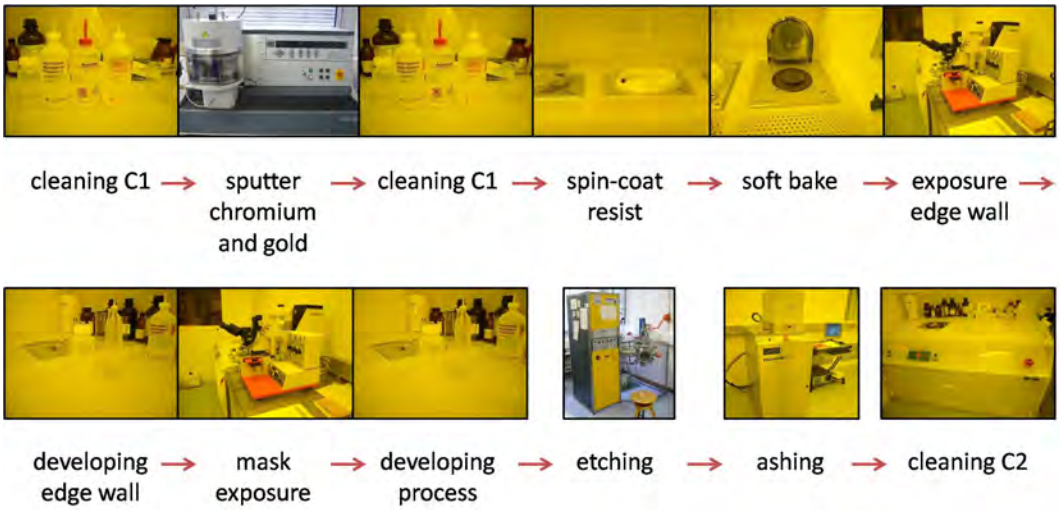

Figure E.3: Overview of the fabrication process for gold on silicon

lithography process is basically the same as for the other samples but with other timescales. Therefore removing the edge wall can be left out. The other fabrication processes include dry etching whereas the MSH Cu sample is etched in $KI - I_2$ dilution.

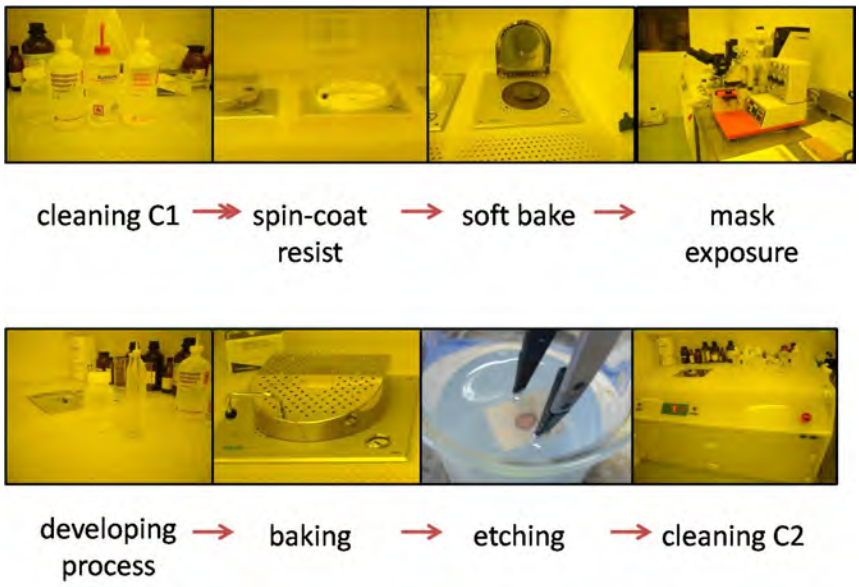

Figure E.4: Overview of the fabrication process of the copper on PTFE/ceramic sample

process step	process parameters
spin-coat the resist	resist: AZ© image reversal photoresist spin speed 4000 rpm @ 3 s, 8000 rpm @ 1 min
hot plates	soft bake: 110° C @ 70 s backing: 140° C @10 min, controlled cooling till 70° C within 1 h
exposure	mask aligner (MJB3, Karl Süss GmbH) duration: 19 s
developing	developer: AZ© developer 20 ml stirred with 20 ml H_2O duration: 45 s
etching (chemical)	$Na_2S_2O_8$ 100 g : 0.5 l H_2O (45° C @ ca. 7 min)

Table E.4: details of fabrication process for copper on teflon/ceramic

F Technical Drawings

The drawings in F.1 and F.2 show the box and the box cover for the hybrid rings. It was machined in the WMI workshop. The technical drawing of the sample box for the H 3 hybrid ring can be found in [24]. The tolerances given are already at the limit of what can be produced. As the achievable accuracy of the substrate dimensions is below the accuracy of the sample holder, the dimensions of the sample holder have been adapted to those of the substrate.

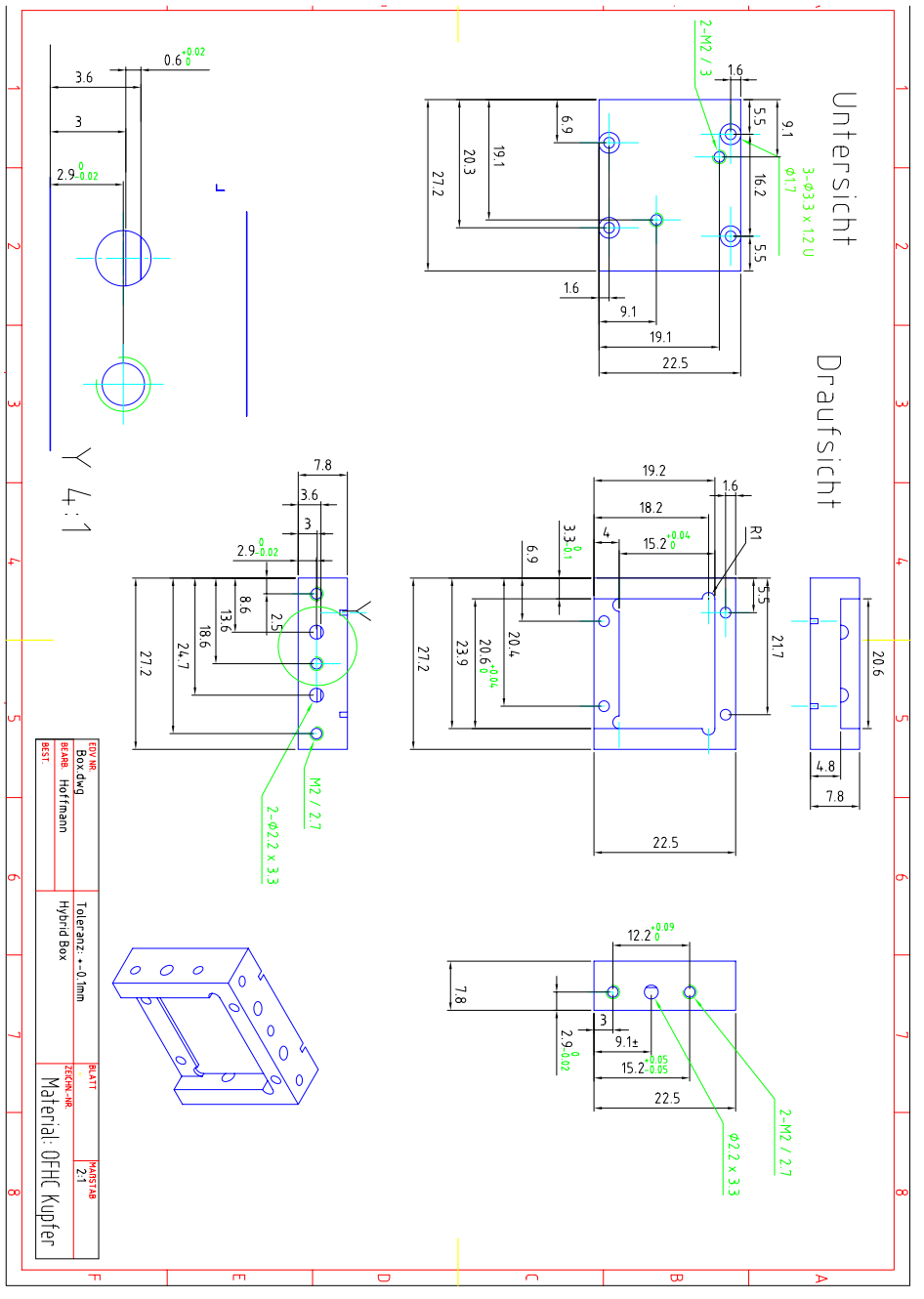

Figure F.1: Technical drawing of the measurement box. Dimensions are given in mm

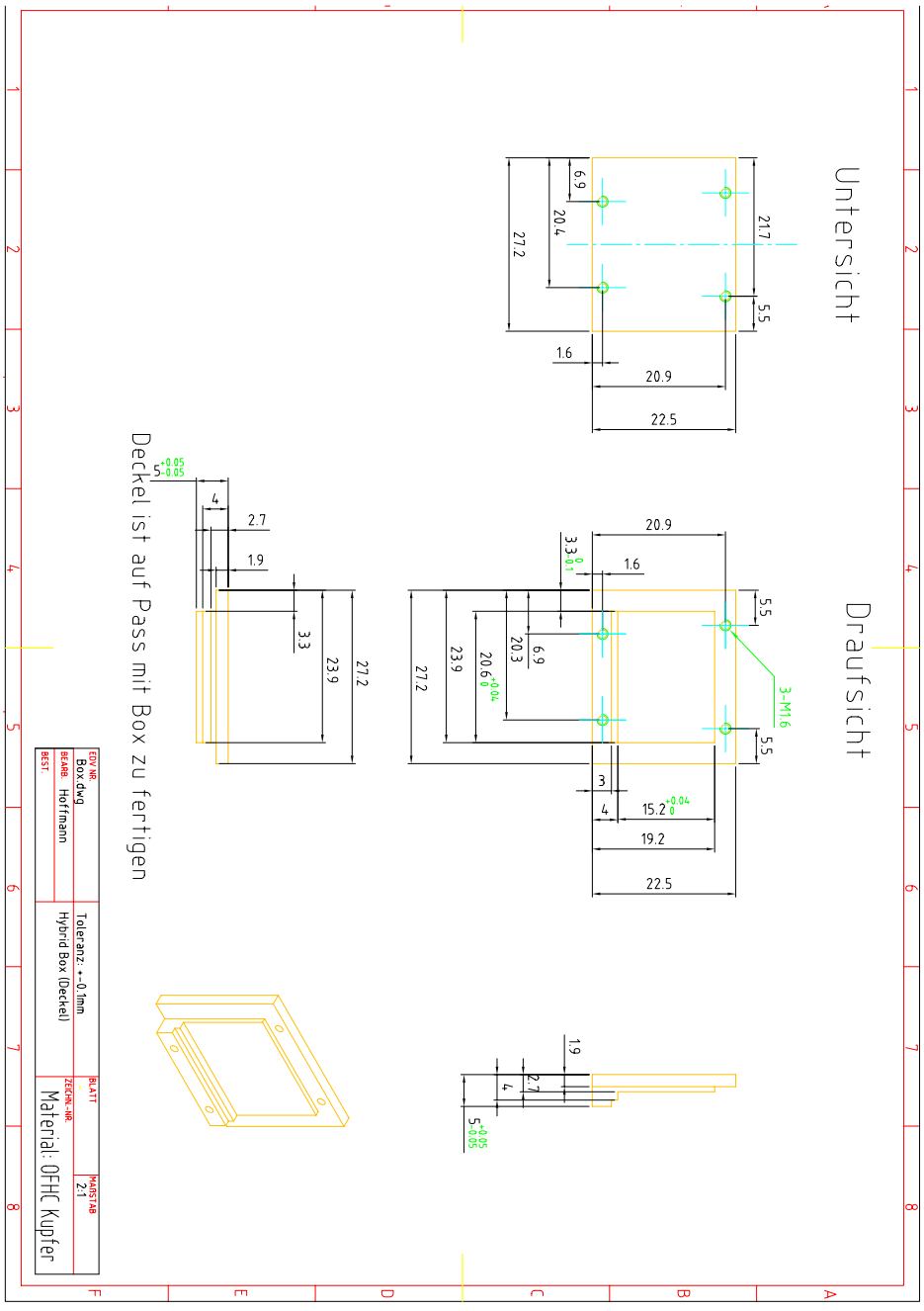

Figure F.2: Technical drawing of the box cover. Dimensions are give in mm

Bibliography

[1] A. Wallraff, D.I. Schuster, A. Blais, L. Frunzio, R.-S. Huang, J. Majer, S. Kumar, S.M. Girvin, and R.J. Schoelkopf. Strong coupling of a single photon to a superconducting qubit using circuit quantum electrodynamics. *Nature*, **431**:162, (2004).

[2] M. Mariantoni, M.J. Storcz, F.K. Wilhelm, W.D. Oliver, A. Emmert, A. Marx, R. Gross, H. Christ, and E. Solano. On-chip Microwave Fock States and Quantum Homodyne Measurements. *submitted to Eur. Phys. Lett., cond-mat/0509737v2*, (2005).

[3] R.P. Feynman. Simulating Physics with Computers. *Int. J. Theor. Phys.*

[4] H. Haeffner, W. Haensel, C. F. Roos, J. Benhelm, D. Chek al kar, M. Chwalla, T. Koerber, U. D. Rapol, M. Riebe, P. O. Schmidt, C. Becher, O. Guehne, W. Duer, and R. Blatt. Scalar multiparticle entanglement of trapped ions. *Nature*, **438**:643, (2005).

[5] Isaac L. Chuang, Lieven M. K. Vandersypen, Xinlan Zhou, Debbie W. Leung, and Seth Lloyd. Experimental realization of a quantumalgorithm. *Nature*, **393**:143, (1998).

[6] Peter W. Shor. Polynomial-time algorithms for prime factorization and discrete logarithms on a quantum computer. (1996). arXiv:quant-ph/9508027.

[7] M.H. Devoret, A. Wallraff, and J.M. Martinis. Superconducting qubits: A short review. arXiv:cond-mat/0411174, (2004).

[8] Y. Nakamura, Yu.A. Pashkin, and J.S. Tsai. Coherent control of macroscopic quantum states in a single-cooper-pair box. *Nature*, **398**:786, (1999).

[9] D. Vion, A. Aassime, A. Cottet, P. Joyez, H. Pothier, C. Urbina, D. Esteve, and M.H. Devoret. Manipulating the quantum state of an electrical circuit. *Science*, **296**:886, (2002).

[10] J.M. Martinis, S. Nam, J. Aumentado, and C. Urbina. Rabi oscillations in a large josephson-junction qubit. *Phys. Rev. Lett.*, **89**:117901, (2002).

[11] I. Chiorescu, Y. Nakamura, C.J.P.M. Harmans, and J.E. Mooij. Coherent quantum dynamics of a superconducting flux-qubit. *Science*, **299**:1869, (2003).

[12] J. Claudon, F. Balestro, F. W. J. Hekking, and O. Buisson. Coherent oscillations in a superconducting multilevel quantum system. *Phys. Rev. Lett.*, **93**:187003, (2004).

[13] F. Deppe, M. Mariantoni, E. P. Menzel, S. Saito, K. Kakuyanagi, H. Tanaka, T. Meno, K. Semba, H. Takayanagi, , and R. Gross. Phase-coherent dynamics of a superconducting flux qubit with capacitive-bias readout. *cond-math.supr-con/0710.4455v1*, (2007).

[14] R. Gross and A. Marx. *Applied Superconductivity: Josephson Effect and Superconducting Electronics*. http://www.wmi.badw-muenchen.de/teaching/Lecturenotes/index.html, (Walther-Meissner-Institut, Garching b. München), (2008).

[15] T. Yamamoto, Yu.A. Pashkin, O. Astafiev, Y. Nakamura, and J.S. Tsai. Demonstration of conditional gate operation using superconducting charge qubits. *Nature*, **425**:941, (2003).

[16] Mika A. Sillanpää, Jae I. Park, and Raymond W. Simmonds. Coherent quantum stste storage and transfer between two phase qubits via a resonator cavity. *Nature*, **449**:438, (2007).

[17] J. Majer, J. M. Chow, J. M. Gambetta, Jens Koch, B. R. Johnson, J. A. Schreier, L. Frunzio, D. I. Schuster, A. A. Houck, A. Wallraff1and A. Blais, M. H. Devoret, S. M. Girvin, and R. J. Schoelkopf. Coupling superconducting qubits via a cavity bus. *Nature*, **449**:443, (2007).

[18] F. Helmer, M. Mariantoni, A. G. Fowler, J. v. Delft, E. Solano, and F. Marquardt. Two-dimensional cavity grid for scalable quantum computation with superconducting circuits. (2007). arXiv:cond-math.mes-hall/0706.3625v.

[19] A. A. Houck, D. I. Schuster, J. M. Gambetta, J. A. Schreier, B. R. Johnson, J. M. Chow, L. Frunzio, J, Majer, M. H. Devoret, S. M. Girvin, and R. J. Schoelkopf. Generating single microwave photons in a circuit. *Nature*, **449**:328, (2007).

[20] M. Mariantoni, M.J. Storcz, F.K. Wilhelm, W.D. Oliver, A. Emmert, A. Marx, R. Gross, H. Christ, and E. Solano. Generation of Microwave Single Photons and Homodyne Tomography on a Chip. *submitted to Eur. Phys. Lett., cond-mat/0509737*, (2007).

[21] D. M. Pozar. *Microwave Engineering, Third Edition*. John Wiley & Sons, Inc., (New York), (2005).

[22] Sung-Chan Kim ans Baek-Seok Ko, Tae-Jong Baek, Byeong-Ok Lim, Dan An, Dong-Hoon Shin, Member, and Jin-Koo Rhee. Hybrid ring coupler forw-band mmic applications using mems technology. *IEEE Microw. and Wireless Comp. Lett.*, **15**:652, (2005).

[23] B.S. Ko, T.J. Baek, D.H. Shin, S.C. Kim, B.O. Lim, H.S. Lee, S.K. Kim, H.C. Park, Y.H. Chun, and J.K. Rhee. Design and fabrication of 180° hybrid ring coupler for applications of mmics using dielectric-supported air-gapped microstriplines. *Electronic Letters*, **40**(11), (2004).

[24] A. Emmert. Circuit-quantum electrodynamics (CQED) with superconducting flux qubits. Master's thesis, Technische Universität München, (2006). Diploma Thesis.

[25] F. London and H. London. The electromagnetic equations of the supraconductor. *Proc. R. Soc. London A*, **149**(**866**), (1935).

[26] V.L. Ginzburg and L.D. Landau. *Zh. Eksp. Teor. Fiz.*, **20**:1064, (1950).

[27] J. Bardeen, L. N. Cooper, and J. R. Schrieffer. Theory of superconductivity. *Physical Review*, **108**:1175, (1957).

[28] P. Mueller and A. V. Ustinov. *The Physics of Superconductivity*. Springer-Verlag Berlin Heidelberg, (1997).

[29] Charles Kittel. *Einführung in die Festkörperphysik*. Oldenbourg, (1983).

[30] R. E. Collin. *Foundations for Microwave Engineering, Second Edition*. Wiley-IEEE Press, (New Jersey), (2000).

[31] M. Kirschning and R. H. Jansen. Accurate model for effective dielectric constant of microstrip with validity up to millimeter-wave frequencies. *Electron. Lett.*, **18**:272, (1982).

[32] T. C. Edwards and R. P. Owens. 2-18-ghz dispersion measurements on 10-100-ω microstrip lines on sapphire. *IEEE Trans. Microw. Theory Tech.*, **24**:506, (1976).

[33] M. Kobayashi. A dispersion formula satisfying recent requirements in microstrip CAD. *IEEE Trans. Microw. Theory Tech.*, **36**:1246, (1988).

[34] M. Kobayashi and F. Ando. Dispersion characteristics of open microstrip lines. *IEEE Trans. Microw. Theory Tech.*, **35**:101, (1987).

[35] W.H. Chang. The inductance of a superconducting strip transmission line. *J. Appl. Phys.*, **50**:8129, (1979).

[36] Cheng P. Wen. Coplanar Waveguide: A surface strip transmission line suitable for nonreciprocal gyromagnetic device applications. *IEEE*, **17**:1087, (1969).

[37] R. N. Simons. *Coplanar Waveguide Circuits, Components, and Systems*. John Wiley & Sons, (New York), (2001).

[38] Spartak Gevorgian, L.J. Linnér, and Erik L. Kollberg. CAD Models for shielded Multilayered CPW. *IEEE Trans. Microw. Theory Tech.*, **43**:772, (1995).

[39] G. Hasnain, A. Dienes, and J. R. Whinnery. Dispersion of picosecond pulses in coplanar transmission lines. *IEEE Trans. Microw. Theory Tech.*, **34**:738, (1986).

[40] Eikichi Yamashita, Kazuhiko Atsuki, and Tomio Ueda. An Approximate Dispersion Formula of Microstip Lines for Computer-Aided Design of Microwaves Integrated Circuits. *IEEE Trans. Microw. Theory Tech.*, **27**:1036, (1979).

[41] W. Rauch, E. Gornik, G. Solkner, A. A. Valenzuela, F. Fox, and H. Behner. Microwave properties of $YBa_2Cu_30_{7-x}$ thin films studied with coplanar transmission line resonators. *J. Appl. Phys.*, **73**:1866, (1993).

[42] B. R. Heimer, L. Fan, and K. Chang. Uniplaner hybrid couplers using asymmetrical coplanar striplines. *IEEE Trans. Microw. Theory Tech.*, **45**:2234, (1997).

[43] Company H.-P. Understanding the fundamental principles of vector network analysis. *Hewlett-Packard Application Note*, **1287-1**, (1999).

[44] Company H.-P. Exploring the architectures of network analyzers. *Hewlett-Packard Application Note*, **1287-2**, (1999).

[45] J.D. Jackson. *Classical electrodynamics*. John Wiley & Sons, Inc., (New York, N.Y.), (1999), 3rd ed.

[46] John G. Hartnett, Michael E. Tobar, Eugene N. Ivanov, and Jerzy Krupka. Room temperature measurement of the anisotropic loss tangent of sapphire using the whispering gallery mode technique. *IEEE, transactions on ultrasonics, ferroelectrics, and frequency control*, **53**(1), (2006).

[47] Peter Haring Bolivar, Martin Brucherseifer, Jaime Gómez Rivas, Ramón Gonzalo, Iñigo Ederra, Andrew L. Reynolds, M. Holker, and Peter de Maagt. Measurement of the dielectric constant and loss tangent of high dielectric-constant materials at terahertz frequencies. *IEEE Trans. Microw. Theory Tech.*, **51**(4), (2003).

[48] Robert E. Collin. *Foundations for Microwave Engeneering*. John Wiley & Sons, Inc., (New Jersey), (2001), 2nd ed.

[49] David. P. Divincenzo. Quantum computation. *Science*, **270**:255, (1995).

[50] G. Ithier, E. Collin, P. Joyez, P. J. Meeson, D. Vion, D. Esteve, F. Chiarello, A. Shnirman, Y. Makhlin, J. Schriefl, and G. Schön. Decoherence in a superconducting quantum bit circuit. *Phys. Rev. B*, **72**:134519, (2005).

[51] Matthias Steffen, M. Ansmann, R. McDermott, N. Katz, Radoslaw C. Bialczak, Erik Lucero, Matthew Neeley, E. M. Weig, A. N. Cleland, , and John M. Martinis. State tomography of capacitively shunted phase qubits with high fidelity. *Phys. Rev. Lett.*, **97**:050502, (2006).

[52] A. Wallraff, D.I. Schuster, A. Blais, L. Frunzio, J. Majer, S.M. Girvin, and R.J. Schoelkopf. Approaching Unit Visibility for Control of a Superconducting Qubit with Dispersive Readout. *Phys. Rev. Lett.*, **95**:060501, (2005).

[53] I. Marcikic, H. de Riedmatten, W. Tittel, V. Scarani, H. Zbinden, and N. Gisin. Femtosecond time-bin entangled qubits for quantum communication. *arXiv:quant-ph/0205144v2*.

[54] A. J. Berkley, H. Xu, R. C. Ramos, M. A. Gubrud, F. W. Strauch, P. R. Johnson, J. R. Anderson, A. J. Dragt, C. J. Lobb, and F. C. Wellstood. Entangled macroscopic quantum states in two superconducting qubits. *Science*, **300**:1548, (2003).

[55] Yu.A. Pashkin, T. Yamamoto, O. Astafiev, Y. Nakamura, D.V. Averin, and J.S. Tsai. Quantum oscillations in two coupled charge qubits. *Nature*, **421**:823, (2003).

[56] J.B. Majer, F.G. Paauw, A.C.J. ter Haar, C.J.P.M. Harmans, and J.E. Mooij. Spectroscopy on two coupled superconducting flux qubits. *Phys. Rev. Lett.*, **94**:090501, (2005).

[57] I. Chiorescu, P. Bertet, K. Semba, Y. Nakamura, C.J.P.M. Harmans, and J.E. Mooij. Coherent dynamics of a flux-qubit coupled to a harmonic oscillator. *Nature*, **431**:159, (2004).

[58] P. Bertet, I. Chiorescu, G. Burkard, K. Semba, C. J. P. M. Harmans, D. P. DiVincenzo, , and J. E. Mooij. Dephasing of a superconducting qubit induced by photon noise. *Phys. Rev. Lett.*, **95**:257002, (2005).

[59] F. Yoshihara, K. Harrabi, A. O. Niskanen, Y. Nakamura, and J. S. Tsa. Decoherence of flux qubits due to 1/f flux noise. *Phys. Rev. Lett.*, **97**:167001, (2006).

[60] T. Lindström, C. H. Webster, J. E. Healey, M. S. Colclough, C. M. Muirhead, and A. Ya. Tzalenchuk. Circuit qed with a flux qubit strongly coupled to a coplanar transmission line resonator. *cond-mat.supr-con/0704.0727v3*, (2007).

[61] A. Blais, R.-S. Huang, A. Wallraff, S.M. Girvin, and R. J. Schoelkopf. Cavity quantum electrodynamics for superconducting electrical circuits: an architecture for quantum computation. *Phys. Rev. A*, **69**:062320, (2004).

[62] R. Doll and M. Näbauer. Experimental proof of magnetic flux quantization in a superconducting ring. *Phys. Rev. Lett.*, **7**:51, (1961).

[63] B.S. Deaver and W.M. Fairbank. Experimental evidence for quantized flux in superconducting cylinders. *Phys. Rev. Lett.*, **7**:43, (1961).

Danksagung

An dieser Stelle möchte ich mich bei denjenigen bedanken, die zu dieser Arbeit beigetragen haben.

Dr. Rudolf Gross danke ich, dass er mir (als LMU Student) die Arbeit am Walther-Meissner-Institut überhaupt erst ermöglicht hat. Ebenso dafür, dass er immer wieder Zeit fand, mit mir meine Ergebnisse zu besprechen und mir hilfreiche Hinweise zu möglichen Problemursachen zu geben.

Bei *Dr. Achim Marx* möchte ich mich für die Hilfestellungen und Diskusionen bedanken. Auch wenn es zu kritischen Situationen kam, behielt er einen kühlen Kopf (obwohl es im Labor schon kalt genug war). Auch möchte ich mich für das Korrekturlesen dieser Arbeit bei ihm bedanken.

Ein ganz besonderer Dank geht an *Tomasz Niemczyk* für einfach alles: die Einführung an den Geräten und im Labor, die vielen Diskusionen über Paper oder über das Verhalten der Hybrid Ringe und natürlich das Korrekturlesen dieser Diplomarbeit. Ohne Tomasz wäre diese Arbeit so nicht möglich gewesen.

Frank Deppe möchte ich für die Hilfestellungen bei der Einleitung und meinem Poster danken. *Edwin Menzel*, *Matteo Mariantoni* und *Georg Wild* danke ich dafür, dass sie mir immer weitergeholfen haben, wenn ich Probleme mit z. B. diversen Gräten hatte oder einfach nur jemanden zum Diskutieren brauchte.

Ein Dankeschön geht auch an *Karl Madek*, der nicht davor zurückscheute, sich meine Probevorträge anzuhören und zu kommentieren.

Tobias Heimbeck möchte ich für die anfängliche Administration danken. Ohne ihn hätte bei mir die Umstellung von Windows 2000 auf XP nicht so reibungslos funktioniert.

An dieser Stelle möchte ich auch die Mithilfe der WMI Werkstadt, speziell *Robert Müller, Helmut Thies* und *Christian Reichlmeier* ebenso wie die Hilfe von *Thomas Brenninger* herausheben, die unter anderem meine Messbox herstellten und mir häufig mit Rat und Tat bzgl. technischen Fragen zur Seite standen.

Desweiteren geht mein Dank natürlich auch an all diejenigen, die ich hier jetzt nicht persönlich ansprach, die aber indirekt zu dieser Arbeit beigetragen haben. Das gilt jetzt vor allem für sämtliche Diplomaden, Doktoranden und sonstige Mitarbeiter am WMI.

At this point, I would like to thank *Dr. Alexey Ustinov* for the opportunity to use the LTLSM in Erlangen. This thank is also to *Tobias Wirth* who showed me the setup and helped to perform three LTLSM-measurements within three days. It was him who enabled this measurements. For the technical advise I would like to thank *Dr. Alexandr Lukashenko*.

Ich möchte mich auch bei Herrn *Stefan Beyer* für die Möglichkeit das 8 GHz Oszilloskop und den Mikrowellengenerator bei Infineon benutzen zu dürfen, bedanken.
A special thank goes to *Robyn Benjamin* who gave me advices in questions about the English language and helped me to translate from "german English" to "english English".
Abseits der eigentlichen Arbeit möchte ich mich bei all meinen Freunden bedanken, die mich viel unterstützt haben und auch viel Geduld aufbrachten, wenn ich mal wieder "laut gedacht" habe. Vielen Dank an dieser Stelle vor allem an *Flo* und *Katrin* für ein teilweise sehr kritisches Lesen meiner Arbeit. *Juli* möchte ich danken für ihre stets offenen Ohren und ihre Engelsgeduld.
Aber der wohl größte Dank geht an meine Geschwister, *Angelika*, *Thomas*, *Martin* und an meine Eltern. Vielen Dank für Eure Unterstützung in allen Lebenssituationen. Ich hoffe Ihr wisst was für eine große Unterstützung Ihr ward und seid.

Erklärung

Mit der Abgabe der Diplomarbeit versichere ich, dass ich die Arbeit selbständig verfasst und keine anderen, als die angegebenen Quellen und Hilfsmittel benutzt habe.

München, den 15.Februar 2008 .....

Elisabeth Hoffmann